TWO-DIMENSIONAL METAL PHOSPHATE NANOMATERIALS FOR ENERGY STORAGE APPLICATIONS

by

GREGORY ROBERT NEHER

(Under the Direction of Tina T. Salguero)

ABSTRACT

The ability to synthesize two-dimensional inorganic nanomaterials is one of the many important challenges in materials science. Olivine $LiMPO_4$ (M = Mn, Fe, Co, Ni) compounds represent an emerging class of cathode materials for lithium-ion batteries, whose electrochemical properties can be significantly enhanced by nano-structuring in two dimensions. My research focuses on developing and understanding synthetic routes that ultimately produce freestanding nanosheets of $LiMnPO_4$. To achieve these goals, my synthetic strategy utilizes $Mn_3(PO_4)_2 \cdot 3H_2O$ nanosheets as reactive synthons. In chapter 2, I discuss how this approach led to the synthesis of a new $Mn_3(PO_4)_2$ polymorph—a microporous open-framework compound with intriguing potential in emerging electrode applications. In chapter 3, I describe the solvothermal reaction parameters that lead to <10 nm thick nanosheets of $LiMnPO_4$, and how the morphology can be tuned by varying certain factors. Finally, in chapter 4, I discuss the unique nanoscrolling behavior of $Mn_3(PO_4)_2 \cdot 3H_2O$ nanosheets under specific reaction conditions.

INDEX WORDS: nanosheets, two-dimensional materials, Li-ion battery cathodes, Lithium metal phosphates, δ-Manganese Phosphate, Manganese Phosphate Hydrates

TWO-DIMENSIONAL METAL PHOSPHATE NANOMATERIALS FOR ENERGY STORAGE APPLICATIONS

By

GREGORY ROBERT NEHER

B.S., Miami University, 2012

A Dissertation Submitted to the Graduate Faculty of The University of Georgia in Partial Fulfillment of the Requirements for the Degree

DOCTOR OF PHILOSOPHY

ATHENS, GEORGIA

2018

TWO-DIMENSIONAL METAL PHOSPHATE NANOMATERIALS FOR ENERGY STORAGE APPLICATIONS

By

GREGORY ROBERT NEHER

Major Professor:	Tina T. Salguero
Committee:	Ramaraja Ramasamy
	John Stickney

Electronic Version Approved:

Suzanne Barbour
Dean of the Graduate School
The University of Georgia
May 2018

DEDICATION

To my beautiful fiancé, friends, and family

ACKNOWLEDGEMENTS

I would like to acknowledge all of my former and current labmates who helped me throughout graduate school. Chris Barrett, Darrah McDaniel-Johnson, Timothy Pope, Matt Davidson and Roshini Ramachandran are former coworkers who all provided invaluable advice on anything ranging from microscopy and analytical techniques to suggestions and advice for my various projects and presentations. I would also like to thank my excellent labmates and coworkers: Monika Milkovska, Mayra Pedraza, Matt Bloodgood, Nick Nguyen, Harshani Rathnaweera, Eman Abdelrahman, Yassamin Ghafouri, Matt Seivert—you all made it a joy to come to work everyday. I would also like to especially thank Dr. Eric Formo for microscopy and graduate school advice.

Furthermore, I would also like to thank my research advisor, Dr. Tina Salguero. Under her mentorship, I learned the importance of conducting thorough research, how to critically analyze scientific and approach scientific problems, and how to give excellent research presentations. She has been a great advisor and I have truly enjoyed performing research in her group.

Furthermore, I would also like to thank my committee members, Dr. Ramaraja Ramasamy and Dr. John Stickney for providing excellent advice throughout my Orals and Prospectus presentations.

Finally I would like to thank my fiancé Amy, my parents, Rob and Deb, my brothers, Tim and Travis, my sister, Elise, and everyone else who helped and supported me throughout graduate school.

TABLE OF CONTENTS

Page

CHAPTER 1

INTRODUCTION AND LITERATURE REVIEW

Lithium-ion Battery Chemistry

Portable energy storage has gained increasing prominence as technology delves into electric vehicle applications and as our laptops and phones demand increasing energy. One popular energy storage technology is the lithium-ion battery. Lithium-ion batteries feature high energy-density, high power density, long cycle life, and relatively environment friendliness, making them ideal for portable applications as well as electric and hybrid vehicle applications.[1],[2]

The first lithium-ion battery was successfully commercialized in 1992, but research into this remarkable energy technology started in the early 1970s. Lithium-ion batteries, also known as “rocking chair batteries” have the same makeup as a standard electrochemical cells.

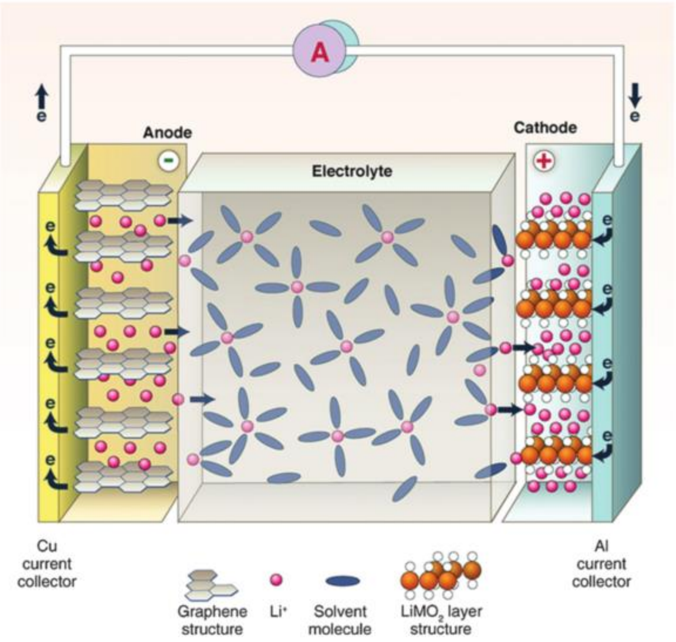

Figure 1.1. Schematic of a Li-ion battery from ref 3[3]

A lithium-ion electrochemical cell contains a cathode, an anode, and electrolyte, as shown in Figure 1.1. During discharge, lithium ions are extracted from the anode and inserted into the cathode, generating a current. During the charge process, an external current provides the driving force for the extraction of lithium from the cathode, which is then inserted into the anode. The reversibility of this type of electrochemical cell arises from the structural stability of both the anode and cathode. For example, in many commercial Li-ion batteries, the cathode is $LiCoO_2$ and the anode is graphitic carbon. Upon charging, Li ions are extracted from the $LiCoO_2$ cathode according to the following equation:

$$LiCoO_2 \leftrightarrows Li_{1-x}CoO_2 + xLi^+ + xe^- \tag{1.1}$$

Li is then inserted into the graphite anode, as shown by:

$$Li^+ + xe^- + 6C \leftrightarrows Li_xC_6 \tag{1.2}$$

The double arrows represent the reversibility of this reaction, which occurs upon discharging.[4] Like any electrochemical cell, lithium-ion batteries are restrained by the laws of thermodynamics. Knowledge of these rules are important to design batteries with high discharge capacity, energy densities, and power density. The change in the free energy, ΔG^0 of an electrochemical cell at standard conditions is calculated from the equation:

$$\Delta G^0 = -nFE^0 \tag{1.3}$$

Where n is the number of electrons transferred, F is Faraday's constant (96,485 C/mol), and E^0 is the cell potential at standard conditions. However, under non-standard conditions, the cell potential is described by the Nernst equation:

$$V_{OC} = E^0 - \frac{RT}{nF} ln \frac{\mu_B^i \mu_D^i}{\mu_A^i \mu_C^i} \tag{1.4}$$

Where V_{OC} is the open circuit potential, or the potential between terminals without a current load, R is the gas constant, T is temperature, and μ is the activity of the chemical species taking part in the reaction. For lithium-ion batteries, V_{OC} can be described by:

$$V_{OC} = -\frac{1}{nF}(\mu_A^i - \mu_C^i) \tag{1.5}$$

Where μ_A and μ_C are the chemical potentials of the anode and cathodes, respectively. One common parameter measured in batteries is energy density, which is representative of how much energy per mass can be stored. The theoretical energy density (Wh/kg) of a cell is calculated by multiplying V_{OC} by the theoretical discharge capacity of a material:

$$E = V_{OC}Q_{dis} \tag{1.6}$$

Another important battery parameter is specific capacity, or the charge a material can store per mass of material (Ah/Kg). The theoretical value is obtained from the following equation:

$$Q = \frac{1000 \times nF}{3600 \times M_W} \tag{1.7}$$

Where M_W is the molecular weight of the material. Therefore, to realize high specific capacities of lithium ion batteries it is imperative to use compounds with low molecular weights that transfer a high degree of electrons.

The power density (W/kg) derived from a lithium ion battery cell is defined as the product of the discharge current and the voltage on discharging:

$$P_{out} = I_{dis}V_{dis} \tag{1.8}$$

The energy density, power density, and discharge capacity electrochemical properties are determined by the electrolyte, cathode, and anode used.[4]

A suitable electrolyte for Li-ion batteries needs to contain the following properties: high ionic conductivity, wide voltage stability window, high thermal and chemical stability, and low reactivity towards the separator and current collector.[5] For an electrolyte to be thermodynamically stable, the energy gap E_g between the highest occupied molecular orbital (HOMO) and lowest unoccupied molecular orbital (LUMO) must be greater than or equal to the chemical potential of the anode μ_A and cathode μ_C:

$$\mu_A - \mu_C \leq E_g \tag{1.9}$$

Typical electrolytes for Li-ion batteries contain a Li salt dissolved in an appropriate organic solvent. Alkyl carbonates are popular organic solvents for Li-ion batteries because they are polar aprotic and therefore stable at negative potentials, but still able to dissolve Li salts. These solvents also have high boiling points, along with high dielectric constants. Combinations of cyclic alkyl carbonates, such as propylene carbonate and ethylene carbonate, are usually combined with long chained carbonates, such as ethyl and diethyl carbonate, to decrease the viscosity.[6] Commonly used organic solvents are shown in figure 1.2.

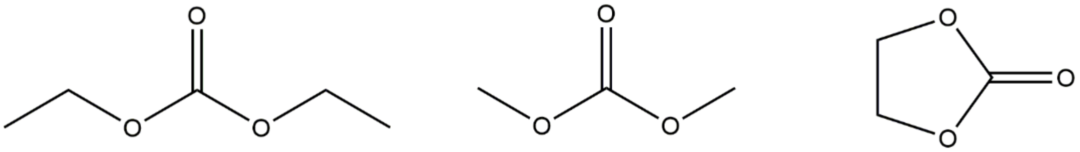

Diethyl carbonate Dimethyl carbonate Ethylene carbonate

Figure 1.2. Common solvents for the electrolyte in lithium-ion batteries

The lithium salts most commonly used in commercial Li-ion batteries are $LiClO_4$ and $LiPF_6$. $LiClO_4$ has a higher ionic conductivity, but is unstable at low potentials, which is why $LiPF_6$ is typically the electrolyte of choice.[6]

The separator, as its name implies, separates the cathode and anode from making direct contact. Common separators include polypropyrene, polyethylene, and poly(vinyl)formamide. The separator can also impede lithium ion diffusion by closing micropores if the cell becomes to hot—an important safeguard against thermal runaway.[4]

The negative terminal of a Li-ion battery, or anode, has the following ideal properties: the ability to accommodate a large amount of Li (small molar mass), a small redox potential relative to Li^0/Li^+ (to maximize cell potential), high electronic and ionic conductivities, low reactivity with the electrolyte, and high safety. Lithium metal anodes have the ability to provide cells with high energy densities. However, lithium is highly reactive with the organic electrolyte and forms a passivating layer, called the Solid Electrolyte Interphase (SEI). During charging, lithium is deposited on this substrate in the form of dendrites, which significantly reduces the amount of lithium available in the cell, and can potentially lead to short circuiting of the cell. Furthermore, lithium suffers from small lifetimes and poor thermal stability—two qualities that make it poor choice for commercial batteries. However, Li is used as an anode (and reference electrode) for testing coin cells in laboratory settings.[4]

Because of the above reasons, graphite is used at the anode in commercial Li-ion batteries. Graphite is cheap, abundant, and has a low potential vs Li of 0.15-0.25 V. It also exhibits suitable electronic conductivity (10^{-3} S/Cm) and lithium ion diffusion. However, the specific capacity is rather low (372 mAh/g) as it can only accommodate 1 Li atom per 6 Carbon atoms.[4]

Current anode research focuses on raising the specific capacity of the anode by using different carbonaceous materials, or by replacing graphite with another material, such as silicon or $Li_4Ti_5O_{12}$. Silicon is an attractive anode material because of its high theoretical capacity of 4200 mAh/g, but it suffers from poor cycling performance due to the large volume expansion upon Li intercalation and growth of a large SEI layer[7]. Another promising anode material is $Li_4Ti_5O_{12}$. The redox couple for this material is 1.55 V versus Li, which is high enough to prevent the formation of the SEI layer. Moreover, it is remarkably stable over hundreds of charge/discharge cycles.[8] Unfortunately, the electronic structure of $Li_4Ti_5O_{12}$ is that of an insulator and must be synthesized or coated with a conductive additive to improve its electrochemical performance.[9] Also, improving the charge capacity of the anode is an important endeavor, however, a Li-ion cell is still limited by the capacity of the cathode.[4] Therefore, a large amount of research is devoted towards improving the cathode.

An ideal cathode has the following properties: high potential vs. Li^0/Li^+, high theoretical capacity, or the ability to store lithium ions, structural stability upon charge and discharge, unreactive with the electrolyte, and containing a band gap E_g of the redox couple in between the HOMO and LUMO of the electrolyte.

One of the first commercial cathodes employed was $LiCoO_2$ (with graphite as the anode). $LiCoO_2$ adopts the α-$NaFeO_2$ structure, shown in figure 1.3. In this structure, $[CoO_6]$ octahedra are edge-shared to form crystallographic layers. The Li ions reside in between adjacent layers. Cobalt exists as Co^{3+} in a low spin ground state. However, as more Li is extracted, only ~50 % of its theoretical capacity can be obtained due to the chemical instability of Li_xCoO_2 and disorder of the crystal lattice when discharged to below $x = 0.5$.[10]

$LiMn_2O_4$ has also seen use as a cathode material. The spinel structure of $LiMn_2O_4$, shown in figure 1.3, is composed of a three-dimensional network of edge and corner-shared $[MnO_6]$ octahedra and $[LiO_4]$ tetrahedra. $LiMn_2O_4$ cathodes are cheaper and less toxic than $LiCoO_2$, and have a high energy density. However, this material suffers from manganese dissolution in the electrolyte and severe capacity fade at high temperatures[11].

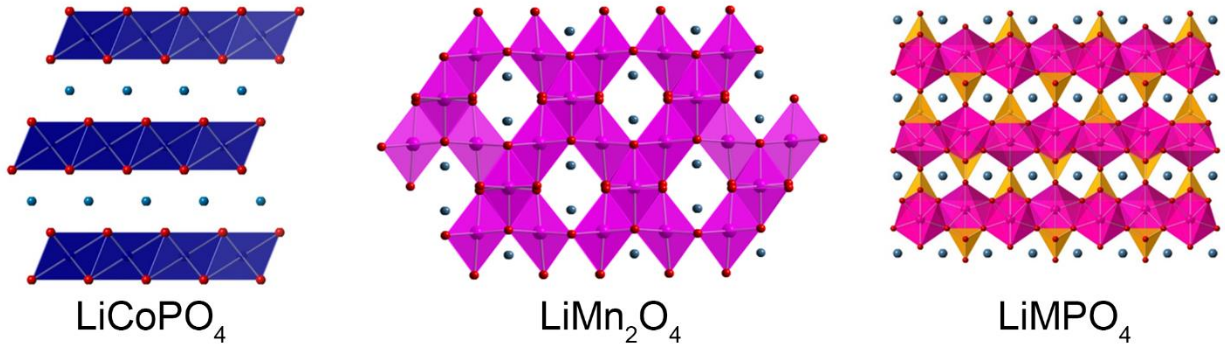

Figure 1.3. Crystal structures of commonly used cathode materials for Li-ion batteries. M = Mn, Fe, Co, Ni.

Another disadvantage of both $LiCoO_2$ and $LiMn_2O_4$ is their safety issues. At elevated temperatures, they can undergo thermal runaway—a self-staining increase in temperature of the battery cell.[3] This phenomenon occurs as a result of external or internal temperature rise of the battery cell. At temperatures above 180 °C, these cathode materials generate O_2 from the crystal lattice. The evolved O_2 oxidizes the electrolyte, and causes temperatures to rise as fast as 100 °C/min.[12] Therefore, much research is focused on developing cathode material with higher thermal and chemical stabilities.

$LiMnPO_4$ (M = Mn, Fe, Co, Ni)

Recently, olivine $LiMPO_4$ (M = Mn, Fe, Co, Ni) have taken center stage as next-generation cathodes due to their relatively high potentials, energy density and safety. They were first successfully demonstrated as viable cathodes in lithium ion batteries by Goodenough and coworkers in 1997.[13] Here they validated the reversible lithium extraction and intercalation of $LiFePO_4$ at a flat voltage of 3.5 V vs. Li^0/Li^+, and concluded that lithium insertion/extraction occurred by way of a two-phase interaction. Since then, there have been thousands of papers on these compounds and there electrochemical properties as Li-ion battery cathodes.

These compounds belong to the metal (II) phosphates, a class of compounds that hold potential in various energy applications, such as supercapacitors, heterogeneous catalysts and electrode materials. This broad class of compounds encompasses a large variety of structures and morphologies, both artificial and natural. The structural diversity of these compounds stems from the propensity of the [PO_4] tetrahedra to edge and corner-share with metal (II) polyhedra groups, as well as other tetrahedra including SiO_4 and AlO_4.[14]

Shown in figure 1.4 is the crystal structure of $LiMPO_4$ (M = Mn, Fe, Co, Ni). This compound is composed of planes of distorted [MO_6] octahedral extending in the [010] and [001] directions. [PO_4] tetrahedra connect these planes by edge-sharing and corner-sharing to form an open-framework structure. Li resides in the [010] and [001] channels of this structure.

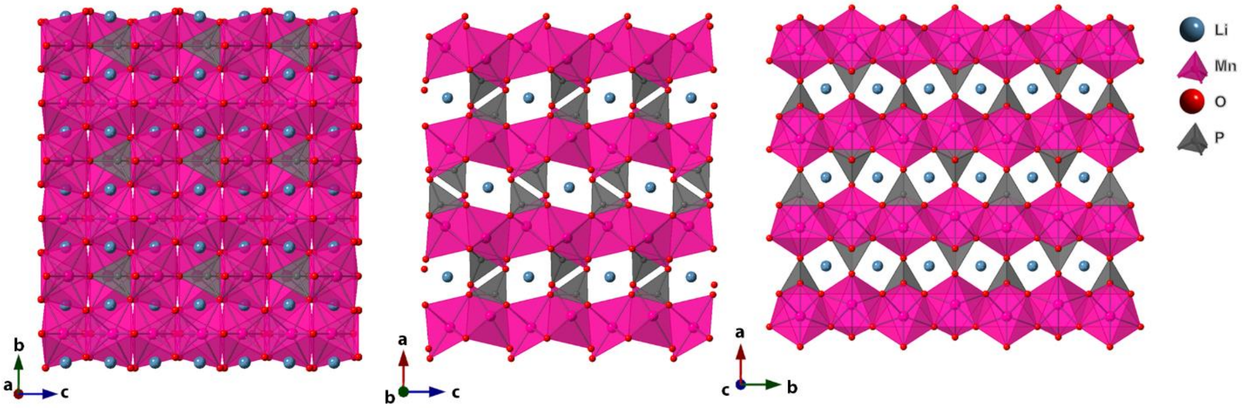

Figure 1.4. Crystallographic orientations of the (200), (020), and (002) planes of $LiMPO_4$ (M = Mn, Fe, Co, Ni)

The relatively high potential range of these compounds (3.4-5.1 V vs Li^0/Li^+) arises from the inductive effect of the [PO_4] group. Typically, the stronger the M-O bond, the higher the energy of the M^{3+}/M^{2+} redox couple and the smaller the V_{oc}. The P cation of the [PO_4] tetrahedra shares a common P-O-M linkage. A stronger P-O bond results in a weaker M-O bond, ultimately stabilizing and lowering the Fermi level of $LiMPO_4$, causing the relatively high theoretical potentials observed for these compounds.[15]

To date, only $LiFePO_4$ has been successfully commercialized; While $LiCoPO_4$ and $LiNiPO_4$ have higher theoretical energy densities, their potential versus Li/Li^+ is incompatible with the organic electrolyte. $LiMnPO_4$ is attractive because its voltage (4.1V vs Li^0/Li^+) exists within the electrochemical stability window of the electrolyte, leading to a theoretical energy density of 701.1 Wh/kg.[16] However, $LiMnPO_4$ suffers from several drawbacks that need to be overcome if it is to be used commercially.

A significant problem to realize the full electrochemical performance of $LiMnPO_4$ cathodes is its poor electronic conductivity. For example, the conductivity of $LiFePO_4$ is 10^{-9}-10^{-10} cm^{-1} while the conductivity of $LiMnPO_4$ is over an order of magnitude less $<10^{-10}$ S cm^{-1} [17]. Density of states (DOS) calculations show that $LiMnPO_4$ is an insulator, with a 2-4 eV band gap. $LiFePO_4$ is a semiconductor with 0.3 eV band gap.[18],[19] However, the conductivity can be improved by several different carbon coating methods.

The carbon-coating must be tuned for each material and morphology. For annealing methods, $LiMnPO_4$ is heated up to temperatures between 600-700 °C in an inert atmosphere, along with a compound that contains a high carbon contents, such as glucose. The goal is to form a thin <5 nm thick layer of amorphous carbon on the surface of $LiMnPO_4$, to improve the electronic conductivity, without hindering Li^+ diffusion.[20],[21] The carbon coating also has the added benefit of mitigating dissolution of the material by the electrolyte. The $LiPF_6$ is sensitive to trace amounts of water, forming HF, which can go on to erode the transition metals.[21] The choice of carbon-containing precursor vital—Yang et al tested five different organic molecules as carbon sources to coat $LiMnPO_4$ nanorods, and found that each affected the electrochemical performance differently.

Beta-cyclodextrin and sucrose as carbon sources achieved the highest electrochemical capacity, while citric acid and ascorbic acid, the least. The author posited that the higher number of oxygenous groups lead to stronger absorption on the $LiMnPO_4$ surface, ultimately providing better conductivity.[22]

Furthermore, time of annealing, temperature, and percentage of carbon source used are all important parameters. Chen and coworkers studied all three of these factors on $LiMnPO_4$ microparticles. They found that using 20 wt% glucose was optimal—at higher loadings the carbon coating was detrimental to Li^+ diffusion, and at lower loading the $LiMnPO_4$ nanoparticles were not conductive enough.[23] This conclusion was also corroborated by a previous work performed on $LiFePO_4$. High loadings of Carbon resulted in increased polarization and a decrease in the reversibility of the reaction.[20]

Unfortunately, there is not a one-size fits all method for carbon-coating. Each method must be adjusted according to the morphology. Still, while these carbon-coating strategies lead to better electrochemical performance for $LiMnPO_4$, the amount of carbon required is still higher than that of $LiFePO_4$. Carbon-coating techniques that raise the conductivity without compromising volumetric density are required in order to take advantage of the high theoretical energy density of $LiMnPO_4$.

Other problems that $LiMnPO_4$ faces is volume expansion and instability caused by Jahn-Teller effects upon delithiation. The Jahn-Teller effect states that in a system with a degenerate electronic states, the system will distort to a lower symmetry state to remove this degeneracy.[24] Mn^{2+} has a high spin d^5 configuration, and contains five 3d orbitals. Crystal field splitting separates these orbitals into a triplet (t_{2g}) and a doublet (e_g). However, when Mn^{2+} is oxidized to Mn^{3+}, it is now d^4 and an electron in the (e_g) orbital is removed. The remaining electron is part of a degenerate electronic state, and in order to compensate for this, the Mn-O lengths of the MnO_6 octahedra are significantly distorted into two long Mn-O bonds along the z directions and four short Mn-O bonds along the x and y planes.[25] Experimentally, A mixed binary $LiMn_yFe_{1-y}PO_4$ compound showed significant lattice distortions when delithiated. The 'elastic deformation' of the Mn^{3+} phase was responsible for this distortion.[18]

Perhaps the largest problem to overcome with $LiMnPO_4$, and the other olivine compounds in general, is that lithium is only extracted/inserted in only one dimension. Computational calculations shows that Li ions are inserted and extracted from the lattice along the [010] directions.[19], [26] This pathway is show schematically in figure 1.5. This is especially problematic, as defect sites in the lattice can easily block and impede lithium ion migration and have a severe impact on the electrochemical performance of the material. Islam and coworkers used atomistic modeling techniques and found that anti-site defects, in which a Fe ion is found on a lithium site, were the most favorable defects (having the lowest energy of formation) to form.[26] Antisite defects were experimentally observed in a number of reports. Wang and coworkers reported a correlation

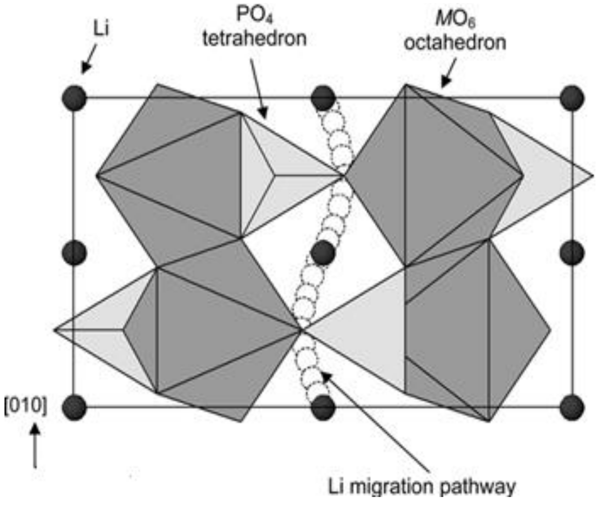

Figure 1.5: Li-ion migration pathway in phospho-olivines, adopted from ref [26][26]

between antisite defect concentration and FTIR Spectra. The defect-free P-O vibration of the PO_4 polyhedron was calculated to occur around 957 cm^{-1}, while high wave-numbers represented a greater degree of defects.[27] Ikuhara and coworkers were able to observe anti-site defects in the lattice using High-angle annular dark field (HAADF). HAADF was used instead of bright-field HRTEM because it provides high Z contrast. In this technique, they were able to detect high contrast in the lithium channels in the (010) lattice plane, indicative of Fe blocking the lithium channels. Furthermore, they found a tendency for the anti-defect sites to aggregate in localized clusters.[28]

Zaghib and coworkers observed less anti-site defects at longer hydrothermal reaction times. The intercalation of Li^+ and exchange with Fe^{2+} in the $Fe_3(PO_4)_2{\cdot}8H_2O$ intermediate was determined to be the main driving source of defect removal.[29] In another report, anti-site defects were significantly reduced by adding $CaSO_4$ to the hydrothermal reaction mixture. The calcium ions were able to form high energy facets of $LiFePO_4$ crystals, confining anti-site defects to a thin surface layer.[30]

There has been mild success in eliminating anti-site defects. Whittingham and coworkers used Rietveld analysis on the X-ray diffraction patterns of hydrothermally synthesized $LiFePO_4$. They found that the % of Fe on Li sites was as high as 7.8 % for a hydrothermal reaction at 120 °C, but sharply decreased with increasing reaction temperature. No defects were observed about 200 °C.[31]

One strategy to improve the Li-ion migration and eliminate the influence of defect sites is to design nanomaterials with the smallest possible Li-ion diffusion pathway. Nanosheets, or nanomorphologies that contain lateral dimensions in microns and thicknesses <10 nm, represent an excellent nanomorphology to decrease the Li diffusion to the smallest size possible, while still maintaining a large active surface area. The next section will discusses different methods for synthesizing two-dimensional materials.

Two-dimensional Materials

Two-dimensional nanomaterials have recently taken center stage in materials science research. With lateral dimensions in microns and thicknesses of <10 nm, these free-standing nanosheets hold promise for future materials with exotic electronic, mechanical, and chemical properties. Graphene, a one-atomic-layer thick of carbon, is one of the most well-studied and recognizable two-dimensional materials. Owing to its ultrathin morphology, graphene exhibits an exceptionally high electron mobility (> 2,000 $cm^2/V\cdot s$)[32] , a high Young's modulus value of 1.0 TPA,[33] and high (>90%) optical transparency.[34] And yet, graphene is remarkably easy to make; Geim and coworkers demonstrated the 'scotch-tape method', a technique in which high-quality graphene monolayers are peeled from graphite with tape.[35]

However, two-dimensional materials aren't confined to just carbon. Other well-studied graphene-like compounds include transition metal dichalcogenides (TMD's), boro-nitride and Layered Double-Hydroxides (LDHs). The crystal structures of these compounds are intrinsically layered and contain lamella with strong in-plane covalent or ionic bonding, held together by weaker out-of-plane van der Waals or electrostatic interactions between the layers. For example, MoS_2, a TMD, contains layers of covalently bound Mo and S, held together by van der Waals forces.[36] The layered crystal structure of graphene, TMDs, and LDHs are highlighted in Figure 1.6. Because of the weak interaction between layers, these compounds are readily delaminated into single layers through 'top-down' methods. In these procedures, a starting bulk compound with a layered structure is exfoliated through mechanical or chemical means. Graphene as well as TMDs and other layered compounds can be exfoliated by probe sonication.[37],[38] The shear rates created by probe sonication are enough to overcome the van der Waals interactions and break the layered structure into nanosheet components. Furthermore, this method can be assisted by using a compatible solvent, such as N-methyl pyrrolidone or isopropyl alcohol that has a similar surface energy to the desired sheets.[37],[38]

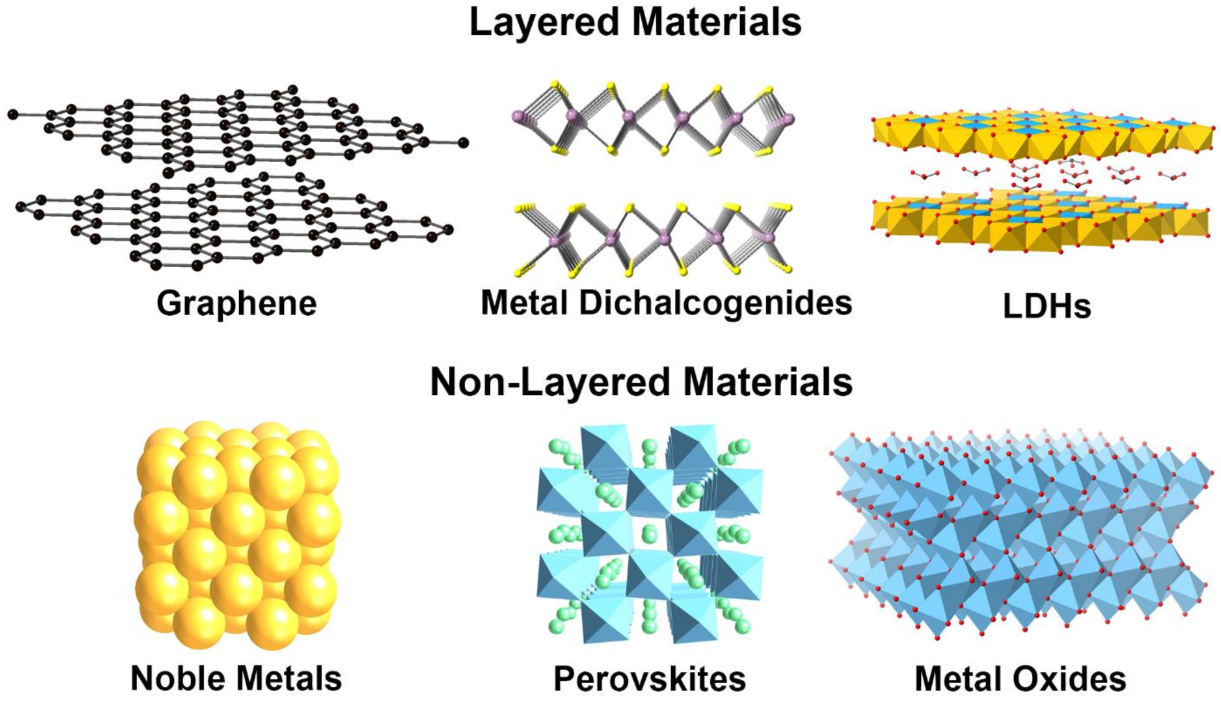

Figure 1.6. Crystal structures of several layered materials (top row) and non-layered materials (bottom row)

Although mechanical exfoliation provides a relatively cheap and easy way to access two-dimensional morphologies of layered bulk compounds, it often yields nanosheets of inconsistent size and thickness. Chemical exfoliation strategies in general produce much more reliable dimensions and morphologies. Takayoshi Sasaki was one of the first pioneers of chemical exfoliation methods that utilized bulky organic compounds to delaminate bulk precursors.[39] With this strategy, Sasaki was able to produce “Oversized” titania nanosheets from $K_{0.8}Ti_{1.73}Li_{0.27}O_4$ crystals. In this method, the $K_{0.8}Ti_{1.73}Li_{0.27}O_4$ crystals were converted into $H_{1.07}Ti_{1.73}O_4\cdot H_2O$ by acid exchange with 2 M HCl for 5 days, and replacing the acid each day. Afterwards, the protonated titanate was added to a solution of tetrabutylammonium, or TBAOH. The solution was shaken, and the H^+ exchanged with the TBA^+ ions, resulting in the "osmotic swelling" of the protonated structure, as observed by X-ray diffraction. The resulting TiO_2 nanosheets were tens of microns in lateral dimensions and only 1 nm in thickness.[40] A schematic of this same method applied to $Cs_{0.70}Ti_{1.83}O_4$ is shown in figure 1.7.

Sasaki was also successful in extending this method to form nanosheets of MnO_2[41], TaO_3[42], $Cs_4W_{11}O_{36}^{2-}$ [43], and numerous other metal oxide compounds. Still other compounds that were also exfoliated into nanosheets and scrolls by this method are tantalates and titanolates of $H_2[A_{n-1}B_nO_{3n+1}]$ A = Na, Ca, Sr, La; B = Ta, Ti), reported by Schaak et al in 2002,[44] and $HTiNbO_5$, HTi_2NbO_7, and $HTiTaO_5$ by Takagaki et al in 2004[45].

A different, although chemically similar strategy involves the intercalation of ions (Li^+, Na^+) into the interlayer spacings of layered compounds, weakening the van der Waals forces between neighboring layers. This ion intercalation-assisted liquid exfoliation has been successful in producing nanosheets of TMDs. Dines was one of the first to use an alkali metal intercalation agent, when he reacted *n*-BuLi with a number of metal dichalcogenides as far back as 1975. He quantitatively showed that the intercalation process reaction occurred according to the formula:

$$\text{n-}C_4H_9Li + TX_2 \rightarrow LiTX_2 + 1/2\text{n-}C_8H_{18} \tag{1.10}$$

where T = Ti, Zr, Hf, V, Nb, Ta, Mo, or W, and X = S, or Se. On average, intercalation of lithium expanded the crystal lattice by 0.5 Å, measured by XRD.[46] Joensen et al took this process a step further in 1986 and reacted n-BuLi treated MoS_2 with H_2O, resulting in delamination of the structure down to single atomic layers.[36] The rapid gas expansion of H_2 formed by reaction of Li with H_2O was enough to break apart the structure into single layers.[46] Interestingly, these monolayer TMDs were not revisited until the early to mid 2000's, when graphene brought about a renewed interest in two-dimensional materials.

Intercalation of lithium by electrochemical means has also been employed, although to a lesser extent. Zheng and coworkers fabricated coin cells by depositing a slurry of MoS_2 onto a copper electrode, with lithium metal as the anode. After applying a current over the course of 6 h, they were successfully able to electrochemically intercalate lithium into the structure. The Li_xMoS_2 compounds was recovered from the electrode, and sonicated in H_2O to form isolated nanosheets of MoS_2.[47]

While top-down methods are reliable in producing high-quality single and multi-layered nanosheets, they are limited by the structure of the material. Mechanical and chemical exfoliation can easily disrupt the weak forces of intrinsically layered compounds, but are ineffective for materials that contain stronger bonding in three dimensions. Therefore, another approach is needed, specifically one in which a compound is grown, either on a substrate, or in solution. These so called 'bottom-up' methods are able to grow two-dimensional compounds from three dimensional crystal structures. Figure 1.6 shows the crystal structure of several non-layered materials classes that have successfully been synthesized as nanosheets.

Hydrothermal and solvothermal reactions are common bottom-up techniques to grow nanomaterials. In a typical synthesis, the reactants are salts that have been dissolved in the desired solvent. A 'capping agent' is added, typically a bulky organic compound or surfactant (e.g. polyvinylpyrrolidone, oleylamine) that will bind to certain crystal faces during nucleation. The reactants are added to a Teflon-lined steel autoclave, which allows for temperatures that are higher than boiling point of the solvent used.[48] The synthesis of TiO_2 nanosheets, apart from chemical exfoliation, can also be accomplished through hydrothermal and solvothermal techniques.

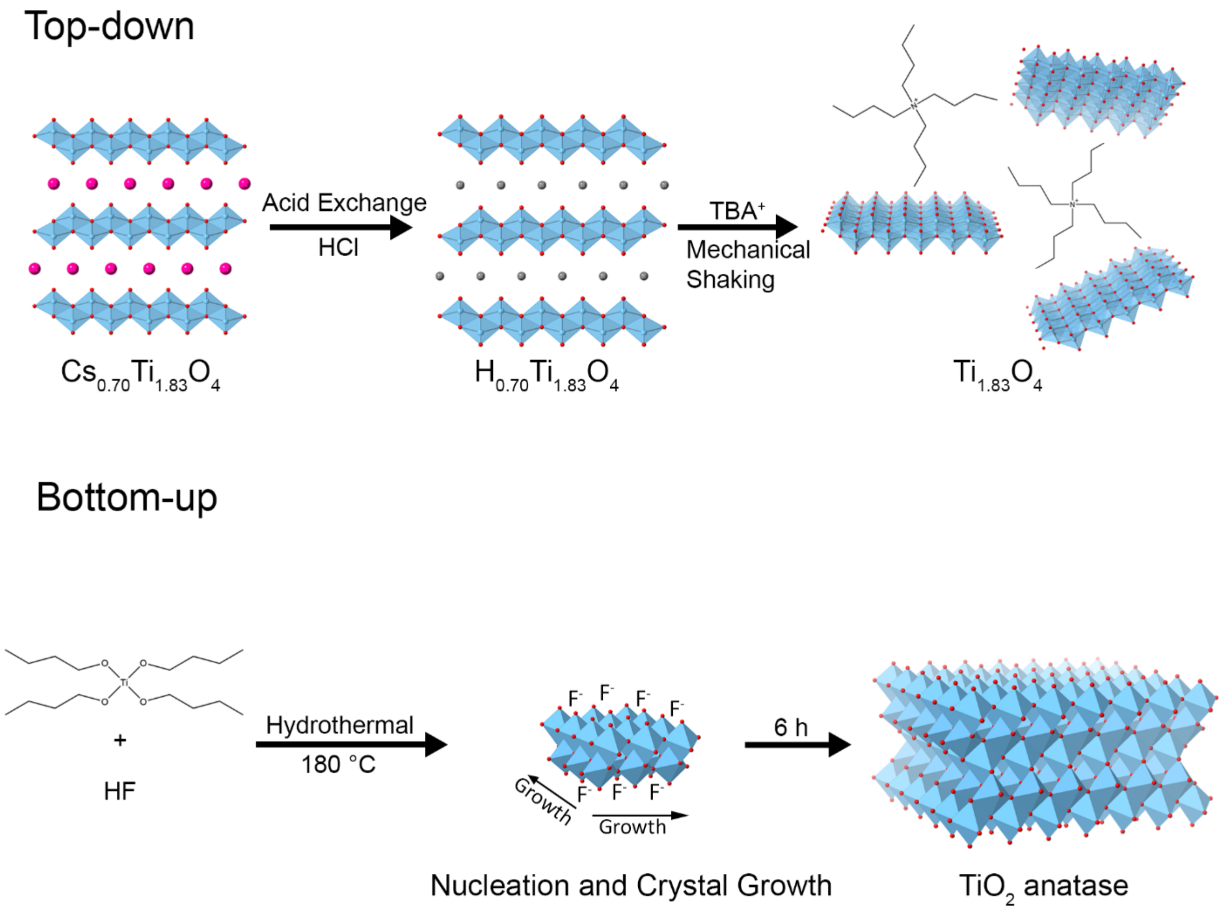

Figure 1.7. Examples of top-down and bottom-up methods that generate two-dimensional materials. Top: ion exchange/mechanical exfoliation of a layered cesium titanate. Bottom: Hydrothermal method using $Ti(OBu)_4$ and HF to grow TiO_2 anatase. Top-down adopted from experimental in Sasaki[49] and bottom-up adopted from Xie[50].

In one example, nanosheets of TiO_2 anatase were grown hydrothermally by using tetrabutyl titanate, $(Ti(OBu)_4$ as the titanium precursor, along with HF as the solvent in a hydrothermal reaction at 180 °C, as illustrated in figure 1.7. The TiO_2 nanosheet products were approximately 40 nm in length, and 6 nm in thickness. The fluoride anions were found to play an important structure-directing role in the two-dimensional growth of TiO_2. During nucleation, of TiO_2, they fluoride anions bonded to the (001) plane of TiO_2, prohibiting growth in the [001] direction.[50] While this method is relatively simple and effective at forming TiO_2 nanosheets with the photocatalytic (001) face, the Sasaki method discussed earlier is far superior in consistently forming single or double-layer TiO_2 nanosheets that are microns in lateral dimensions.

Additionally, Liao and coworkers were able to develop another method of synthesizing nanosheets of TiO_2. Their method used the block polymer Pluronic P123, or PEO_{20}-$PPO_{70}PEO_{20}$ as well as ethylene glycol as a cosolvent in a solvothermal reaction at 150 °C for 20 h. With this method, they were also able to synthesize nanosheets of Co_3O_4, WO_3, and ZnO.[51]

Bottom-up methods work well for compounds that lack an inherent layered structure. For example, metallic nanosheets are notoriously difficult to prepare, due to their desire to form 3-dimensional structures. There have been several reports of successful hydrothermal and solvothermal methods that form metallic nanosheets. Li and coworkers were successful in producing single-layer thick Rh nanosheets using a solvothermal synthesis with poly(vinylpyrrolidone) (PVP) as the structure-directing agent. Computational measurements showed that the PVP molecules decreased the surface energy of Rh nanosheets from 0.126 to 0.071 eV/Å^2. [52] Other metallic nanosheets include Ru nanosheet and nanocrystals[53]

Still, other clever techniques are required to access nanosheets of metallic compounds. One example is the growth of Pd nanosheets by using carbon monoxide (CO) as a structure-directing agent. Zheng and coworkers combined Palladium (II) acetyl acetonate with PVP and a halide salt and added to a reaction vessel in dimethyl formamide (DMF) solvent. Carbon Monoxide gas was added to the vessel until a pressure of 1 bar, and reacted for 100 °C for 3 h. The resulting hexagon-shaped nanosheets were approximately 60 nm in edge length and 1.8 nm thick. The CO gas was determined to strongly absorb on the (111) planes of Palladium and quench the growth in the [111] direction, leading to the ultrathin morphology observed. [54]

Another useful, but less common bottom-up technique is a template-assisted synthesis. In this method, a nanosheet precursor, typically graphene, is used as a two dimensional template to synthesize other two-dimensional morphologies. For example, Huang et al grew Au nanosheets onto a graphene oxide (GO) template. These square nanosheets were 200-500 nm in lateral dimensions, and approximately 2.4 nm thick. To form the nanosheets, $HAuCl_4$ was dissolved in 1-amino-9-octadecene and mixed with a dispersion of GO. Because of the strong affinity of the 1-amino-9-octadecene complex with GO, Au seeds nucleated and began to grow into square shapes upon heating at 55 °C. Without using the GO template, gold nanosheets were still obtained, but also contained a mixture of gold nanowires and nanoparticles.[55]

An example of a non-graphene template involved the formation of nanosheets of the cubic phase of $Cu_{1-x}Se$ from hexagonal CuSe nanosheets. After hot injection of CuSe nanosheets into a Cu solution, the copper-poor non-stoichiometric $Cu_{1-x}Se$ compound was formed. The CuSe acted as a template for insertion of Cu cations during the heat treatment and the crystalline Se framework stabilized the nanosheet morphology during this process resulting in $Cu_{1-x}Se$ nanosheets with only 6 nm in thickness, compared to the 5 nm of the starting CuSe nanosheets.[56]

There are a few reports of $LiMnPO_4$ nanosheet and nanoplate compounds in the literature. For example, Yan and coworkers successfully demonstrated a high pressure, high temperature synthesis to yield nanosheets of $LiMnPO_4$. The nanosheets were less <5 nm thick and exhibited the (020) plane. These nanosheets exhibited higher electrochemical activity compared to bulk—especially at high current rates, due to the large surface area contact with the electrolyte and fast lithium diffusion out of the (020) plane. However, this synthesis requires rather harsh conditons, with high pressure <10 MPa and high temperatures 400 °C.[57]

Other examples include $LiMnPO_4$ nanosheets ~20 nm in thickness synthesized from a solvothermal method, using EG and LiH_2PO_4 and $Mn(CH_3COO)_2 \cdot 4H_2O$ as precursors.[58] Additionally, Liu and coworkers used oleic acid as the capping agents to access $LiMnPO_4$ nanoplates approximately 50 nm in thickness. [17]

Many of these synthetic techniques utilize bottom-up methods, and are modification of the basic recipe of Mn(II) salt, a lithium phosphate precursors, in water or a polyol solvent. Many of these methods generate $Mn_3(PO_4)_2 \cdot 3H_2O$ nanosheets *in situ* during this method.[59],[60]. In Chapters II and III I describe hydrothermal and solvothermal bottom-up approaches using $Mn_3(PO_4)_2 \cdot 3H_2O$ nanosheets as unique synthons to form δ-$Mn_3(PO_4)_2$ and two-dimensional nanosheets of $LiMnPO_4$.

Finally, even though two-dimensional materials were discovered and studied long before the scotch tape method was developed in 2005, it wasn't until the unique properties of graphene were studied in depth that a renewed interest in two-dimensional materials was launched. To date the two-dimensional material field is still in its infancy. Nanosheets reported in the literature represent only a fraction of the tens of thousands of different crystal structures. Developing new methods to form two-dimensional materials is key to unlocking useful and novel properties for energy storage, catalytic and electronic applications.

Research Goals

The goal of my research aims to 1.) improve the lithium diffusion in $LiMnPO_4$ by synthesizing <10 nm thick nanosheets of $LiMnPO_4$ that exhibit the (020) plane 2.) study and explore the synthetic parameters that produce two-dimensional nanosheets of $LiMnPO_4$ 3.) apply this chemical insight to synthesize novel metal phosphate structures.

My research strategy focuses on using manganese phosphate nanosheet precursors as reactive synthons to form nanosheets of $LiMnPO_4$. $Mn_3(PO_4)_2 \cdot 3H_2O$ nanosheets are easily formed by the reaction of an aqueous solution containing Mn(II) cations and $H_2PO_4^-$ or HPO_4^{2-} anions. The $Mn_3(PO_4)_2{\cdot}3H_2O$ nanosheets display lateral dimensions of 1-3 µm and thicknesses <30 nm. The precipitation of $Mn_3(PO_4)_2{\cdot}3H_2O$ as nanosheets is a direct consequence of its layered structure. In this structure, planes of covalently bound Mn polyhedra and PO_4 tetrahedra extend in the [100] and [010] directions. The hydrates reside inbetween these planes. Hydrogen bonding occurs between the H of the H_2O molecules and the O of the PO_4 tetrahedra and Mn polyhedra. The stronger covalently bound (002) plane exhibits more stable bonding than the out-of-plane hydrogen bonding, resulting in the anisotropic growth of this compound in the [100] and [010] directions.[61]

In chapter II, I detail the discovery and synthesis of a new manganese phosphate polymorph that is formed by reacting $Mn_3(PO_4)_2{\cdot}3H_2O$ nanosheets hydrothermally at 250 °C for 6 h. δ-$Mn_3(PO_4)_2$ contains a unique open-framework structure composed of planes of $[MnO_5]$ pentahedra edge and corner-shared to $[PO_4]$ tetrahedra. This novel compound is remarkably different than the structures of the α, β', and γ polymorphs. These polymorphs contain both $[MnO_6]$ octahedra and $[MnO_5]$ pentahedra, edge-and corner-shared with $[PO_4]$, yielding a denser, more compact structure.[62],[63],[64]. δ-$Mn_3(PO_4)_2$ can also be synthesized as microcrystals, by changing the precursor to $Mn_5(PO_4)_2(PO_3OH)_2{\cdot}4H_2O$. Additionally, I describe the solid-state reaction using $LiMnPO_4$ and β-$Mn_3(PO_4)_2$ in a 2:1 molar ratios at 1,000 °C under inert conditions.[65]

Chapter III discusses the reaction of $Mn_3(PO_4)_2{\cdot}3H_2O$ nanosheets with LiH_2PO_4, and the solvothermal conditions that lead to $LiMnPO_4$ nanosheets with thicknesses ~5 nm. These nanosheets exhibited the (200) plane and are approximately 2-5 µm in lateral dimensions. Investigating this reaction and monitoring at different times with XRD and SEM reveals that $LiMnPO_4$ nanosheets form after just 2 h. As the reaction proceeds, the peak belonging to the (200) plane in the XRD pattern becomes noticeably more intense, indicative of greater crystallinity and two-dimensional growth. Further exploring this reaction reveals that $LiMnPO_4$ nanosheets form under a stringent set of conditions—water to diethylene glycol ratio, temperature, and lithium precursor all play significant roles in the structure and morphology of the final product. Three-dimensional morphologies of $LiMnPO_4$ were formed when Li_3PO_4 was used instead of LiH_2PO_4 suggesting that the $H_2PO_4^-$ anion plays a structure-directing role upon $LiMnPO_4$ nanosheets formation. Solvent ratio of DEG:H_2O was determined to also be a key component in this reaction. At lower ratios of DEG:H_2O, $\underline{\delta}$-$Mn_3(PO_4)_2$ formed instead. Furthermore, at lower temperatures, even a small amount of H_2O (<5ml) in the system favored $Mn_5(PO_4)_2(PO_3OH)_2 \cdot 4H_2O$ formation. Additionally, both δ-$Mn_3(PO_4)_2$ and β'-$Mn_3(PO_4)_2$ form $LiMnPO_4$ under the same reaction conditions.

Although the $LiMnPO_4$ nanosheets exhibit the (200) plane, instead of the high-rate (020) plane for fast lithium diffusion, this material does exhibit interesting electrochemical properties. For this particular two-dimensional morphology, the most favorable path for lithium diffusion is through the edges of the nanosheets. Wang and coworkers showed that $LiFePO_4$ nanosheets <15 nm thick oriented with the (200) face exhibited superior electrochemical properties to that of the (020) plane. This fascinating result was hypothesized in terms of increasing the coherency strain of the active material. The coherency strain is the difference in lattice strain between $LiFePO_4$ and its delithiated $FePO_4$ state.[66] Measuring the discharge capacity for each charge-discharge cycle at 1/20 C reveals that the nanosheets exhibit slightly higher discharge capacities over the course of 25 cycles, which is indicative of high cycling stability for this material. Future work aims to optimize the carbon coating and shrink the lateral dimensions of this material by ball-milling and ultrasonication methods to ultimately raise the discharge capacity closer to the theoretical capacity (171 mAh/g) of $LiMnPO_4$.

In Chapter IV, I study the scrolling behavior of $Mn_3(PO_4)_2{\cdot}3H_2O$ nanosheets. Scrolling was found to occur by changing the reactant conditions, and also by reacting $Mn_3(PO_4)_2{\cdot}3H_2O$ nanosheets hydrothermally. Changing the reactant solvent to 25:5 H_2O:EtoH resulted in scrolled $Mn_3(PO_4)_2{\cdot}3H_2O$ nanosheets. Testing other solvents revealed that most polar solvents lead to scrolling. Furthermore, no scrolling was observed when carried out in non-polar organic solvents, such as hexane and pentane. $Mn_3(PO_4)_2{\cdot}3H_2O$ nanoscrolls were also formed by changing the pH of the precursor $(NH_4)_2HPO_4$ nanosheets to pH >10. Scrolling under these conditions is likely facilitated by the HPO_4^{2-} anion, which is the dominant phosphate species at this pH. Finally, $Mn_3(PO_4)_2{\cdot}3H_2O$ nanosheets were able to scroll post-synthesis by reacting under solvothermal conditions of 25:5 DEG:H_2O at 250 °C. The $Mn_3(PO_4)_2{\cdot}3H_2O$ product consisted of twisted and untwisted nanobelts of $Mn_3(PO_4)_2{\cdot}3H_2O$ >10 µm as well as nanoscrolls. The remarkably different $Mn_3(PO_4)_2{\cdot}3H_2O$ morphology suggests that this compound undergoes dissolution and renucleation under these conditions, facilitated by DEG at this temperature.

Overall, manganese (II) phosphate compounds exhibit a rich degree of chemistry. However, these compounds make up just a small subset of the many different structures and morphologies in the class of metal (II) phosphates. Chapter V describes future applications of this research. There are many different directions to take these projects, including applying this chemical insight to other metal phosphate systems, such as the other olivine phosphates ($LiMPO_4$, M = Fe, Co, Ni) and $M_3(PO_4)_2{\cdot}8H_2O$ (M = Fe, Co). There are also several enticing applications for $Mn_3(PO_4)_2{\cdot}3H_2O$ nanoscrolls and nanosheets, including as water oxidation catalysts and as supercapacitors. Furthermore, δ-$Mn_3(PO_4)_2$ in particular shows promise as a molecular sieve, due to its microporous open-framework structure. Finally, other potential applications for this compound include anode materials for lithium-ion batteries and as water oxidation catalysts.

References

[1] L. Lu, X. Han, J. Li, J. Hua and M. Ouyang, *Journal of Power Sources* **2013**, *226*, 272-288.

[2] B. Scrosati, J. Hassoun and Y.-K. Sun, *Energy & Environmental Science* **2011**, *4*, 3287.

[3] J. Wen, Y. Yu and C. Chen, *Materials Express* **2012**, *2*, 197-212.

[4] C. Julien, A. Mauger, A. Vijh and K. Zaghib, *Lithium batteries: science and technology*, Springer, **2015**, p.

[5] S. S. Zhang, *Journal of Power Sources* **2006**, *162*, 1379-1394.

[6] M. Wakihara and O. Yamamoto, *Lithium ion batteries: fundamentals and performance*, John Wiley & Sons, **2008**, p.

[7] Y. Oumellal, N. Delpuech, D. Mazouzi, N. Dupré, J. Gaubicher, P. Moreau, P. Soudan, B. Lestriez and D. Guyomard, *Journal of Materials Chemistry* **2011**, *21*, 6201.

[8] T. Ohzuku, A. Ueda and N. Yamamoto, *Journal of The Electrochemical Society* **1995**, *142*, 1431-1435.

[9] C. Y. Ouyang, Z. Y. Zhong and M. S. Lei, *Electrochemistry Communications* **2007**, *9*, 1107-1112.

[10] J. N. Reimers and J. R. Dahn, *Journal of The Electrochemical Society* **1992**, *139*, 2091-2097.

[11] G. G. Amatucci, C. N. Schmutz, A. Blyr, C. Sigala, A. S. Gozdz, D. Larcher and J. M. Tarascon, *Journal of Power Sources* **1997**, *69*, 11-25.

[12] D. P. Abraham, E. P. Roth, R. Kostecki, K. McCarthy, S. MacLaren and D. H. Doughty, *Journal of Power Sources* **2006**, *161*, 648-657.

[13] A. K. Padhi, K. S. Nanjundaswamy and J. B. Goodenough, *Journal of The Electrochemical Society* **1997**, *144*, 1188-1194.

[14] D. M. C. Huminicki and F. C. Hawthorne, *Reviews in Mineralogy and Geochemistry* **2002**, *48*, 123-253.

[15] A. K. Padhi, K. S. Nanjundaswamy, C. Masquelier, S. Okada and J. B. Goodenough, *Journal of The Electrochemical Society* **1997**, *144*, 1609-1613.

[16] V. Aravindan, J. Gnanaraj, Y.-S. Lee and S. Madhavi, *Journal of Materials Chemistry A* **2013**, *1*, 3518.

[17] D. Choi, D. Wang, I.-T. Bae, J. Xiao, Z. Nie, W. Wang, V. V. Viswanathan, Y. J. Lee, J.-G. Zhang, G. L. Graff, Z. Yang and J. Liu, *Nano Letters* **2010**, *10*, 2799-2805.

[18] A. Yamada and S.-C. Chung *Journal of The Electrochemical Society* **2001**, *148*, A960-A967.

[19] F. Zhou, K. Kang, T. Maxisch, G. Ceder and D. Morgan, *Solid State Communications* **2004**, *132*, 181-186.

[20] Y.-D. Cho, G. T.-K. Fey and H.-M. Kao, *Journal of Power Sources* **2009**, *189*, 256-262.

[21] H. Li and H. Zhou, *Chem Commun (Camb)* **2012**, *48*, 1201-1217.

[22] L.-e. Li, J. Liu, L. Chen, H. Xu, J. Yang and Y. Qian, *RSC Advances* **2013**, *3*, 6847.

[23] K. Su, F. Liu and J. Chen, *Journal of Power Sources* **2013**, *232*, 234-239.

[24] *Proceedings of the Royal Society of London. Series A - Mathematical and Physical Sciences* **1937**, *161*, 220-235.

[25] Z. X. Nie, C. Y. Ouyang, J. Z. Chen, Z. Y. Zhong, Y. L. Du, D. S. Liu, S. Q. Shi and M. S. Lei, *Solid State Communications* **2010**, *150*, 40-44.

[26] M. S. Islam, D. J. Driscoll, C. A. J. Fisher and P. R. Slater, *Chemistry of Materials* **2005**, *17*, 5085-5092.

[27] X. Qin, J. Wang, J. Xie, F. Li, L. Wen and X. Wang, *Phys Chem Chem Phys* **2012**, *14*, 2669-2677.

[28] S.-Y. Chung, S.-Y. Choi, T. Yamamoto and Y. Ikuhara, *Angewandte Chemie International Edition* **2009**, *48*, 543-546.

[29] A. Paolella, G. Bertoni, P. Hovington, Z. Feng, R. Flacau, M. Prato, M. Colombo, S. Marras, L. Manna, S. Turner, G. Van Tendeloo, A. Guerfi, G. P. Demopoulos and K. Zaghib, *Nano Energy* **2015**, *16*, 256-267.

[30] A. Paolella, S. Turner, G. Bertoni, P. Hovington, R. Flacau, C. Boyer, Z. Feng, M. Colombo, S. Marras, M. Prato, L. Manna, A. Guerfi, G. P. Demopoulos, M. Armand and K. Zaghib, *Nano Lett* **2016**, *16*, 2692-2697.

[31] J. Chen, S. Wang and M. S. Whittingham, *Journal of Power Sources* **2007**, *174*, 442-448.

[32] Y. Zhang, Y.-W. Tan, H. L. Stormer and P. Kim, *Nature* **2005**, *438*, 201.

[33] C. Lee, X. Wei, J. W. Kysar and J. Hone, *Science* **2008**, *321,* 385-388.

[34] P. Blake, P. D. Brimicombe, R. R. Nair, T. J. Booth, D. Jiang, F. Schedin, L. A. Ponomarenko, S. V. Morozov, H. F. Gleeson, E. W. Hill, A. K. Geim and K. S. Novoselov, *Nano Letters* **2008**, *8*, 1704-1708.

[35] K. S. Novoselov, A. K. Geim, S. V. Morozov, D. Jiang, Y. Zhang, S. V. Dubonos, I. V. Grigorieva and A. A. Firsov, *Science* **2004**, *306*, 666-669.

[36] P. Joensen, R. F. Frindt and S. R. Morrison, *Materials Research Bulletin* **1986**, *21*, 457-461.

[37] A. O’Neill, U. Khan and J. N. Coleman, *Chemistry of Materials* **2012**, *24*, 2414-2421.

[38] Y. Hernandez, V. Nicolosi, M. Lotya, F. M. Blighe, Z. Sun, S. De, I. T. McGovern, B. Holland, M. Byrne, Y. K. Gun'Ko, J. J. Boland, P. Niraj, G. Duesberg, S. Krishnamurthy, R. Goodhue, J. Hutchison, V. Scardaci, A. C. Ferrari and J. N. Coleman, *Nature Nanotechnology* **2008**, *3*, 563.

[39] T. Sasaki and M. Watanabe, *The Journal of Physical Chemistry B* **1997**, *101*, 10159-10161.

[40] T. Tanaka, Y. Ebina, K. Takada, K. Kurashima and T. Sasaki, *Chemistry of Materials* **2003**, *15*, 3564-3568.

[41] Y. Omomo, T. Sasaki, Wang and M. Watanabe, *Journal of the American Chemical Society* **2003**, *125*, 3568-3575.

[42] K. Fukuda, I. Nakai, Y. Ebina, R. Ma and T. Sasaki, *Inorganic Chemistry* **2007**, *46*, 4787-4789.

[43] K. Fukuda, K. Akatsuka, Y. Ebina, R. Ma, K. Takada, I. Nakai and T. Sasaki, *ACS Nano* **2008**, *2*, 1689-1695.

[44] R. E. Schaak and T. E. Mallouk, *Chemistry of Materials* **2000**, *12*, 3427-3434.

[45] A. Takagaki, T. Yoshida, D. Lu, J. N. Kondo, M. Hara, K. Domen and S. Hayashi, *The Journal of Physical Chemistry B* **2004**, *108*, 11549-11555.

[46] M. B. Dines, *Materials Research Bulletin* **1975**, *10*, 287-291.

[47] Z. Zeng, Z. Yin, X. Huang, H. Li, Q. He, G. Lu, F. Boey and H. Zhang, *Angewandte Chemie International Edition* **2011**, *50*, 11093-11097.

[48] W. Shi, S. Song and H. Zhang, *Chem Soc Rev* **2013**, *42*, 5714-5743.

[49] T. Sasaki, M. Watanabe, Y. Michiue, Y. Komatsu, F. Izumi and S. Takenouchi, *Chemistry of materials* **1995**, *7*, 1001-1007.

[50] X. Han, Q. Kuang, M. Jin, Z. Xie and L. Zheng, *Journal of the American Chemical Society* **2009**, *131*, 3152-3153.

[51] Z. Sun, T. Liao, Y. Dou, S. M. Hwang, M. S. Park, L. Jiang, J. H. Kim and S. X. Dou, *Nat Commun* **2014**, *5*, 3813.

[52] H. Duan, N. Yan, R. Yu, C. R. Chang, G. Zhou, H. S. Hu, H. Rong, Z. Niu, J. Mao, H. Asakura, T. Tanaka, P. J. Dyson, J. Li and Y. Li, *Nat Commun* **2014**, *5*, 3093.

[53] A.-X. Yin, W.-C. Liu, J. Ke, W. Zhu, J. Gu, Y.-W. Zhang and C.-H. Yan, *Journal of the American Chemical Society* **2012**, *134*, 20479-20489.

[54] X. Huang, S. Tang, X. Mu, Y. Dai, G. Chen, Z. Zhou, F. Ruan, Z. Yang and N. Zheng, *Nat Nanotechnol* **2011**, *6*, 28-32.

[55] X. Huang, S. Li, Y. Huang, S. Wu, X. Zhou, S. Li, C. L. Gan, F. Boey, C. A. Mirkin and H. Zhang, *Nature Communications* **2011**, *2*, 292.

[56] X. J. Wu, X. Huang, J. Liu, H. Li, J. Yang, B. Li, W. Huang and H. Zhang, *Angew Chem Int Ed Engl* **2014**, *53*, 5083-5087.

[57] X. Rui, X. Zhao, Z. Lu, H. Tan, D. Sim, H. H. Hng, R. Yazami, T. M. Lim and Q. Yan, *ACS Nano* **2013**, *7*, 5637-5646.

[58] N. P. W. Pieczonka, Z. Liu, A. Huq and J.-H. Kim, *Journal of Power Sources* **2013**, *230*, 122-129.

[59] C. Delacourt, P. Poizot, M. Morcrette, J. M. Tarascon and C. Masquelier, *Chemistry of Materials* **2004**, *16*, 93-99.

[60] S.-L. Yang, R.-G. Ma, M.-J. Hu, L.-J. Xi, Z.-G. Lu and C. Y. Chung, *Journal of Materials Chemistry* **2012**, *22*, 25402.

[61] K. Jin, J. Park, J. Lee, K. D. Yang, G. K. Pradhan, U. Sim, D. J. Jeong, H. L., S. Park, D. Kim, N. E. Sung, S. H. Kim, S. Han and K. T. Nam, *J Am Chem Soc* **2014**, *136*, 7435-7443.

[62] J. S. Stephens and C. Calvo, *Canadian Journal of Chemistry* **1969**, *47*, 2215-2225.

[63] A. NORD and H. ANNERSTEN, *Acta chemica Scandinavica. Series A. Physical and inorganic chemistry* **1987**, *41*, 56-58.

[64] W. Massa, O. V. Yakubovich and O. V. Dimitrova, *Solid State Sciences* **2005**, *7*, 950-956.

[65] G. Neher and T. T. Salguero, *Crystal Growth & Design* **2017**.

[66] Z. Li, Z. Peng, H. Zhang, T. Hu, M. Hu, K. Zhu and X. Wang, *Nano Lett* **2016**, *16*, 795-799.

CHAPTER 2

δ-POLYMORPH OF MANGANESE PHOSPHATE

Neher, G. and Salguero, T.T. *Crystal Growth & Design* **2017,** *17* (9), 4864-4872. Reprinted here with permission of the publisher.

Abstract

A fourth polymorph of manganese phosphate, δ-$Mn_3(PO_4)_2$, crystallizes in the monoclinic space group $P2_1/c$ with lattice parameters a = 8.9234(6) Å, b = 9.1526(6) Å, c = 8.6587(5) Å, β = 111.6670(10)°, V = 657.21(7) Å^3, and Z = 4. Its structure features planes of [MnO_5] pentahedra edge-shared with [PO_4] tetrahedra, resulting in a three dimensional framework containing sub-nanometer channels. Both hydrothermal and solid-state synthesis routes can yield δ-$Mn_3(PO_4)_2$. In one method, the hydrothermal treatment of $Mn_5(PO_4)_2(PO_3OH)_2{\cdot}4H_2O$ (hureaulite) at 250 °C for 1-6 h yields δ-$Mn_3(PO_4)_2$ microcrystals; changing the precursor to $Mn_3(PO_4)_2{\cdot}3H_2O$ nanosheets leads to δ-$Mn_3(PO_4)_2$ nanoplates. A time study of δ-$Mn_3(PO_4)_2$ formation under hydrothermal conditions suggests a dissolution-nucleation mechanism. Alternatively, the solid state reaction of $LiMnPO_4$ and β'-$Mn_3(PO_4)_2$ in a 1:2 molar ratio under air-free conditions at 1,000 °C produces δ-$Mn_3(PO_4)_2$. DSC and variable temperature XRD measurements show that δ-$Mn_3(PO_4)_2$ is stable to 735 °C, beyond which it transforms into β'-$Mn_3(PO_4)_2$. The δ-$Mn_3(PO_4)_2$ $\rightarrow$ β'-$Mn_3(PO_4)_2$ conversion also occurs by hydrothermal treatment at 250 °C for 24 h.

Introduction

A variety of metal(II) phosphates have emerged as useful materials in recent years. In the case of manganese(II), manganese phosphate trihydrate $Mn_3(PO_4)_2{\cdot}3H_2O$, has applications as a water oxidation catalyst,[1] supercapacitor material,[2] and precursor to $LiMnPO_4$ used for Li-ion battery cathodes.[3] However, relatively little chemistry is known for the anhydrous analog of manganese phosphate, $Mn_3(PO_4)_2$ (also known as manganese orthophosphate). As is typical for simple inorganic compounds, $Mn_3(PO_4)_2$ crystallizes in several polymorphic forms (Table 2.1). The thermodynamically stable form, characterized by Calvo and Stephens in 1987, was designated β'-$Mn_3(PO_4)_2$ because of structural similarities to β-$Zn_3(PO_4)_2$.[4] Subsequent researchers refined the structure using crystals grown by chemical vapor transport.[5] Nord and Annersten characterized an α-$Mn_3(PO_4)_2$ form prepared at elevated temperatures and pressures; this polymorph is isomorphous with the mineral graftonite $(Fe,Mn,Ca)_3(PO_4)_2$.[6] A third polymorph, γ-$Mn_3(PO_4)_2$, was synthesized under hydrothermal conditions by Massa and coworkers.[7] All three polymorphs crystallize in the $P2_1/c$ ($P2_1/n$) space group, contain both of five- and six-coordinate manganese(II), and exhibit low temperature antiferromagnetic ground states, as recently demonstrated by Vasiliev and coworkers.[8]

Table 2.1
Distinguishing features of manganese phosphate polymorphs

Polymorph	Synthesis	Space Group (No. 14)	Unit Cell Parameters		Volume (Å^3)	Z	Density	Reference
			a, b, c (Å)	*β* (°)			g/cm^3	
α-$Mn_3(PO_4)_2$	Solid-state ≥ 826 °C	$P2_1/c$	8.817(7) 11.455(6) 6.244(5)	98.96(7)	622.8	4	3.789	6
β'-$Mn_3(PO_4)_2$	Solid-state ≥ 800 °C	$P2_1/c$	8.948(2) 10.050(2) 24.084(2)	120.5(1)	1866.1	12	3.7882	4
γ-$Mn_3(PO_4)_2$	Hydrothermal 270 °C	$P2_1/n$	5.2344(5) 6.6739(7) 8.9688(10)	95.276(9)	312.0	2	3.7764	7
δ-$Mn_3(PO_4)_2$	Hydrothermal 250 °C Solid-state 900-1000 °C	$P2_1/c$	8.9234(6) 9.1526(6) 8.6587(5)	111.6670(10)	657.21(7)	4	3.5855	this work

Of these $Mn_3(PO_4)_2$ polymorphs, only β'-$Mn_3(PO_4)_2$ has been used as a precursor for further chemical synthesis. Clemens and coworkers reported a solid-state route to a range of compounds $Li_xMn_{1.5-x/2}PO_4$ ($0 \leq x \leq 1$) by reacting $LiMnPO_4$ and β'-$Mn_3(PO_4)_2$ under air-free conditions at 900 °C.[9] These products were studied by powder X-ray diffraction methods to gain a better understanding of the degree of aliovalent substitution (Li^+ by Mn^{2+}) in $LiMnPO_4$ and related materials, an important feature related to Li-ion battery cathodes with enhanced electronic and ionic conductivity.

In this contribution we describe a fourth polymorph of $Mn_3(PO_4)_2$. Based on IUCr nomenclature recommendations,[10] this new modification is formally designated "δ |<1008 K |$P2_1/c$ (14) |Z = 4 |likely antiferromagnetic|–"; however, we refer to it here simply as δ-$Mn_3(PO_4)_2$. In contrast to the other known polymorphs, δ-$Mn_3(PO_4)_2$ contains three unique five-coordinate manganese sites and no six-coordinate manganese sites. This feature is unusual in light of typical metal phosphate minerals, which contain at least one octahedral metal cation site in their structures.[11] We find that δ-$Mn_3(PO_4)_2$ is composed of chains of alternating [MnO_5] and [PO_4] moieties that (1) result in a porous structure with 2.14-3.84 Å diameter channels, and (2) cause the crystals to grow anisotropically in the [100] and [010] directions without the addition of structure-directing agents. Here we detail several synthetic routes to δ-$Mn_3(PO_4)_2$ and characterize its spectroscopic features and thermal stability.

Experimental

Materials: The following reagents were used as received: $MnSO_4·H_2O$ (J.T. Baker, 99%), $MnCl_2·4H_2O$ (J.T. Baker, 99.6%), $NH_4H_2PO_4$, (Sigma-Aldrich, 98%), $(NH_4)_2HPO_4$, (Sigma Aldrich, >98%), 0.1 M aqueous NaOH (Sigma-Aldrich 99%), MnO (Sigma-Aldrich, 99.99%), LiH_2PO_4 (Sigma-Aldrich, 99%), H_3PO_4 (Sigma-Aldrich, 35%).

Preparation of $Mn_5(PO_4)_2(PO_3OH)_2·4H_2O$: This procedure was adapted from the literature.[12] A solution of 1.3570 g (6.8567 mmol) of $MnCl_2·4H_2O$ in 20 mL nanopure H_2O and a solution of 0.5470 g (4.756 mmol) of $NH_4H_2PO_4$ in 20 mL nanopure H_2O were mixed together and refluxed for 7 h. The resulting white precipitate was isolated by centrifugation at 10,000 rpm and washed with 30 mL nanopure water 2x. The solids were dried in a vacuum oven overnight at 50 °C to provide 0.0368 g (3.7%) of white product.

Alternate preparation of $Mn_5(PO_4)_2(PO_3OH)_2·4H_2O$: 0.3445 g (1.741 mmol) of $MnCl_2·4H_2O$ was added to 150 mL of nanopure H_2O. Then 0.168 mL of 15.2 M H_3PO_4 (2.55 mmol) was added, and the resulting solution was transferred to a 250 mL round bottom flask. The solution was refluxed for 30 min. Then 25.0 mL of 0.1 M aqueous NaOH (2.50 mmol) was added dropwise to the refluxing solution. The solution changed from clear to cloudy white, consistent with $Mn_3(PO_4)_2·3H_2O$ formation. This reaction mixture was refluxed an additional 12 h. The white precipitate was isolated by centrifugation at 10,000 rpm and washed with 30 mL of distilled water 2x. The solids were dried in a vacuum oven overnight to provide 0.2593 g (75.1%) of white $Mn_5(PO_4)_2(PO_3OH)_2{\cdot}4H_2O$ powder.

Preparation of $Mn_3(PO_4)_2{\cdot}3H_2O$ nanosheets: This procedure was adapted from the literature.[13] A solution of 1.0370 g (6.1358 mmol) of $MnSO_4{\cdot}H_2O$ in 50 mL nanopure H_2O and a solution of 0.54500 g (4.1269 mmol) $(NH_4)_2HPO_4$ in 50 mL nanopure H_2O were mixed, which caused a milky white precipitate to form. This mixture was stirred at room temperature for 3 h. The resulting colloidal suspension was centrifuged at 10,000 rpm, and the solids were washed 3x with distilled H_2O. Vacuum drying provided 0.5588 g (67.8%) of white $Mn_3(PO_4)_2{\cdot}3H_2O$ powder.

Preparation of δ-$Mn_3(PO_4)_2$ nanoplates: 0.0500 g of $Mn_3(PO_4)_2{\cdot}3H_2O$ nanosheets were dispersed in 30 mL nanopure H_2O. This suspension was transferred to a 42 mL Teflon-lined autoclave and heated at 250 °C for 4 h. Afterwards, the off-white product was washed with nanopure H_2O and centrifuged at 10,000 rpm 3x. The solids were dried at 120 °C for 6 h to yield 0.0474 g (94.8%) of a cream-colored product.

δ-$Mn_3(PO_4)_2$ microcrystals: 0.0500 g of $Mn_5(PO_4)_2(PO_3OH)_2{\cdot}4H_2O$ were added to 30 mL of H_2O and transferred to a 42 mL Teflon-lined autoclave. The reaction was heated at 250 °C for 3 h. The resulting crystals were isolated by vacuum filtration, washed with nanopure H_2O and dried at 120 °C overnight. The yield of isolated colorless microcrystals was 0.0242 g (53.2%). Time studies were carried out by preparing multiple hydrothermal reactions and reacting each at 250 °C for a certain period of time. The resulting products were analyzed without any workup by washing.

Solid-State Synthesis of δ-$Mn_3(PO_4)_2$: This method is based on a procedure detailed by Clemens and coworkers.[9] The first precursor, $LiMnPO_4$, was synthesized by ball-milling 0.5522 g (5.313 mmol) of LiH_2PO_4 and 0.3769 g (5.313 mmol) of MnO at 300 RPM for 1 h with a Fritzch Pulverisette 6 Planetary Ball Mill with ~150 1-mm WC balls. The resulting powder was pressed into a pellet and calcined at 300 °C in air for 1 h in an alumina crucible. Then the pellet was added to an alumina boat and transferred into a quartz ampule. A second alumina boat filled halfway with MnO (as a sacrificial oxygen scavenger) was added to the ampule. The ampule was evacuated and back-filled with Ar 3x times, then sealed. The ampoule was heated at 900 °C for 15 h in a tube furnace to produce pure $LiMnPO_4$. The second precursor, β'-$Mn_3(PO_4)_2$, was prepared in a similar way using 0.5950 g (4.505 mmol) of $(NH_4)_2HPO_4$ and 0.4798 g (6.768 mmol) of MnO reacted at 900 °C for 15 h. Then, to produce δ-$Mn_3(PO_4)_2$, 0.3000 g (0.8456 mmol) of β'-$Mn_3(PO_4)_2$ and 0.0667 g (0.425 mmol) of $LiMnPO_4$ were ball-milled using the same conditions described earlier. The mixture was then pressed into a pellet and calcined at 300 °C in air for 1 h in an alumina crucible. Afterwards, it was added to an ampoule, sealed (with MnO) and reacted at 1,000 °C for 9 h, resulting in a white powder containing δ-$Mn_3(PO_4)_2$.

Characterization: X-ray diffraction (XRD) data were collected on two diffractometers: a Bruker D8 instrument utilizing a Co-Kα X-ray source (λ =1.78890 Å) operated at 40 kV and 40 mA, and a PANalytical X'Pert instrument utilizing a Cu-Kα X-ray source (λ = 1.5418 Å) operated at 40 kV and 40 mA. In both cases, data were collected from 5-80° 2θ with a scan rate of 0.1 s/step. Samples were prepared as powder mounts or drop cast from solution.

For single crystal X-ray diffraction, the selected colorless crystal of δ-$Mn_3(PO_4)_2$ was mounted on the tip of a glass fiber. The X-ray intensity data were measured at room temperature on a Bruker SMART APEX II X-ray diffractometer system with graphite-monochromated Mo

Kα radiation (λ = 0.71073 Å) using the ω-scan technique. The data was collected in 1464 frames with 10 s exposure times. Additional details are provided in the SI.

Transmission electron microscopy (TEM) imaging and selected area electron diffraction (SAED) analyses were performed on an FEI Tecnai 20 transmission electron microscope with an accelerating voltage of 200 kV. Samples were drop cast onto Formvar grids and air dried. High resolution transmission electron microscopy (HRTEM) was performed with a Hitachi H9500 transmission electron microscope operating at 300 kV. Samples were drop cast onto holey carbon grids.

Scanning electron microscopy (SEM) analysis was performed using an FEI Teneo FE-SEM at 10 kV with a spot size of 10. Samples were dropcast onto a silicon wafer.

For atomic force microscopy (AFM), samples were dispersed in water, bath sonicated for 10 min, and centrifuged at 4,000 rpm for 10 min. The top portion of the dispersion was drop cast onto a clean Si wafer. Data were collected with a Bruker Innova instrument in tapping mode. AFM data were analyzed with Nanoscope Analysis software.

Differential scanning calorimetry (DSC) was performed by NETZSCH Instruments North America, LLC, on a NETZSCH model DSC 404 F1 *Pegasus* differential scanning calorimeter. Data were collected in the temperature range of 25–1000 °C with a heating ramp of 10 °C min^{-1} under a flowing Ar atmosphere (50 mL min^{-1}).

Combination thermogravimetric analysis (TGA)–mass spectrometry (MS) was performed on a TA Instruments Discovery TGA under an N_2 flow from 26–1,000 °C using a temperature ramp of 10 °C min^{-1}. IR spectra were collected with a Bruker Tensor 37 spectrometer in scanning mode from 500-4000 cm^{-1}. Raman spectra were collected with a Renishaw InVia Laser spectrometer with a diode laser operating at 785 nm. Solid samples were deposited on a quartz slide and run with an acquisition time of 30 s, 0.1% laser power, and a 20x objective lens. Typical resolution was approximately 2 cm^{-1}. The spectrometer was calibrated with an internal Si reference (521 cm^{-1}). Spectra were baseline-corrected in OriginPro 8.5; cosmic ray spikes also were removed using this software. XPS data were collected using an X-ray source (Staib Instruments) and a hemispherical analyzer (Leybold Heraeus) under UHV conditions.

Results and Discussion

Advantageously, δ-$Mn_3(PO_4)_2$ can be accessed through several routes that are summarized in Scheme 2.1. The convenient hydrothermal reactions start from $Mn_3(PO_4)_2{\cdot}3H_2O$ or $Mn_5(PO_4)_2(PO_3OH)_2{\cdot}4H_2O$ precursors. We prepared $Mn_3(PO_4)_2{\cdot}3H_2O$ in 65–70% yield by the aqueous reaction of $MnSO_4{\cdot}H_2O$ and $(NH_4)_2HPO_4$, which is based on the method reported by Chung and coworkers with our modification of using $(NH_4)_2HPO_4$ rather than Li_3PO_4 as the phosphate source.[13] $Mn_3(PO_4)_2{\cdot}3H_2O$ precipitates as nanosheets that vary from 0.2 to 2 µm in lateral dimensions (determined by TEM imaging, Figure S2.1A), and have thicknesses in the range of 10–35 nm (determined by AFM imaging, Figures S2.1D-E). The measured d-spacings from the SAED pattern from these nanosheets corresponds to the (002) plane of $Mn_3(PO_4)_2{\cdot}3H_2O$ (Figure S2.1C). Although the powder X-ray diffraction pattern of our synthesized material indexes appropriately to previously reported $Mn_3(PO_4)_2{\cdot}3H_2O$ (Figure S2.1C), the published crystallographic study of $Mn_3(PO_4)_2{\cdot}3H_2O$ lacks atomic coordinates. However, Nam and coworkers have modeled a likely structure based on $Mn_3(PO_4)_2{\cdot}7H_2O$ minus four water molecules.[1] The resulting calculated structure of $Mn_3(PO_4)_2{\cdot}3H_2O$ contains sheets of edge- and corner-shared [MnO_6], [MnO_5], and [PO_4] polyhedra extending in the [100] and [010] directions. The two-dimensional morphology of $Mn_3(PO_4)_2{\cdot}3H_2O$ nanosheets is a direct consequence of this layered crystal structure. Such anisotropic crystal growth resulting in two-dimensional morphologies is a feature shared by other hydrated metal phosphates like $NH_4MPO_4{\cdot}H_2O$ (M = Mn, Fe, Co, Ni).[14],[15] In the case of $Mn_3(PO_4)_2{\cdot}3H_2O$, each unit cell (Z = 4) contains twelve water molecules, where eight bridge [MnO_6] polyhedra and two are bound to [MnO_5]. The two remaining water molecules reside between the (001) planes. Our thermogravimetric analysis of $Mn_3(PO_4)_2 \cdot 3H_2O$ is consistent with this structure. The TGA data provides a total mass loss of 12.6% in the range 25–1,000 °C, corresponding to the three water molecules of hydration (Figure S2.1F). The first mass loss of 4.4% can be attributed to the two non-bonded water molecules plus the two water molecules bonded to [MnO_5]. The second mass loss of 8.2% corresponds to the more strongly bonded eight water molecules that bridge the [MnO_5] pentahedra.

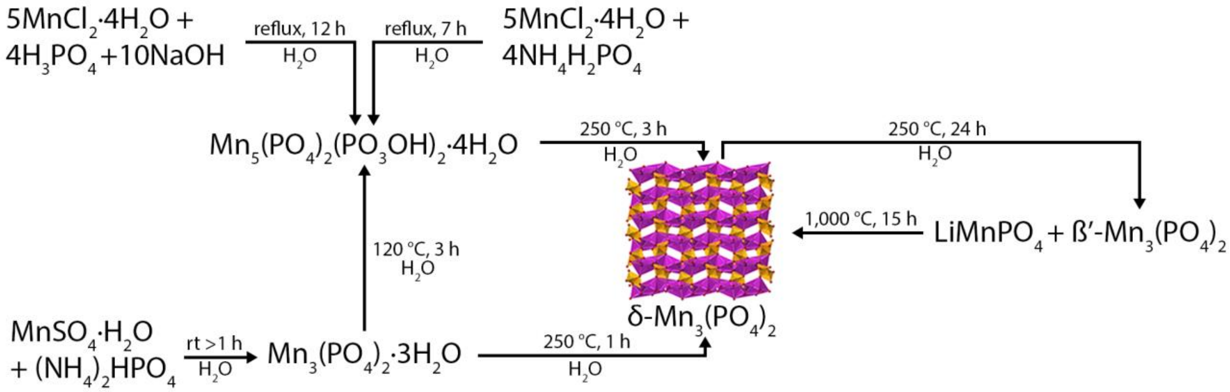

Scheme 2.1: Hydrothermal and solid state routes to δ-$Mn_3(PO_4)_2$.

The hydrothermal treatment of $Mn_3(PO_4)_2 \cdot 3H_2O$ nanosheets at 250 °C for >1 h results in δ-$Mn_3(PO_4)_2$ nanoplates in 68% isolated yield. The resulting washed and dried white powder easily re-disperses in water to produce a highly pearlescent, colloidal dispersion. The X-ray diffraction pattern (Figure 2.1D) matches single crystal data (*vide infra*), with the notable appearance of an intense peak at 21.38° 2θ corresponding to the (020) reflection. The relative intensity of this peak compared to the others is a strong indicator of oriented growth and the presence of preferred orientation effects in the resulting sample. ICP-OES confirms the stoichiometry of δ-$Mn_3(PO_4)_2$ with an atomic ratio of approximately 3.2 to 2.0 manganese to phosphorous (Table S2.1). As seen by both AFM and TEM imaging, δ-$Mn_3(PO_4)_2$ nanoplates exhibit straight edges with lateral dimensions from 5-20 µm (Figure 2.1A-B). SEM imaging shows that these nanoplates are typically 10–40 µm in length, with some smaller nanoplates <10 µm also present in the sample (Figure 2.1C). AFM analysis of a representative nanoplate indicates a typical thickness of ca. 150 nm (Figure 2.1A). The SAED pattern of these nanoplates reveals their single crystalline nature (Figure 2.1E), with the measured d-spacings corresponding to the (002) plane of δ-$Mn_3(PO_4)_2$ rather than the (020) plane suggested by the powder XRD data. HRTEM data further supports the (002) orientation. Figure 1F shows the lattice fringes of a δ-$Mn_3(PO_4)_2$ nanoplate with an average measured value of 0.446 nm. The corresponding fast Fourier transform (FFT) provides d-spacings of 0.419 nm and 0.456 nm, which are in good agreement with the calculated values of 0.415 nm and 0.458 nm for the d-spacings of the (200) and (020) planes of δ-$Mn_3(PO_4)_2$, respectively.

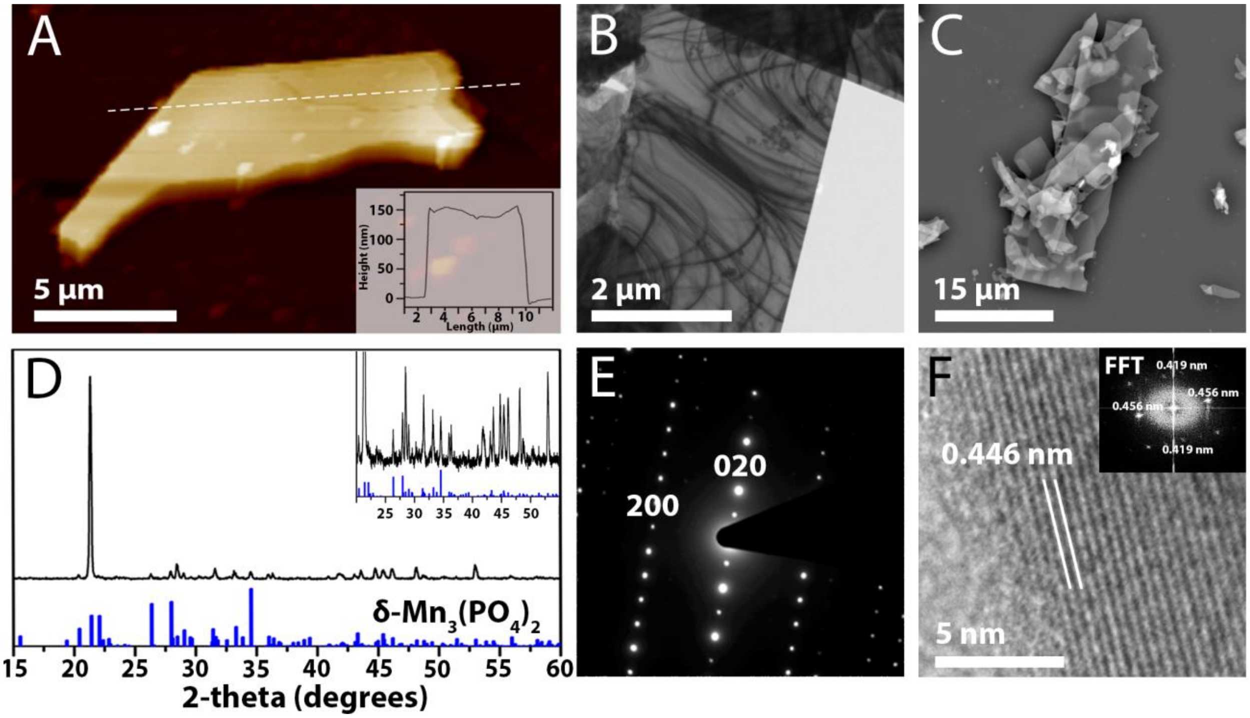

Figure 2.1. Characterization of δ-$Mn_3(PO_4)_2$: A) AFM image of a typical δ-$Mn_3(PO_4)_2$ nanoplate, with the height profile (inset). B and C) TEM and SEM images of $Mn_3(PO_4)_2$ nanoplate, respectively. D) Powder XRD (Cu X-ray Source) pattern of δ-$Mn_3(PO_4)_2$ nanoplate, with calculated pattern (blue drop lines) and magnification of 20-55° 2θ region (inset). E) SAED pattern from the δ-$Mn_3(PO_4)_2$ nanoplate in panel B. F) HRTEM of δ-$Mn_3(PO_4)_2$ with FFT (inset).

Interestingly, the same reaction of $Mn_3(PO_4)_2 \cdot 3H_2O$ nanoplates at a lower temperature of 120 °C yields $Mn_5(PO_4)_2(PO_3OH)_2 \cdot 4H_2O$ instead of δ-$Mn_3(PO_4)_2$. In mineral form, $(Mn,Fe)_5(PO_4)_2(PO_3OH)_2 \cdot 4H_2O$ is known as hureaulite.[16] A time study at 120 °C showed that this product forms at reaction times greater than 12 h, which was monitored by the appearance of XRD peaks that index to the (*h*00) series of $Mn_5(PO_4)_2(PO_3OH)_2 \cdot 4H_2O$. This result is not surprising because $Mn_5(PO_4)_2(PO_3OH)_2 \cdot 4H_2O$ is known to form from $Mn_3(PO_4)_2 \cdot 3H_2O$ under aqueous reflux conditions.[17] Additionally, the solubility constants of –30.70 log K° for $Mn_3(PO_4)_2 \cdot 3H_2O$ and –73.44 log K° for $Mn_5(PO_4)_2(PO_3OH)_2 \cdot 4H_2O$ suggest that the precipitation of $Mn_5(PO_4)_2(PO_3OH)_2 \cdot 4H_2O$ is favored by its lower solubility.[18] For these reasons, it is likely that $Mn_5(PO_4)_2(PO_3OH)_2 \cdot 4H_2O$ forms as an intermediate in the hydrothermal chemistry leading to δ-$Mn_3(PO_4)_2$.

The synthesis of δ-$Mn_3(PO_4)_2$ directly from $Mn_5(PO_4)_2(PO_3OH)_2 \cdot 4H_2O$ provides evidence for this hypothesis. We have prepared this precursor successfully by two routes. The first is based on a published procedure in which an aqueous solution of $MnCl_2$ and NH_4HPO_4 is refluxed for 12 h.[12] Because the isolated yield of $Mn_5(PO_4)_2(PO_3OH)_2 \cdot 4H_2O$ from this synthesis is <5%, we optimized an alternate procedure that utilizes H_3PO_4, NaOH, and $MnCl_2$ according to Eq. 2.1:

$$5MnCl_2 + 4H_3PO_4 + 10NaOH \rightarrow Mn_5(PO_4)_2(PO_3OH)_2 \cdot 4H_2O + 10NaCl + 6H_2O \quad (2.1)$$

The isolated yield of $Mn_5(PO_4)_2(PO_3OH)_2 \cdot 4H_2O$ from this reaction is a much-improved ~75%. The morphology of the products from the two syntheses is slightly different: the literature procedure provides prism-like aggregates tens of microns in length whereas our modified procedure provides sub-10 μm aggregates with distinctive stepped crystal facets (Figure S2.3).

The hydrothermal treatment of $Mn_5(PO_4)_2(PO_3OH)_2 \cdot 4H_2O$ at 250 °C for 1-6 h provides δ-$Mn_3(PO_4)_2$ in the form of microcrystals with lateral dimensions greater than 100 μm (Figure S4)—significantly larger than the nanoplates formed from $Mn_3(PO_4)_2 \cdot 3H_2O$ nanosheets. These larger crystals allowed us to determine the crystal structure of δ-$Mn_3(PO_4)_2$ by single crystal X-ray diffraction, as described in the next section. We propose that δ-$Mn_3(PO_4)_2$ forms according to Eq. 2.2 via the dissolution of $Mn_5(PO_4)_2(PO_3OH)_2 \cdot 4H_2O$ followed by nucleation of δ-$Mn_3(PO_4)_2$:

$$3Mn_5(PO_4)_2(PO_3OH)_2 \cdot 4H_2O\ (s) \rightarrow 5\ \delta\text{-}Mn_3(PO_4)_2\ (s) + 2H_2PO_4^-\ (aq) + 12H_2O + 2H^+ \quad (2.2)$$

Notably, the hydrothermal syntheses of δ-$Mn_3(PO_4)_2$ described here do not include intentional structure directing agents or coordinating solvents to assist in the formation of two-dimensional morphologies. In general, many bottom-up syntheses that provide nanosheets or platelets employ organic surfactants or coordinating solvents that control growth in certain directions by binding to specific faces of the nucleating crystal.[19] Common solvents for the directed growth of metal phosphates include ethylene glycol and diethylene glycol.[20]

To better understand the crystal growth of δ-$Mn_3(PO_4)_2$, we performed a time study. Because the hydrothermal reaction starting with $Mn_3(PO_4)_2{\cdot}3H_2O$ proceeds quite rapidly (<1 h), we instead monitored the hydrothermal reaction starting with $Mn_5(PO_4)_2(PO_3OH)_2{\cdot}4H_2O$ over the course of 24 h at 250 °C. Figure 2.2 shows SEM images and PXRD data for six time points. The initial reaction mixture contains $Mn_5(PO_4)_2(PO_3OH)_2{\cdot}4H_2O$ aggregates (Figure 2.2B). After 2 h of reaction at 250 °C, flower-like microcrystals of δ-$Mn_3(PO_4)_2$ begin to form alongside unreacted $Mn_5(PO_4)_2(PO_3OH)_2{\cdot}4H_2O$ (Figure 2.2C). After 3 h of reaction, $Mn_5(PO_4)_2(PO_3OH)_2{\cdot}4H_2O$ is consumed completely, with the sole crystalline product being δ-$Mn_3(PO_4)_2$ (Figure 2.2D).

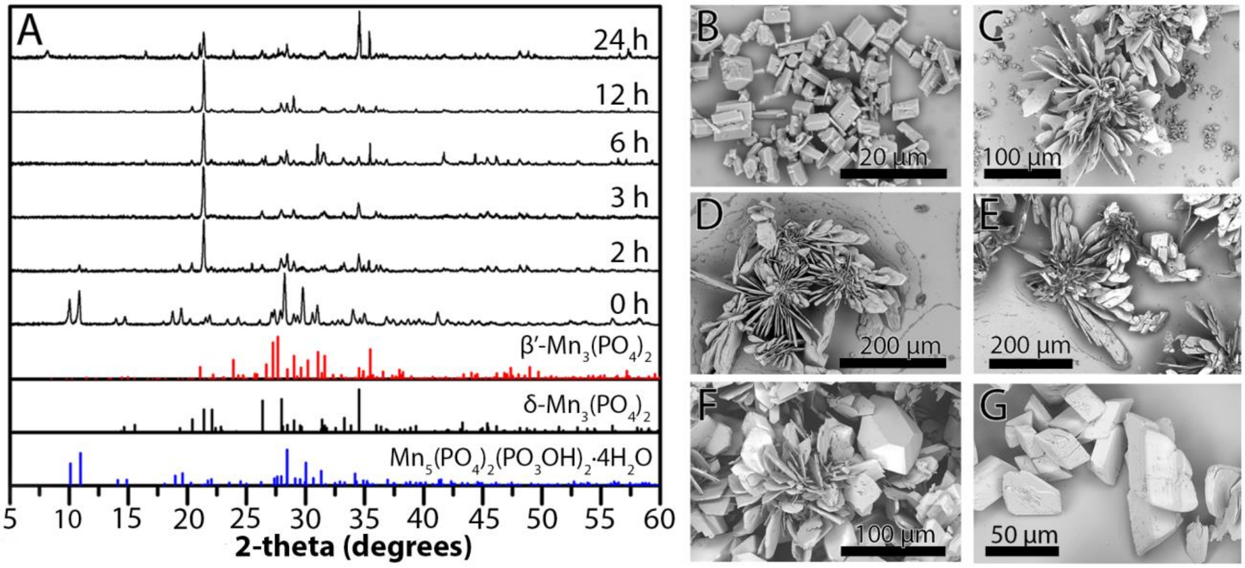

Figure 2.2 Time study of δ-$Mn_3(PO_4)_2$ formation by the hydrothermal reaction of $Mn_5(PO_4)_2(PO_3OH)_2 \cdot 4H_2O$ at 250 °C for 0-24 h: A) XRD patterns at different time points (Cu X-ray source). Blue drop lines correspond to $Mn_5(PO_4)_2(PO_3OH_2) \cdot 4H_2O$ (JCPDS #00-034-0146), black drop lines correspond to δ-$Mn_3(PO_4)_2$ (this work), and red drop lines correspond to β'-$Mn_3(PO_4)_2$ (JCPDS #04-012-2502). B-G) SEM of reaction mixtures at corresponding time periods: B) 0 h, C) 2 h, D), 3 h, E) 6 h, F) 12 h, and G) 24 h.

This progression suggests a dissolution-nucleation mechanism, starting with the dissolution of $Mn_5(PO_4)_2(PO_3OH)_2 \cdot 4H_2O$ and culminating in the nucleation of flower-like δ-$Mn_3(PO_4)_2$ microcrystals. Similar flower-like crystal growth is widely described in the literature to proceed via a nucleation step, followed by crystallization, self-assembly, oriented growth and finally Ostwald ripening.[21] In the case of hydrothermal δ-$Mn_3(PO_4)_2$ formation, it is possible that $H_2PO_4^-$ generated by Eq. 2 influences crystal growth, helping to explain the nanoplate versus microcrystal δ-$Mn_3(PO_4)_2$ products when starting from $Mn_3(PO_4)_2 \cdot 3H_2O$ versus $Mn_5(PO_4)_2(PO_3OH)_2 \cdot 4H_2O$. For example, Xu and coworkers have proposed that SO_4^{2-} ions selectively bind to specific faces of $LiMnPO_4$ during hydrothermal growth and thus are in part responsible for the flower-like morphology of the product.[22]

Upon continuing the time study, we see a new compound appearing after 6 h of reaction at 250 °C. Crystals with a prism-like morphology (Figure 2.2E) coincide with new peaks in the diffraction pattern, which correspond to β'-$Mn_3(PO_4)_2$ (JCPDS #04-012-2502). By the 24 h time point, most of the δ-$Mn_3(PO_4)_2$ has been converted to this species (Figure 2.2G). The formation of β'-$Mn_3(PO_4)_2$ under these conditions is surprising based on the lack of any prior hydrothermal synthesis of this polymorph, which has been prepared by solid state reactions at ≥ 800 °C.[4-5, 8] The formation of β'-$Mn_3(PO_4)_2$ from $Mn_5(PO_4)_2(PO_3OH)_2{\cdot}4H_2O$ at 250 °C for >24 h is thus a convenient alternate route to this polymorph.

Single crystals of δ-$Mn_3(PO_4)_2$ from the hydrothermal treatment of $Mn_5(PO_4)_2(PO_3OH)_2{\cdot}4H_2O$ provided high quality X-ray diffraction data. Similar to the other $Mn_3(PO_4)_2$ polymorphs, δ-$Mn_3(PO_4)_2$ crystallizes in the monoclinic $P2_1/c$ space group. Lattice parameters are summarized in Table 1, and atomic coordinates are provided in Table S2. The structure of δ-$Mn_3(PO_4)_2$ is strikingly different from the α, β', and γ polymorphs. These polymorphs each contain two unique [MnO_5] pentahedra and one octahedral [MnO_6] moiety, whereas δ-$Mn_3(PO_4)_2$ lacks Mn in octahedral coordination, instead containing three unique [MnO_5] moieties. Furthermore, δ-$Mn_3(PO_4)_2$ has a channel structure, which contrasts with the more compact atomic arrangements of the α, β', and γ phases. This feature is reflected in the crystal densities, lowest for δ-$Mn_3(PO_4)_2$ (3.5855 g/cm^3) and > 0.1901 g cm^{-3} greater for the other three polymorphs (Table 2.1).[4, 7-8]

Views illustrating the crystal structure of δ-$Mn_3(PO_4)_2$ are shown in Figure 4, with key bond lengths and angles listed in Table 2.2. The structure contains three distinct manganese sites. Both Mn(1) and Mn(3) form [MnO_5] pentahedra, connected by two bridging oxygen atoms, O(7A) and O(1) (Figure 3B). The [MnO_5] pentahedron containing Mn(2) is connected to the corners of two [PO_4] units through O(2) and O(5), and it also shares an edge with an additional [PO_4] group through O(3) and O(4). This connectivity produces the three-dimensional framework shown in Figure 2.3C-E. These views highlight how the two-dimensional planes of the [MnO_5] pentahedra extend in the [100] and [010] directions, joined by [PO_4] tetrahedra corner-shared to all three [MnO_5] pentahedra and also edge-shared with the [Mn(2)O_5] polyhedron. Figure 2.3H shows an isometric view of the (002) plane. The rigid connectivity of the edge-shared [MnO_5] in this plane is responsible for the two-dimensional growth of δ-$Mn_3(PO_4)_2$ nanoplates and microcrystals.

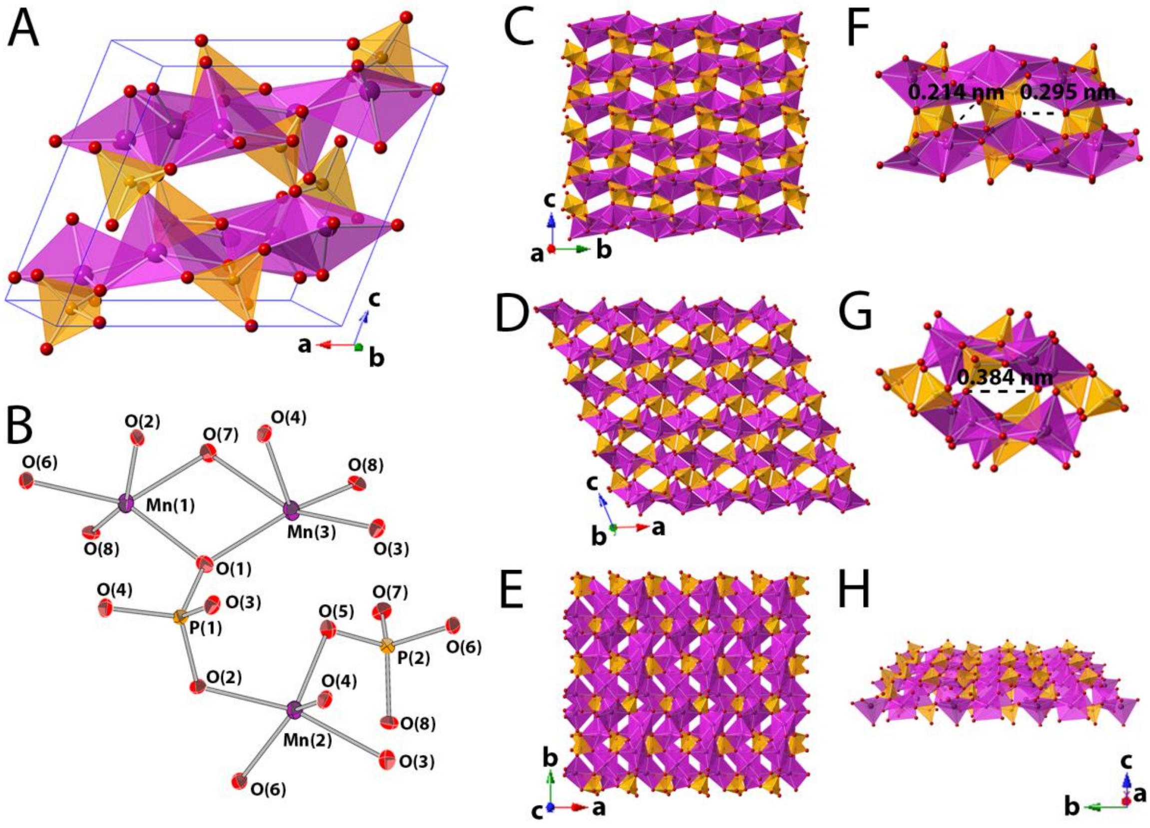

Figure 2.3. Structure of δ-$Mn_3(PO_4)_2$ (O = red, Mn = purple, P = orange): A) Unit cell. B) Thermal ellipsoid plot showing part of the δ-$Mn_3(PO_4)_2$ structure. Thermal ellipsoids are represented at 50% probability. C, D, E) Views of (200), (020), and (002) planes of δ-$Mn_3(PO_4)_2$, respectively. Purple pentahedra = [MnO_5], Orange tetrahedra = [PO_4]. F, G) Channels in the [100] and [010] directions, respectively. H) Isometric view of the (002) plane of δ-$Mn_3(PO_4)_2$.

Channels run in the [100] and [010] directions, as seen in Figure 2.3F-G. The channels extending in the [100] direction have a diameter of 0.21 nm and 0.30 nm, whereas those in the [010] direction have a diameter of 0.38 nm (measured from oxygen to oxygen). BET surface area measurements were attempted on δ-$Mn_3(PO_4)_2$, however the microporous channels of δ-$Mn_3(PO_4)_2$ were too small to allow Ar(g) access.

Selected interatomic distances and bond angles are highlighted in Table 2.2. The Mn-O bond distances vary most widely in [Mn(3)O_5], ranging from 2.0812 to 2.3397 Å, which is consistent with significant distortion. To obey the valence sum rule, the sum of the bond valence of an atom must be equal to the valence of that atom.[23] These differing bond lengths result in the distortion of the polyhedra of the structure. Table S2.3 shows the degree of polyhedral distortion of each atom, according to Baur's distortion index,[24] along with the coordination number, single bond valence and bond valence sum. The bond valence sum values are in good agreement with the formal oxidation state of each atom. Out of the three distinct [MnO_5], the pentahedra containing Mn(1) are the least distorted, while the Mn(3) pentrahedra are the most distorted. The high degree of distortion for the [Mn(3)O_5] pentrahedra is correlated to the larger range of Mn-O bond lengths observed, as it contains Mn-O bond lengths ranging from 2.0817(17) to 2.3397(17) Å. Consequently, the smallest range of Mn-O bond lengths are observed in the [Mn(1)O_5] pentahedra, where the bond lengths are 2.1168(18) to 2.1826(17) Å. The average distance of the Mn-O bonds are comparable to those found in the [MnO_5] polyhedra of the β'-, and γ-$Mn_3(PO_4)_2$ polymorphs, and they are shorter than typical values for [MnO_6];

Table 2.2
Interatomic distances and angles in δ-$Mn_3(PO_4)_2$. Esd's are given in parentheses.

Selected Bond Lengths (Å)	
Avg Mn(1)-O	2.1447
max	2.1826(17)
min	2.1168(18)
Avg Mn(2)-O	2.1465
max	2.2759(18)
min	2.0812(17)
Avg Mn(3)-O	2.1735
max	2.3397(17)
min	2.0817(17)
Avg P(1)-O	1.5373
Avg P(2)-O	1.5406
Selected Bond Angles (°)	
O(8)-Mn(1)-O(6)	90.03(7)
O(8)-Mn(1)-O(1)	112.45(7)
O(1)-Mn(1)-O(2)	90.35(7)
O(6)-Mn(1)-O(2)	76.00(6)
O(1)-Mn(1)-O(7)	79.84(7)
O(2)-Mn(2)-O(6)	78.64(6)
O(6)-Mn(2)-O(3)	104.66(7)
O(3)-Mn(2)-O(4)	66.61(6)
O(2)-Mn(2)-O(4)	88.06(6)
O(5)-Mn(2)-O(4)	112.56(7)
O(1)-Mn(3)-O(3)	119.25 (7)
O(3)-Mn(3)-O(8)	87.51(7)
O(8)-Mn(3)-O(7)	86.69(6)
O(7)-Mn(3)-O(1)	75.67(6)
O(3)-Mn(3)-(O4)	86.90(6)
Avg O-P(1)-O	109.46
Avg O-P(2)-O	109.45

e.g., the average Mn-O bond in olivine $LiMnPO_4$, which contains only octahedral $[MnO_6]$, is 2.20 Å.[25]

The average P-O bond distance in $[PO_4]$ tetrahedra is 1.5373 Å for P(1)-O and 1.5406 Å for P(2)-O. The difference in P-O bond distance is accounted for by the slight distortion of both $[PO_4]$ tetrahedral. Both values fall into the 1.506-1.572 Å range of average P-O bond distances calculated from crystal structure data of PO_4-containing compounds by Baur.[24]

To our knowledge, the structure of δ-$Mn_3(PO_4)_2$ is a new structure type. Related structures include $CaCuAsO_7$,[26] $Na_4Ti_2Si_8O_{22}$,[27] $Ba_2Ti_3Nb_4O_{18}$,[28] $Cu_3In_2(PO_4)_4$,[29] and $Mg_5(CO_3)_4(OH)_2\cdot 4H_2O$,[30] Although these compounds crystallize in the same space group, $P2_1/c$, and contain similar structural motifs as seen in δ-$Mn_3(PO_4)_2$ (e.g., microporous frameworks, two-dimensional planes of MO_x (M = Cu, Ti, Nb, Mg, In) polyhedra interconnected with XO_4 (X = S, Si, As, P) tetrahedra) they are not isomorphous with δ-$Mn_3(PO_4)_2$.

In earlier work, Clemens and coworkers explored Li/Mn substitution in $Li_xMn_{1.5-x/2}PO_4$ $(0 \leq x \leq 1)$[9, 31] and found one unusual case: upon reacting $LiMnPO_4$ and β'-$Mn_3(PO_4)_2$ such that x = 0.2, they detected a new phase rather than the expected $Li_{0.2}Mn_{1.4}PO_4$. Although they successfully determined the space group and lattice parameters of this ‘unbekannt’ product from powder XRD data, its structure and identity remained unknown.[31] The XRD pattern reported by Clemens, in fact, matches to that of δ-$Mn_3(PO_4)_2$. We replicated the solid state synthesis using a sealed quartz ampule containing a 1:2 ratio of β'-$Mn_3(PO_4)_2$ to $LiMnPO_4$ heated at 1,000 °C for 15 h. The XRD pattern of the product revealed a mixture of δ-$Mn_3(PO_4)_2$ and β'-$Mn_3(PO_4)_2$ (Figure 2.4).

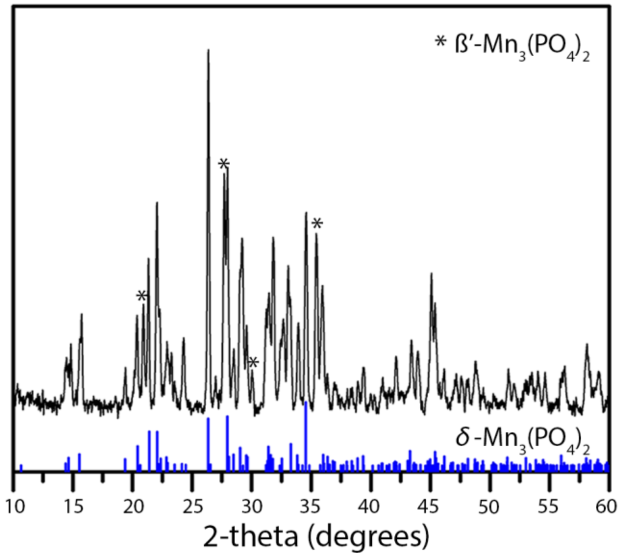

Figure 2.4. XRD pattern (Cu X-ray source) of the product from the solid state reaction of β'-$Mn_3(PO_4)_2$ and $LiMnPO_4$ at 1,000 °C, with assignments to δ-$Mn_3(PO_4)_2$ (blue lines) and β'-$Mn_3(PO_4)_2$ (*).

It is interesting that the solid-state reaction temperature of 1,000 °C is beyond the $\delta \rightarrow \beta'$ phase transition temperature of 735 °C, as described in the next section. This observation leads us to propose the following ideas: (1) the reaction of β'-$Mn_3(PO_4)_2$ and $LiMnPO_4$ may actually proceed to full conversion, but some of the δ-$Mn_3(PO_4)_2$ reverts back to β'-$Mn_3(PO_4)_2$ at this temperature, and (2) the role of the $LiMnPO_4$ may be to stabilize δ-$Mn_3(PO_4)_2$, perhaps through Li^+ incorporation. These aspects of $Mn_3(PO_4)_2$ chemistry require further investigation.

DSC measurements and *in situ* variable temperature XRD studies show that δ-$Mn_3(PO_4)_2$ is stable up to 735 °C, and beyond this temperature, it converts into β'-$Mn_3(PO_4)_2$. This transition is evident from the DSC data, which shows an exothermic event with an onset temperature of 735.3 °C (Figure 2.5A). The heat of transition is –2.76 kJ/mol (–7.78 J/g). For comparison, the anatase to rutile transition has a $\Delta H°$ of –3.26 kJ/mol at 697.9 °C.[32] No peaks were observed on a second equivalent heating, confirming the irreversibility of the $\delta \rightarrow \beta'$ phase transition.

Thermogravimetric analysis performed from 25–900 °C showed a small 0.6% mass loss, which can be attributed to adsorbed O_2 and H_2O (Figure S2.5A).

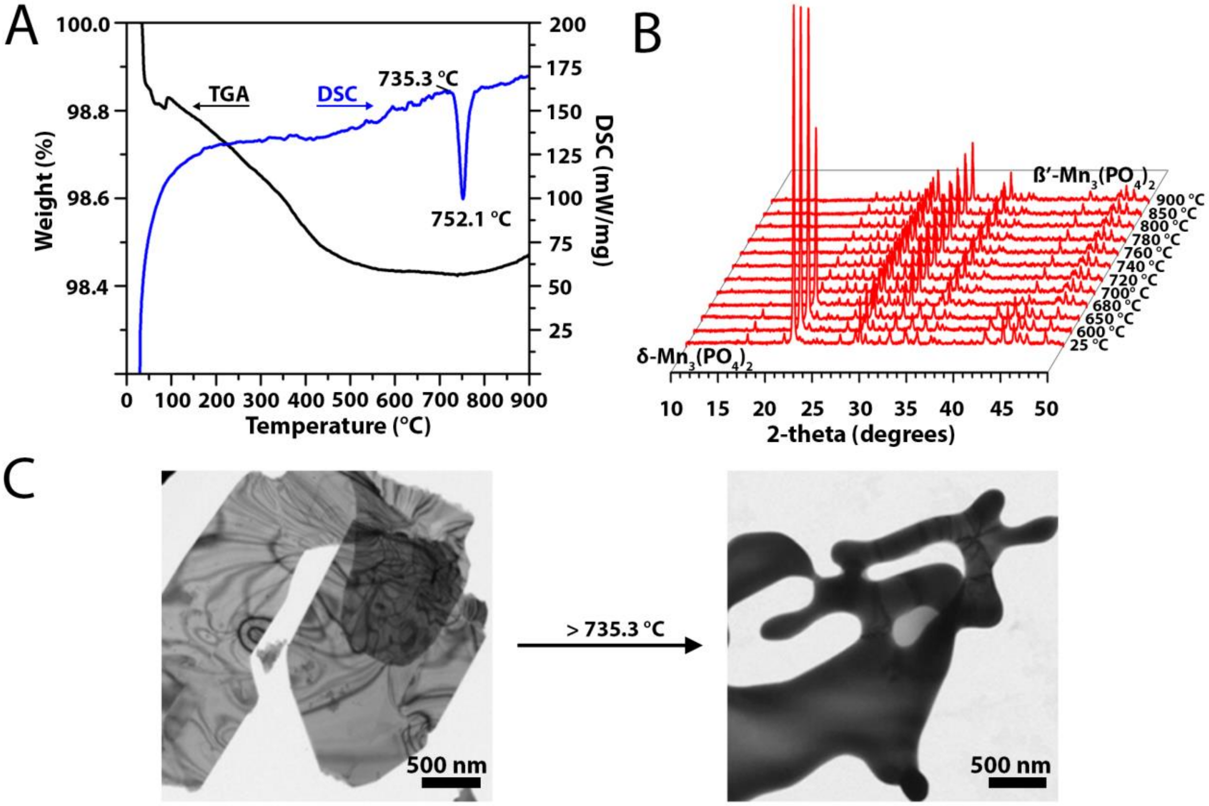

Figure 2.5. A) DSC and TGA of δ-$Mn_3(PO_4)_2$ nanoplates. B) *In situ* XRD temperature study of δ-$Mn_3(PO_4)_2$ nanoplates. C) TEM of δ-$Mn_3(PO_4)_2$ nanoplates before and after *ex situ* heating above the $\delta \rightarrow \beta'$ transition temperature of 735.3 °C.

Variable temperature XRD measurements also reveal the structural changes of the $\delta \rightarrow \beta'$ $Mn_3(PO_4)_2$ transition. Figure 2.5B shows the diffraction patterns of δ-$Mn_3(PO_4)_2$ at temperatures ranging from 25 to 900 °C. No discernible changes in the XRD pattern occur from RT up to 650 °C. However, a decrease in peak intensity of the (002) peak is observed at 680 °C along with the emergence of peaks belonging to β'-$Mn_3(PO_4)_2$. At 700 °C, the (002) peak of δ-$Mn_3(PO_4)_2$ completely disappears and the remaining pattern matches to phase pure β'-$Mn_3(PO_4)_2$.

The $\delta \rightarrow \beta'$ $Mn_3(PO_4)_2$ phase transition was also observed by TEM. Whereas the δ-$Mn_3(PO_4)_2$ morphology consists of distinct nanoplates, heating above the transition temperature leads to rounded, irregular morphologies (Figure 2.5C) that correspond to β'-$Mn_3(PO_4)_2$. This change reflects the difference between the layered structure of δ-$Mn_3(PO_4)_2$ and the three-dimensional structure of β'-$Mn_3(PO_4)_2$.

The Raman and infrared spectra of δ-$Mn_3(PO_4)_2$ are dominated by PO_4^{3-} resonances. As seen in the Raman spectrum in Figure 6, δ-$Mn_3(PO_4)_2$ nanoplates shows distinct peaks at 1044, 1014, 991, 977, 968, and 946 cm^{-1} with small bands at 610, 584, and 555 cm^{-1}. The dominant peaks in the IR spectrum are found at 1108, 1072, 1047, 1010, 989, and cm^{-1}, also with peaks at 613, 592, 557, and 547 cm^{-1}. Analogous peaks are found in the Raman and IR spectra of the δ-microcrystals (Figure S6). These peaks correspond to the internal stretches of the PO_4^{3-} ions.[33],[34] Similar peak values are found in the IR spectra of other inorganic phosphates, such as $Mn_3(PO_4)_2 \cdot 7H_2O$.[35] Finally, the lack of peaks around 3500 cm^{-1} indicates the absence of water or OH^- groups from adsorbed or interlayer hydrates.

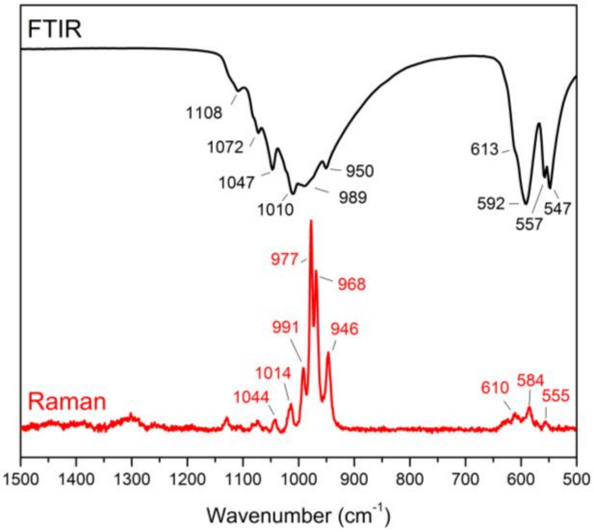

Figure 2.6. Raman and FTIR spectra of δ-$Mn_3(PO_4)_2$nanoplates.

XPS data (Figure S2.8) shows two peaks for the Mn 3s region, one at 92.7 eV and the other at 86.2 eV. The difference of 6.5 eV between these peaks are indicative of Mn in the 2+ oxidation state.[36] The Mn $2p^{1/2}$ and $2\ p^{3/2}$ peaks of 657.2 and 645.3 are shifted to about 2 eV higher than those observed for $Mn_3(PO_4)_2{\cdot}3H_2O$,[1] due to charging effects. Other values, including 136.3 eV for the P $2p^{3/2}$ region and 534.3 eV for the O 1S region are also slightly higher than the values found in the literature for similar metal (II) phosphate compounds.[37],[38] These also may be attributed to surface charging. In fact, charging was noticeable during SEM imaging, a consequence of the poorly conducting phosphate groups.

Conclusions

Is the existence of a fourth polymorph of $Mn_3(PO_4)_2$ surprising? Perhaps not, based on what is already known about the polymorphism of metal(II) phosphates. As pointed out by Vasiliev and coworkers regarding manganese(II) phosphates, the flexibility of Mn^{2+} with respect ultimately leads to rich structural diversity.[8] Nevertheless, it *is* surprising that δ-$Mn_3(PO_4)_2$ was not isolated and characterized earlier, especially in light of our results demonstrating its accessibility via hydrothermal and solid state routes and its thermal stability. An additional discovery is the new low-density, microporous structure of δ-$Mn_3(PO_4)_2$ that makes it a candidate for emerging electrode applications.

References

[1] K. Jin, J. Park, J. Lee, K. D. Yang, G. K. Pradhan, U. Sim, D. J. Jeong, H. L., S. Park, D. Kim, N. E. Sung, S. H. Kim, S. Han and K. T. Nam, *J Am Chem Soc* **2014**, *136*, 7435-7443.

[2] C. Yang, L. Dong, Z. Chen and H. Lu, *The Journal of Physical Chemistry C* **2014**, *118*, 18884-18891.

[3] H.-J. Zhu, W. Zhai, M. Yang, X.-m. Liu, Y.-C. Chen, H. Yang and X.-d. Shen, *RSC Advances* **2014**, *4*, 25625.

[4] J. S. Stephens and C. Calvo, *Canadian Journal of Chemistry* **1969**, *47*, 2215-2225.

[5] B. El-Bali, A. Boukhari, R. Glaum, M. Gerk and K. Maaß, *Zeitschrift für anorganische und allgemeine Chemie* **2000**, *626*, 2557-2562.

[6] A. NORD and H. ANNERSTEN, *Acta chemica Scandinavica. Series A. Physical and inorganic chemistry* **1987**, *41*, 56-58.

[7] W. Massa, O. V. Yakubovich and O. V. Dimitrova, *Solid State Sciences* **2005**, *7*, 950-956.

[8] O. S. Volkova, L. V. Shvanskaya, E. A. Ovchenkov, E. A. Zvereva, A. S. Volkov, D. A. Chareev, K. Molla, B. Rahaman, T. Saha-Dasgupta and A. N. Vasiliev, *Inorganic Chemistry* **2016**, *55*, 10692-10700.

[9] O. Clemens, R. Haberkorn, M. Springborg and H. P. Beck, *Zeitschrift für anorganische und allgemeine Chemie* **2014**, *640*, 173-183.

[10] J.-C. Toledano, A. M. Glazer, T. Hahn, E. Parthe, R. S. Roth, R. S. Berry, R. Metselaar and S. C. Abrahams, *Acta Crystallographica Section A* **1998**, *54*, 1028-1033.

[11] D. M. C. Huminicki and F. C. Hawthorne, *Reviews in Mineralogy and Geochemistry* **2002**, *48*, 123-253.

[12] S. Bevara, S. N. Achary, P. D. Babu and A. K. Tyagi, *AIP Conference Proceedings* **2015**, *1665*, 030021.

[13] S.-L. Yang, R.-G. Ma, M.-J. Hu, L.-J. Xi, Z.-G. Lu and C. Y. Chung, *Journal of Materials Chemistry* **2012**, *22*, 25402.

[14] C. Wu, J. Xie, G. Cao, X. Zhao and S. Zhang, *CrystEngComm* **2014**, *16*, 2239.

[15] X. Rui, X. Zhao, Z. Lu, H. Tan, D. Sim, H. H. Hng, R. Yazami, T. M. Lim and Q. Yan, *ACS Nano* **2013**, *7*, 5637-5646.

[16] S. Menchetti and C. Sabelli, *Acta Crystallographica Section B* **1973**, *29*, 2541-2548.

[17] C. Delacourt, P. Poizot, M. Morcrette, J. M. Tarascon and C. Masquelier, *Chemistry of Materials* **2004**, *16*, 93-99.

[18] F. W. Boyle and W. L. Lindsay, *Soil Science Society of America Journal* **1985**, *49*, 761-766.

[19] S. G. Thoma, F. Bonhomme and R. T. Cygan, *Chemistry of Materials* **2004**, *16*, 2068-2075.

[20] V. Aravindan, J. Gnanaraj, Y.-S. Lee and S. Madhavi, *Journal of Materials Chemistry A* **2013**, *1*, 3518.

[21] P. Nie, L. Shen, F. Zhang, L. Chen, H. Deng and X. Zhang, *CrystEngComm* **2012**, *14*, 4284.

[22] L. Bao, G. Xu, J. Wang, H. Zong, L. Li, R. Zhao, S. Zhou, G. Shen and G. Han, *CrystEngComm* **2015**, *17*, 6399-6405.

[23] I. Brown, *Acta Crystallographica Section B* **1977**, *33*, 1305-1310.

[24] W. Baur, *Acta Crystallographica Section B* **1974**, *30*, 1195-1215.

[25] S. Geller and J. L. Durand, *Acta Crystallographica* **1960**, *13*, 325-331.

[26] T.-C. Chen and S.-L. Wang, *Journal of Solid State Chemistry* **1996**, *121*, 350-355.

[27] Z. Lin, J. Rocha, P. Brandão, A. Ferreira, A. P. Esculcas, J. D. Pedrosa de Jesus, A. Philippou and M. W. Anderson, *The Journal of Physical Chemistry B* **1997**, *101*, 7114-7120.

[28] M. Gasperin, *Acta Crystallographica Section C* **1984**, *40*, 9-11.

[29] M. Gruß and R. Glaum, *Zeitschrift für anorganische und allgemeine Chemie* **2001**, *627*, 1377-1382.

[30] M. Akao and S. Iwai, *Acta Crystallographica Section B* **1977**, *33*, 1273-1275.

[31] O. Clemens, *(Saarbrücken, http://scidok.sulb.uni-saarland.de/volltexte/2012/4718/)* **2011**.

[32] T. Mitsuhashi and O. J. Kleppa, *Journal of the American Ceramic Society* **1979**, *62*, 356-357.

[33] P. N. de Aza, C. Santos, A. Pazo, S. de Aza, R. Cuscó and L. Artús, *Chemistry of Materials* **1997**, *9*, 912-915.

[34] R. L. Frost, Y. Xi, R. Scholz, A. López and F. M. Belotti, *Vibrational Spectroscopy* **2013**, *66*, 69-75.

[35] F. A. Miller and C. H. Wilkins, *Analytical Chemistry* **1952**, *24*, 1253-1294.

[36] M. C. Biesinger, B. P. Payne, A. P. Grosvenor, L. W. M. Lau, A. R. Gerson and R. S. C. Smart, *Applied Surface Science* **2011**, *257*, 2717-2730.

[37] Y. Wang, *Surface Science Spectra* **2002**, *9*, 91.

[38] J. Ma, B. Li, H. Du, C. Xu and F. Kang, *Journal of Solid State Electrochemistry* **2011**, *16*, 1353-1362.

[39] G. M. Sheldrick, *Bruker Analytical X-ray Instruments: Madison, WI* **2013**.

[40] D. T. W. J. T. Cromer, *Kynoch Press, Birmingham England* **1974**, *IV*.

Supporting Information

Of the 2004 unique reflections collected, 1754 were observed ($I > 2\ \sigma(I)$). The linear absorption coefficient for Mo Kα radiation is 6.172 mm^{-1}. The data were corrected for Lorentz and polarization effects and integrated with the manufacturer's SAINT software. Absorption corrections were applied with the SADABS.

Subsequent solution and refinement was performed using the SHELXTL-2013[39] solution package operating on a Pentium computer. The structure was solved by direct method using SHELXTL-2013 Software Package. Non-hydrogen atomic scattering factors were taken from the literature tables.[40] Non-hydrogen atoms were located from successive difference Fourier map calculations. In the final cycles of each refinement, all the non-hydrogen atoms were refined in anisotropic displacement parameters. The crystal system of compound is monoclinic, space group $P2_1/c$ (No. 14) and the final residual values based on 118 variable parameters and 1754 observed reflections ($I > 2\ \sigma(I)$) are $R1 = 0.0291$, $wR2 = 0.0723$, and those for all unique reflections are $R1 = 0.0339$, $wR2 = 0.0746$. The goodness-of-fit indicator for all data is 1.024. Peaks on the final difference map ranging from 1.140 to -0.626e/Å^3, are of no chemical significance. The efforts have been made to resolve as many alerts as possible generated by CheckCIF. The current highest alerts are at level G, which are false alarms.

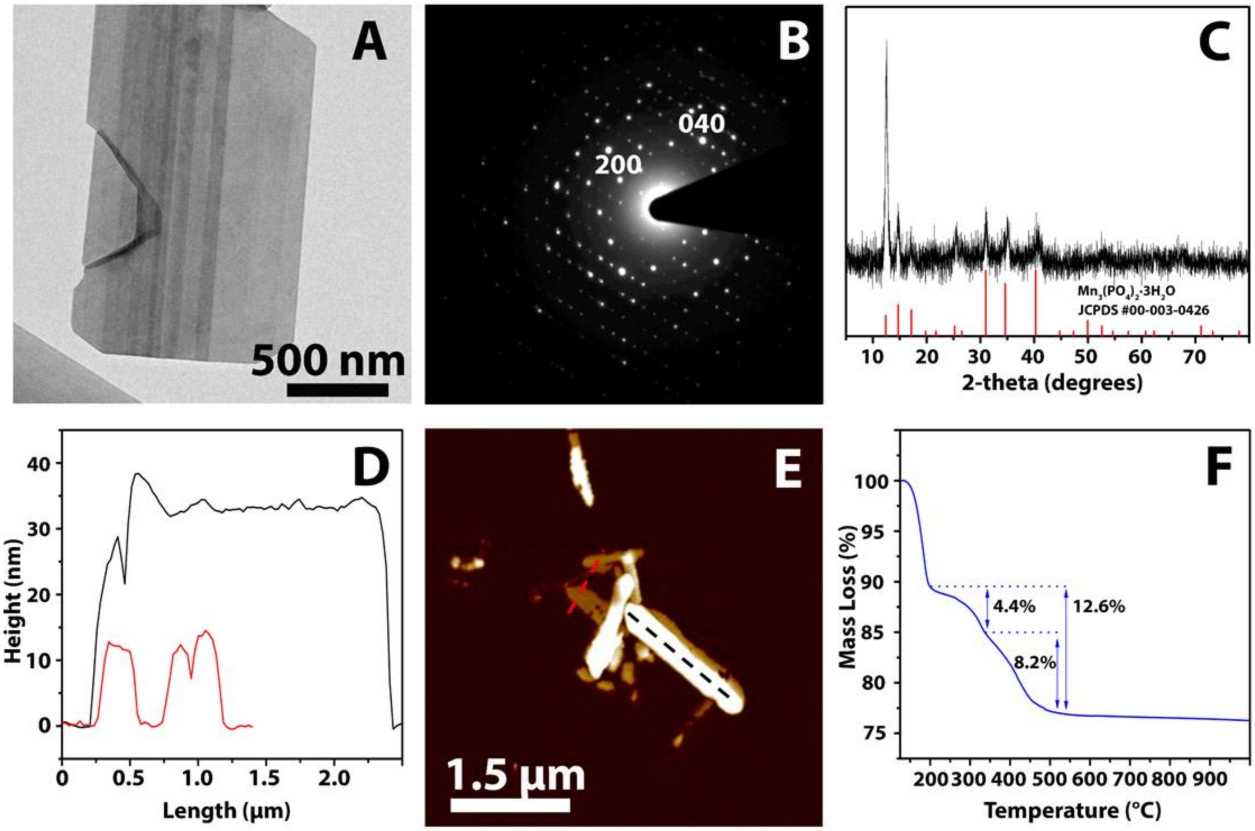

Figure S2.1: Characterization of $Mn_3(PO_4)_2 \cdot 3H_2O$: A) TEM image and B) SAED pattern of $Mn_3(PO_4)_2 \cdot 3H_2O$. C) Experimental (black curve) and reference (red lines) XRD patterns for $Mn_3(PO_4)_2 \cdot 3H_2O$, JCPDS #00-003-0426. D) AFM height profile and E) AFM image of $Mn_3(PO_4) \cdot 3H_2O$. F) TGA curve for $Mn_3(PO_4)_2 \cdot 3H_2O$.

Table S2.1
ICP-OES data for δ-$Mn_3(PO_4)_2$

Mn	P	weight ratio (Mn:P)	atomic ratio (Mn:P)
0.584 ppm	0.208 ppm	2.8:1	3.16:2

Time study of the hydrothermal reaction of $Mn_3(PO_4)_2{\cdot}3H_2O$ nanosheets at 120 °C S4

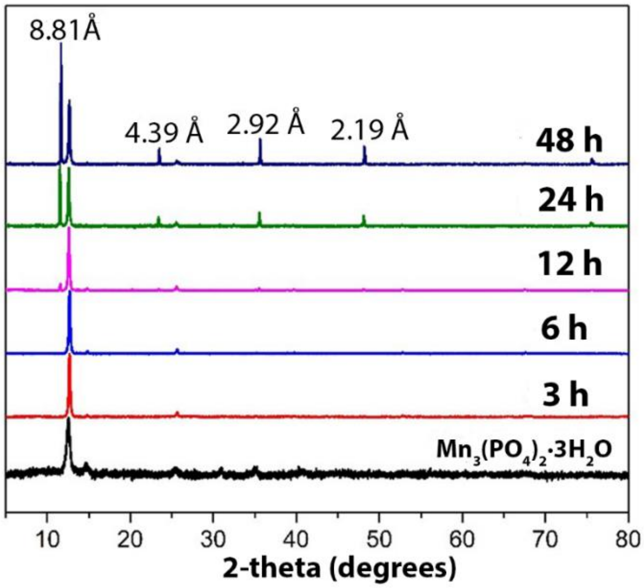

Figure S2.2: Time study monitored by XRD (Co X-ray source) of the hydrothermal reaction of $Mn_3(PO_4)_2{\cdot}3H_2O$ nanosheets at 120 °C. Over the course of 48 h, peaks belonging to the (*h*00) series of $Mn_5(PO_4)_2(PO_3OH)_2{\cdot}4H_2O$ appear, suggesting that this compound is an intermediate in the formation of δ-$Mn_3(PO_4)_2$ nanoplatelets.

$Mn_5(PO_4)_2(PO_3OH)_2 \cdot 4H_2O$ and δ-$Mn_3(PO_4)_2$ microcrystal characterization:

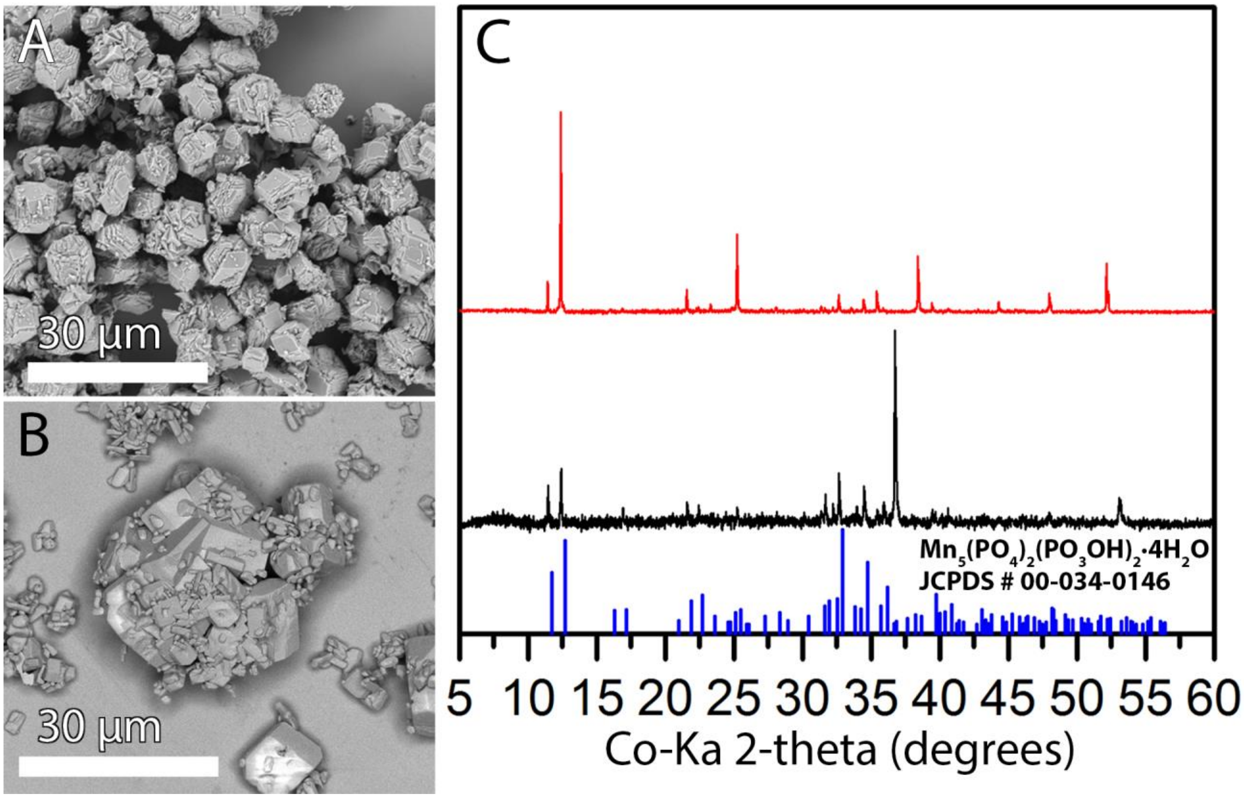

Figure S2.3: A) SEM image of $Mn_5(PO_4)_2(PO_3OH)_2 \cdot 4H_2O$ prepared by the alternate synthesis reported here. B) SEM image of $Mn_5(PO_4)_2(PO_3OH)_2 \cdot 4H_2O$ by the literature procedure of Bevara et al.[12] C) XRD (Co X-ray source) of our synthesis (black) and the Bevara synthesis (red). Blue Drop lines correspond to $Mn_5(PO_4)_2(PO_3OH)_2 \cdot 4H_2O$, JCPDS # 00-034-0146.

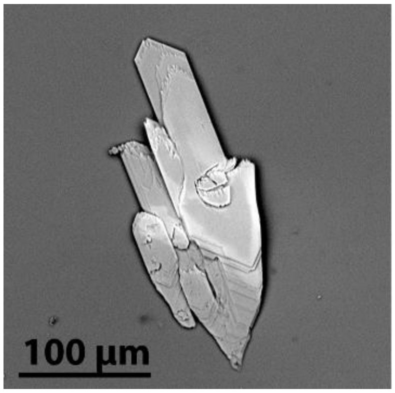

Figure S2.4: SEM image of single crystalline δ-$Mn_3(PO_4)_2$

Atomic Coordinates of *δ*-$Mn_3(PO_4)_2$:

Table S2.2

Bond Valence values for δ-$Mn_3(PO_4)_2$

	CN	Single Bond Valence	VB Sums	Polyhedra Distortion
Mn(1)	5	0.4	1.922(4)	0.000170
Mn(2)	5	0.4	1.939(4)	0.001042
Mn(3)	5	0.4	1.825(4)	0.001816
P(1)	4	1.25	4.963(12)	0.000004
O(1)	3	0.667	2.110(6)	0.019275
O(2)	3	0.667	2.055(7)	0.021778
O(3)	3	0.667	2.018(7)	0.020831
O(4)	3	0.667	1.839(6)	0.027558
P(2)	4	1.25	4.920(12)	0.000043
O(5)	2	1	1.677(6)	0.025004
O(6)	3	0.667	2.041(7)	0.019751
O(7)	3	0.667	1.901(6)	0.029375
O(8)	3	0.667	1.930(7)	0.020944

Table S2.3:
Atomic Coordinates
for δ-$Mn_3(PO_4)_2$

Atom	x	y	z	U (eq)
Mn (1)	8384(1)	1478(1)	6313(1)	14(1)
Mn (2)	6729(1)	6278(1)	2460(1)	14(1)
Mn (3)	7474(1)	4878(1)	7067(1)	15(1)
P (1)	5961(1)	3104(1)	3384(1)	11(1)
P (2)	9054(1)	8083(1)	5360(1)	11(1)
O (1)	7181(2)	3404(2)	5146(2)	16(1)
O (2)	6413((2)	4029(2)	2145(2)	14(1)
O (3)	4233(2)	3440(2)	3280(2)	15(1)
O (4)	5949(2)	1460(2)	3019(2)	15(1)
O (5)	8188(2)	6604(2)	4980(2)	16(1)
O (6)	8069(2)	9180(2)	5958(2)	15(1)
O (7)	10759(2)	7965(2)	6671(2)	16(1)
O (8)	9211(2)	8702(2)	3754(2)	15(1)

Bond Valence Values for *δ*-$Mn_3(PO_4)_2$:

Table S2.4

Bond Valence Parameters for δ-$Mn_3(PO_4)_2$

	CN	Single Bond Valence	BVS	Polyhedra Distortion
Mn(1)	5	0.4	1.922(4)	0.000170
Mn(2)	5	0.4	1.939(4)	0.001042
Mn(3)	5	0.4	1.825(4)	0.001816
P(1)	4	1.25	4.963(12)	0.000004
O(1)	3	0.667	2.110(6)	0.019275
O(2)	3	0.667	2.055(7)	0.021778
O(3)	3	0.667	2.018(7)	0.020831
O(4)	3	0.667	1.839(6)	0.027558
P(2)	4	1.25	4.920(12)	0.000043
O(5)	2	1	1.677(6)	0.025004
O(6)	3	0.667	2.041(7)	0.019751
O(7)	3	0.667	1.901(6)	0.029375
O(8)	3	0.667	1.930(7)	0.020944

Secondary Characterization Data:

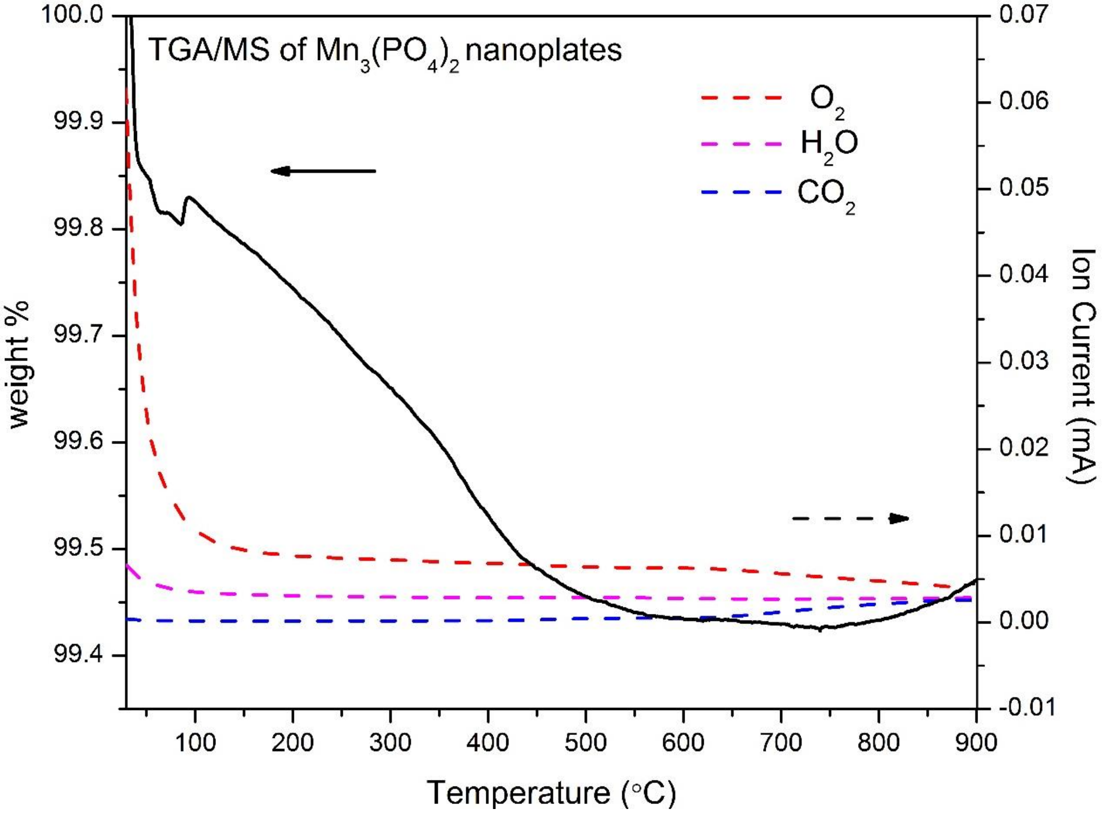

Figure S2.5; TGA/MS data from δ-$Mn_3(PO_4)_2$ nanoplates.

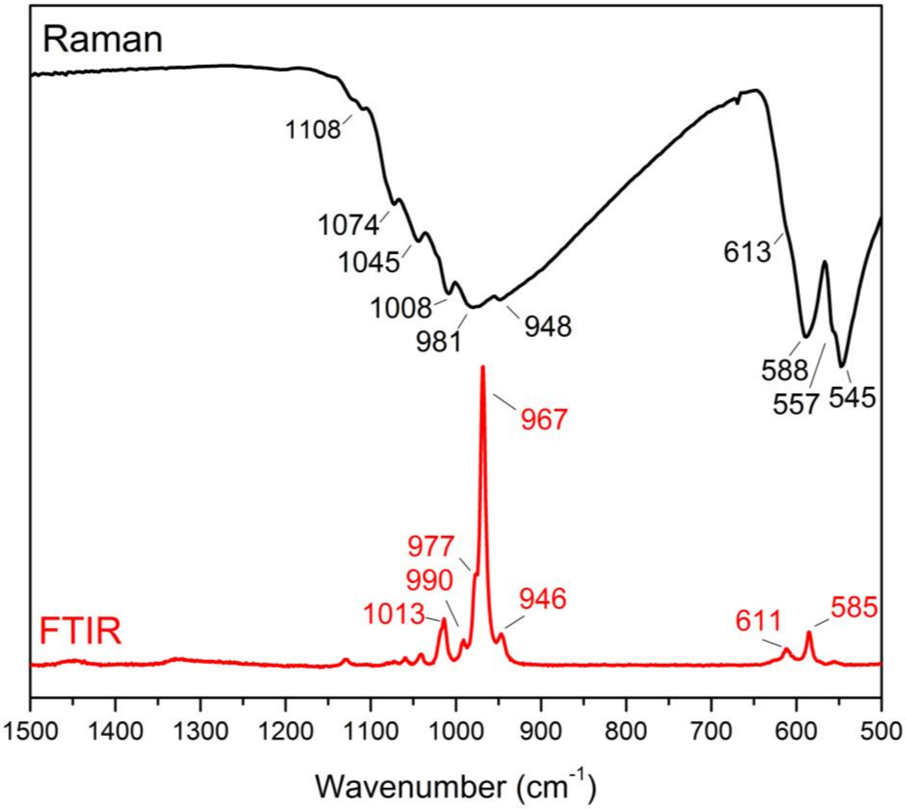

Figure S2.6: Raman and FTIR spectra of δ-$Mn_3(PO_4)_2$ microcrystals.

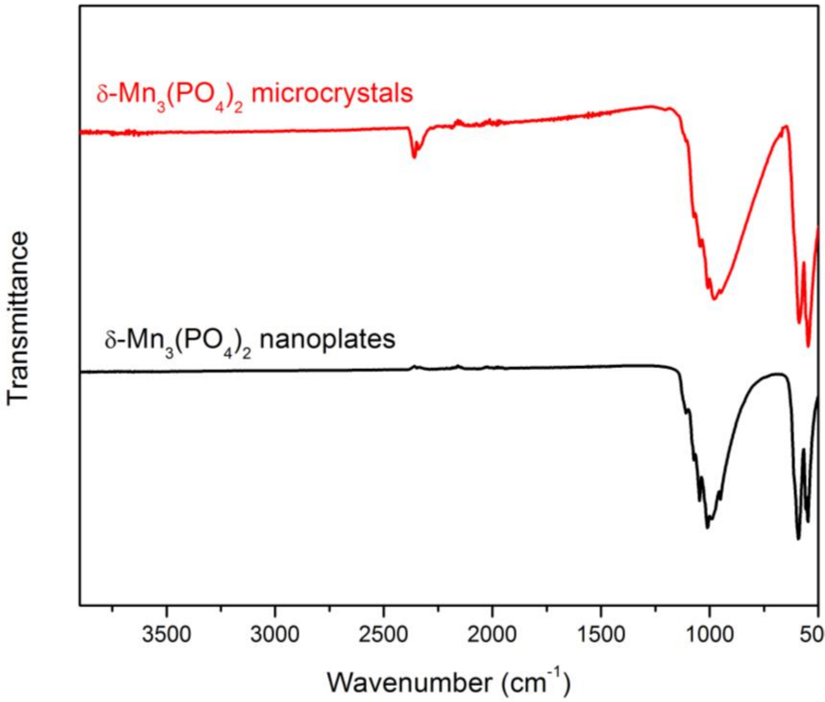

Figure S2.7: Raman and FTIR spectra of δ-$Mn_3(PO_4)_2$ microcrystals and nanoplates.

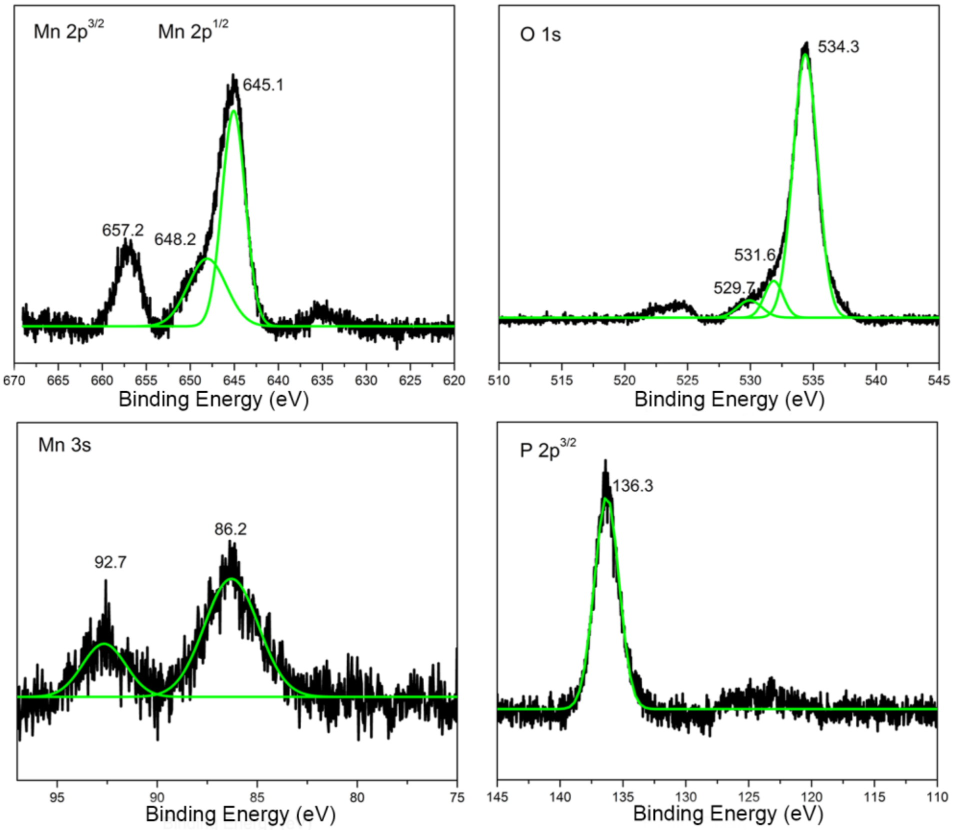

Figure S2.8: XPS data for *δ*-$Mn_3(PO_4)_2$ microplatelets.

CHAPTER 3

$LiMnPO_4$ NANOSHEETS FROM $Mn_3(PO_4)_2 \cdot 3H_2O$ FOR LITHIUM-ION BATTERIES

Neher, G. and Salguero, T.T. To be submitted to *Chemistry of Materials*.

Abstract

Many hydrothermal and solvothermal syntheses that lead to nanostructured $LiMnPO_4$ typically use a Mn(II) salt, a dibasic phosphate salt, and a lithium precursor in aqueous or organic solvents. In these conditions, $Mn_3(PO_4)_2 \cdot 3H_2O$ nanosheets are formed *in situ*, and react with Li ions hydrothermally at temperatures ≥120 °C to form $LiMnPO_4$ in various nanomorphologies. Here, we study the solvothermal reaction of $Mn_3(PO_4)_2 \cdot 3H_2O$ nanosheet dispersions with Li salts and analyze their impact on the final morphology of $LiMnPO_4$. Reaction with LiH_2PO_4 solvothermally at 250 °C in a ratio of 25:5 DEG:H_2O resulted in $LiMnPO_4$ nanosheets that are microns in lateral dimensions and <6 nm in thickness. Temperature and H_2O:DEG ratio were found to be important parameters in this reaction, as varying these conditions lead to the observation of manganese phosphate impurities. Furthermore, three-dimensional nanomorphologies of $LiMnPO_4$ were obtained by using Li_3PO_4 as the precursor. These findings suggest that two-dimensional nanosheets form under stringent reaction conditions. The electrochemical performance of carbon-coated $LiMnPO_4$ nanosheets exhibit excellent cycling stability. Future work aims to optimize the carbon-coating to achieve discharge capacities closer to the theoretical of 171 mAh/g.

Introduction

Battery researchers have been interested in $LiMPO_4$ (M = Mn, Fe, Co, Ni) as cathode materials since they were first implemented in Li-ion batteries electrodes by Padhi et al in 1997.[1] The high operating voltage of the M^{2+}/M^{3+} redox couple (3.4 V-5.1 V) vs Li^+/Li as well as their relatively large theoretical capacity (170-173 mAh/g) make them enticing materials for Li-ion batteries with high energy density. Furthermore, the strong covalent nature of the P-O of the phosphate tetrahedra makes these class of compounds less susceptible to thermal runaway at elevated temperatures than $LiCoO_2$ and $LiMn_2O_4$.[2]

However, these olivine compounds suffer from two major drawbacks. First, their intrinsic electronic conductivity is extremely low. For example, the conductivity of $LiFePO_4$ is 10^{-9}-10^{-10} cm^{-1} and that of $LiMnPO_4$ is $<10^{-10}$ S cm^{-1}.[3] This issue is counteracted by different carbon coating methods such as annealing in sucrose,[4] spray pyrolysis,[5] or by mixing with graphene.[6] Second, the diffusion of Li ions is particularly sluggish—computational calculations show that Li ions migrate out of the lattice along a one dimensional, nonlinear pathway in the [010] direction.[7],[8] This can be especially problematic as these channels are easily blocked by defect sites. Indeed, there have been many reports of antisite defects leading to lower electrochemical activity. These antisite defects occur when the metal ion in the M2 site interchanges with the Li ion on the M1 site. Quantitative evidence for these defect sites comes from high-angle annular dark field scanning-tunneling microscopy (HAADF-STEM), a technique that provides high z contrast[9],[10] and neutron diffraction.[11]

One major strategy to improve the lithium diffusion into and out of the $LiMPO_4$ lattice is to synthesize these materials with dimensions on the nanoscale, and thereby diminishing the distance that Li ions have to travel. To date, $LiMnPO_4$ has been synthesized in a variety of nanomorphologies, including nanoparticles,[12] flower-like structures,[13],[14] and nanoplatelets[15],[16]. These morphologies have all shown improved electrochemical activity compared to bulk $LiMnPO_4$. Nanosheets of $LiMnPO_4$ that exhibit the (020) plane and contain lateral dimensions in microns and thicknesses <10 nm, represent an excellent morphology to decrease the Li ion diffusion pathway to the smallest size possible, while still maintaining a large active surface area. However, to date, there are only a handful of articles that demonstrate the successful synthesis of <10 nm thick $LiMnPO_4$ nanosheets. Yan and coworkers were able to synthesize nanosheets of $LiMnPO_4$ with the (020) plane and other phospo-olivine compounds <5nm in thickness, however, their synthesis involved a high-pressure high-temperature reactor that required 10 MPa and 400 °C.[17] Recently however, Wang and coworkers designed <12 thick nanosheets of $LiFePO_4$ with the (200) plane that exhibited excellent electrochemical performance.[18] This result was unexpected and attributed to the decreased barrier height of the active populations due to the <15 nm thickness of the nanosheets. These results suggest that developing nanosheets with the (020) face is not the only way to develop a high performance cathode.

Many of the bottom-up growth methods that form $LiMnPO_4$ in various nanomorphologies use a soluble Mn salt, a lithium phosphate compound, and a capping agent, such as glycols or long chained amines. These morphologies are typically controlled by changing the amount of precursors, solvent ratio, or reaction temperatures. In this report, we describe the use of $Mn_3(PO_4)_2{\cdot}3H_2O$ nanosheets as a precursor for the synthesis of $LiMnPO_4$ nanosheets. The motivation for using $Mn_3(PO_4)_2{\cdot}3H_2O$ nanosheets as a precursor stems from their formation as an intermediate in many reports involving the synthesis of $LiMnPO_4$ nanomaterials.[19],[20]

Experimental

Materials**:** The following reagents were used as received: $MnSO_4{\cdot}H_2O$ (J.T. Baker 99%), $(NH_4)_2HPO_4$ (Sigma-Aldrich, ≥98%), Diethylene Glycol (Sigma Aldrich, 99%), Ethylene Glycol (Sigma Aldrich ≥ 99%), $MnCl_2{\cdot}6H_2O$ (Sigma Aldrich, 99-102%) $Mn(CH_3COO)_2{\cdot}4H_2O$ (Aldrich ≥ 99%) , LiH_2PO_4 (Aldrich, 99%), LiCl (Sigma Aldrich, ≥ 99%)

Preparation of $Mn_3(PO_4)_2{\cdot}3H_2O$

2.7109 mmol (0.35800 g) of $(NH_4)_2HPO_4$ and 4.0801 mmol (1.0000 g) of $Mn(CH_3OO)_2{\cdot}4H_2O$ were each dissolved in 15 mL nanopure water. The solutions were mixed, and a milky white precipitate formed. The suspension was stirred for 30 min at room temperature. The colloidal suspensions was centrifuged at 10,000 rpm, and the precipitate was washed with 30 mL nanopure water 3 times. The nanosheets could either be kept in solution or dried under vacuum.

Preparation of $LiMnPO_4$ Nanosheets

5 ml of a 0.010 mg/mL dispersion of $Mn_3(PO_4)_2{\cdot}3H_2O$ nanosheets (0.050 total grams, or 0.122 mmol), were added to 25 mL of DEG and stirred for 15 min. Next, 0.369 mL of 1 M LiH_2PO_4 (0.369 mmol) was added to the dispersion and stirred for another 30 min. The suspension was added to 42 mL Teflon-line autoclave and reacted at 250 °C for 6 h. Afterwards, the suspension was washed centrifuged at 10,000 rpm and washed with 30 mL EtOH 3x and 30 mL nanopure water 3x. The resulting cream white powder was dried at 120 °C for 12 h, and could be easily redispersed in H_2O by bath sonication for a 0.031525 g yield (82.3%).

Carbon Coating $LiMnPO_4$ Nanosheets

0.300 g $LiMnPO_4$ nanosheets were ground with 0.0785 g of sucrose to give a theoretical loading of 10% carbon. 3 mL of H_2O was added to the $LiMnPO_4$ and sucrose mixture and then sonicated for 1h. The suspension was dried by heating in an oven at 120 °C for 12 h. The resulting powder was lightly ground with a mortar and pestle, and transferred to a quartz ampoule. The ampoule was then evacuated and backfilled 3x with Ar, and then left under vacuum and sealed. Next, the ampoule was added to a Lindberg Blue furnace and heated from 25 °C to heated to 600 °C at 5 °C/min, and held at this temperature for 5 hr. The resulting product was a black powder.

Electrochemical Testing

To test the electrochemical properties of $LiMnPO_4/C$ nanosheets, CR2032 coin cells were assembled with $LiMnPO_4/C$ as the cathode material. For the slurry formulation, 0.300 g of $LiMnPO_4/C$ nanosheets and 22.5 mg Super C were added to a solution of 22.5 mg of PVDF binder dissolved in 0.853 mL NMP, and ball milled at 300 RPM for 30 minutes in a Fritsch Planetary Miller. The total ratio of active material to carbon to PVDF was 80:10:10. The slurry was deposited on aluminum foil and spread evenly using a glass stir rod. It was then dried at 120 °C overnight under vacuum to remove NMP and trace H_2O. Coin cells were assembled in an Ar glovebox. The $LiMnPO_4/C$ electrode, polypropylene separator (Celgard), Li metal, and two springs and two spacers were arranged between a CR2032 cap and case, with 1 M $LiPF_6$ in 50:50 DEC:EC as the electrolyte. The coin cells were then taken out of the glovebox and crimped at ~1,000 PSI. Electrochemical testing was performed on an Arbin MITS pro. Galvanostatic charge-discharge curves were carried out from 2.5-4.5 V at different C rates. Cyclic Voltammetry (CV) curves were obtained by scanning at a rate of 0.1 mV/s.

Characterization

Powder X-ray Diffraction (PXRD) data were collected on a PANalytical X'Pert utilizing a Cu Kα X-ray source (λ = 1.54184) operated at 45 kV and 40 mA.

Diffraction data was collected from 5-70 2θ with a scan rate of 0.3 s/step. Samples were prepared as powder mounts or drop cast from solution.

Transmission Electron Microscopy (TEM) imaging and Selected Area Electron Diffraction (SAED) analyses were performed on a Tecnai 20 transmission electron microscope with an accelerating voltage of 200 kV. Samples were drop cast onto formvar grids and air dried.

High Resolution Transmission electron Microscopy was performed at Georgia Tech on a FEI G2 Technai F30 with an accelerating voltage at 300 kV.

Scanning Electron Microscopy (SEM) analysis was performed on an FEI Teneo FE-SEM at 10 kV with a spot size of 10. Samples were dropcast onto a silicon wafer. Images were also taken on the same instrument at 30 kV in STEM mode.

For Atomic Force Microscopy (AFM), samples were dispersed in water, bath sonicated and drop cast onto a clean Si wafer. Data were collected with a Bruker Innova instrument in tapping mode. AFM data were analyzed with Nanoscope Analysis software.

Solid-State NMR Magic Angle Spinning experiments were performed at Georgia Tech on a Bruker 400 MHz with a spinning speed of 12 kHz.

Results and Discussion

The solvothermal reactions that lead to $LiMnPO_4$ nanosheets utilize a $Mn_3(PO_4)_2·3H_2O$ nanosheet precursor as well as LiH_2PO_4. $Mn_3(PO_4)_2·3H_2O$ nanosheets are conveniently prepared by mixing aqueous solutions of a manganese (II) salt and $(NH_4)_2HPO_4$ at room temperature. The resulting nanosheets exhibit lateral dimensions ranging from 0.5-4.0 µm as shown in figure

S3.1B. The AFM and corresponding height profile in Figure S3.1A reveal that the resulting nanosheets are <35 nm in thickness. Finally, the crystal structure is corroborated by X-ray diffraction figure S1C and matches well to the calculated pattern for $Mn_3(PO_4)_2{\cdot}3H_2O$ (JCPDS #00-003-0426).

The precipitation of $Mn_3(PO_4)_2{\cdot}3H_2O$ as nanosheets at room temperature without a structure-direct agent is rather unusual, and a direct result of the layered structure of $Mn_3(PO_4)_2{\cdot}3H_2O$. This compound lacks single crystal data and atomic coordinates, however, Nam and coworkers were able to use first-principles molecular dynamics to simulate the crystal structure based on removing four water molecules from the structure of $Mn_3(PO_4)_2{\cdot}7H_2O$.[15] The computationally determined structure of $Mn_3(PO_4)_2{\cdot}3H_2O$ contains planes of distorted MnO_5 and MnO_6 polyhedra that are edge and corner-shared to PO_4 tetrahedra, extending in the [100] and [010] direction. The structural hydrates are found in three unique bonding positions in each unit cell: bridging two Mn atoms, bound to Mn, or between the layers without bonds. The stronger, in-plane bonding of the Mn and PO_4 polyhedra versus the weaker out-of-plane hydrogen bonding is responsible for the anisotropic growth of this compound.

$Mn_3(PO_4)_2{\cdot}3H_2O$ nanosheets can also be formed with different Mn(II) salts and phosphate precursors. Figure S3.2 displays the TEM images highlighting the morphology of each $Mn_3(PO_4)_2{\cdot}3H_2O$ product when different precursors were used. $Mn_3(PO_4)_2{\cdot}3H_2O$ formed in all cases except during the reaction of LiH_2PO_4 with $MnSO_4{\cdot}H_2O$, $Mn(NO_3)_3{\cdot}4H_2O$ and $MnCl_2{\cdot}4H_2O$. In these instances, the total pH was <5.5, and not favorable for $Mn_3(PO_4)_2{\cdot}3H_2O$ precipitation. The lateral dimensions vary slightly across precursors, but overall, they exhibit the same two-dimensional morphology.

The relative ease of $Mn_3(PO_4)_2·3H_2O$ nanosheet formation demonstrates their propensity to form as an intermediate in many hydrothermal or solvothermal reactions that use similar precursors, and in fact, many synthetic methods employed in the literature would form this compound *in situ*. There are a couple reports of $Mn_3(PO_4)_2·3H_2O$ nanosheets directly in a solid state reaction to form $LiMnPO_4$[21] however, to the best of our knowledge there has been no effort to observe the direct reaction of this intermediate with a Li-containing compound in hydrothermal or solvothermal reactions and its effect on the growth of $LiMnPO_4$.

High quality $LiMnPO_4$ nanosheets were formed by reacting 5 mL of a 10 mg/ml aqueous dispersion of $Mn_3(PO_4)_2·3H_2O$ nanosheets, a 0.369 µL of a 1M LiH_2PO_4 solution, and 25 mL of DEG, under the solvothermal condtions of 250 °C for 6 h. Figure 3.1A shows a representative nanosheet of $LiMnPO_4$. The lateral dimensions range from 250 nm to a few micrometers, illustrated by the SEM image in figure S3.3. The AFM image and height profile in figure 1D reveal that the $LiMnPO_4$ nanosheets are approximately 5-6 nm in thickness. The XRD pattern in 3.1F matches to the calculated pattern for $LiMnPO_4$, JCPDS #01-072-7844. Additionally, the relative intensity of the peak at 16.8 2θ, reveals that these nanosheets exhibit the (200) plane. Figure 3.1B shows the HRTEM image of the nanosheet in 3.1A. The measured lattice fringes of 0.390 nm and 0.310 nm are in good agreement with the calculated d-spacings of 0.396nm and 0.305 nm for the (210) and (020) plane. Furthermore, the Fast Fourier Transform (FFT) in figure 3.1C agrees well with the calculated electron diffraction pattern of $LiMnPO_4$, shown in figure S3.4.

Low kV STEM images of the $LiMnPO_4$ nanosheets are shown in figure S3.5. The bright and dark field images clearly illustrate that the $LiMnPO_4$ nanosheets range from hundreds of nanometers to ~5 µm in length and width. The HAADF image reveals that the areas of higher contrast in the bright field image are from stacked $LiMnPO_4$ nanosheets. Finally, EDS mapping in STEM highlights the even distribution of Mn, O, and P present in the sample.

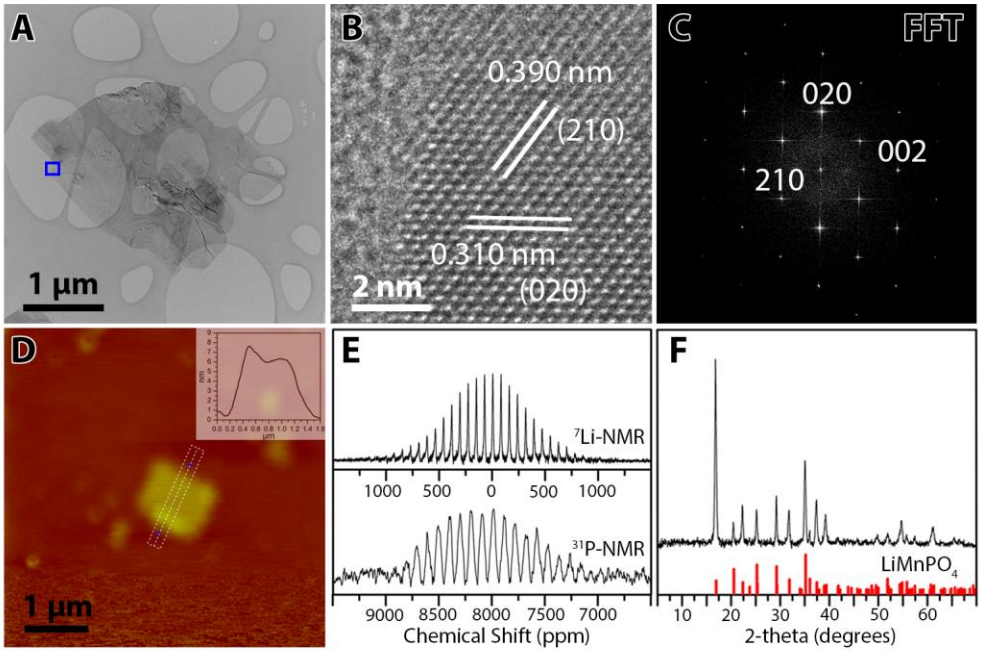

Figure 3.1: Characterization of $LiMnPO_4$ nanosheets formed solvothermally at 250 °C in 25:5 DEG:H_2O: A-B) TEM and HRTEM images of $LiMnPO_4$. C) Fast Fourier Transform of the HRTEM image in A. D) AFM image and height profile (inset). E) Solid-state ^{7}Li and ^{31}P-NMR spectra. F) XRD pattern and calculated pattern of $LiMnPO_4$ JCPDS # 01-072-7844.

We further confirmed the compound with magic-angle spinning (MAS) Solid State ^{31}P-NMR and ^{7}Li-NMR. The spectra are shown in Figure 1E. The isotropic chemical shift appears in the ^{31}P spectra occurs at approximately 7,984 ppm, while the shift for ^{7}Li occurs at 70.2 ppm. The surrounding peaks are attributed to spinning side bands; an artifact of the different spinning speeds for MAS NMR.

Both of these values closely match the values reported in the literatures of 7,296 ppm for ^{31}P-NMR and a ^{7}Li shift of 57-68 ppm for $LiMnPO_4$.[22] The relatively large shifts in both spectra arise from the transfer of unpaired electronic density of the Mn^{2+} d-orbitals to the NMR active nuclei. This transfer of electron density was denoted as the supertransferred hyperfine (STH) interaction by Wilcke and coworkers. Even though the chemical shifts for ^{31}P and ^{7}Li NMR occur by this same mechanism in $LiMnPO_4$, the large difference in chemical shifts is influenced by the covalency, or the ratio of unpaired electron density on the NMR active nuclei to that of the manganese nuclei. The much larger covalency of the P-O-Mn compared to that Li-O-Mn bond results in a higher downfield shift for ^{31}P-NMR.[22]

To gain more insight into the formation mechanism of $LiMnPO_4$ nanosheets, a time study was performed and monitored with XRD and TEM, shown in figure 3.2. The results illustrate that $LiMnPO_4$ forms after just 2 h. The TEM images of the 2 h and 4 h reveal a mixture of $LiMnPO_4$ nanosheets and nanoscrolls. At 6 h and 10 h the (200) peak in the XRD becomes noticeably more intense and highlights the growth of the (200) plane of $LiMnPO_4$. At these timepoints, no scrolling was observed, only nanosheets. Remarkably, this orientation effect is observed without sonication; we can therefore conclude that these sheets do not arise from heterostructured $LiMnPO_4$ broken apart by sonication, as observed by Zhao et al.[23]

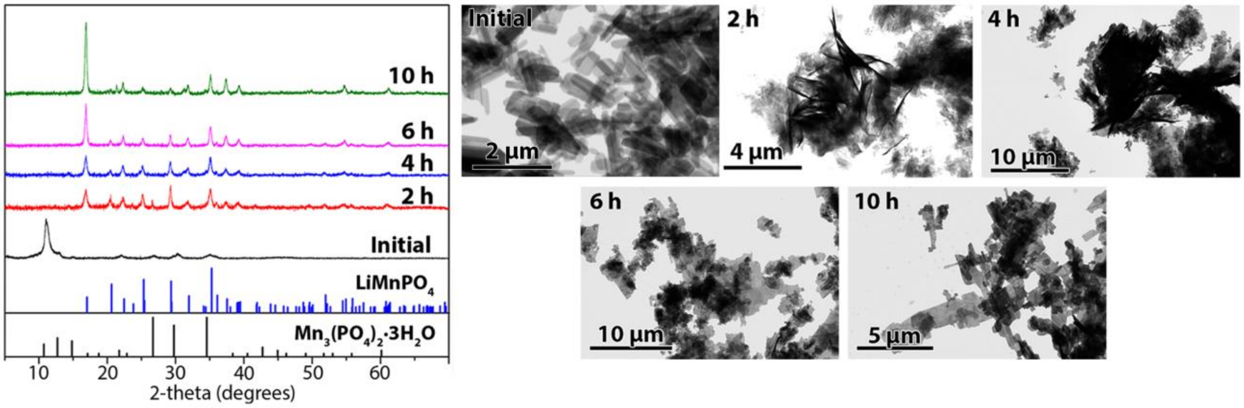

Figure 3.2: Time study of $LiMnPO_4$ formation at 250 °C analyzed with XRD and TEM.

Furthermore, there is no evidence of flower-like formation, even at 10 h. In Nie et al, $LiMnPO_4$ growth occurs over the course of a 10 h solvothermal reaction. This process occurs through a dissolution and renucleation mechanism followed by the formation of nanosheets and their self-assembly in to hierarchical flower-like structures.[13] However, it is important to point out that unlike similar one-pot syntheses in the literature, this reaction is not affected by the anion of the dissolved manganese salt, in this case, CH_3COO^-. While the effect of the anion of the Mn salt precursor is not conclusive, Wong and coworkers found that in a polyol synthesis, dissimilar morphologies of $LiMnPO_4$ could be obtained when using different Mn salts. The CH_3COO^- anion produced $LiMnPO_4$ with a smaller crystallite size, owing to its larger volume relative, whereas the SO_4^{2-} ion was determined to bond to higher order facets of the $LiMnPO_4$ crystal during growth.[24] Therefore eliminating these ions altogether by synthesizing and washing $Mn_3(PO_4)_2{\cdot}3H_2O$ nanosheets excludes their influence on the final morphology of $LiMnPO_4$.

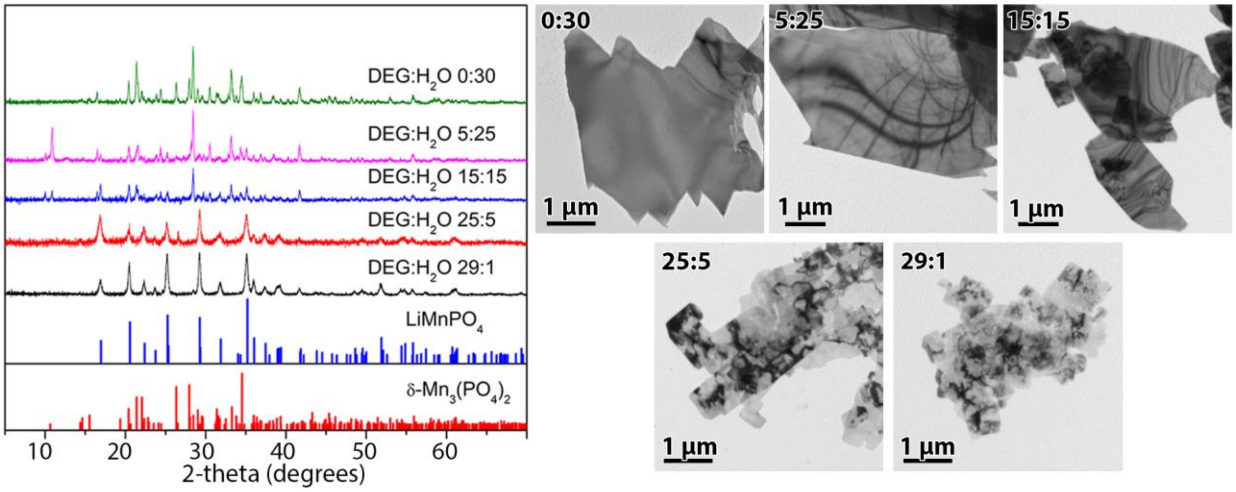

Figure 3.3: XRD patterns and SEM images of the product obtained from the solvothermal reaction of $Mn_3(PO_4)_2{\cdot}3H_2O$ using different ratios of DEG:H_2O at 250 °C for 6h.

A significant factor in this system is the DEG:H_2O ratio. Figure 3.3 shows the XRD patterns and TEM images of the product obtained from the reaction of $Mn_3(PO_4)_2{\cdot}3H_2O$ with different ratios of DEG:H_2O at 250 °C for 6h. When no DEG is used in the reaction (DEG:H_2O 0:30), nanoplates of δ-$Mn_3(PO_4)_2$ are formed. These nanoplates are also formed at ratios 5:25 and 15:15 DEG:H_2O, as observed in the XRD pattern. However, at 25:5 and 29:1 ratios of DEG:H_2O, the XRD patterns are indexed to pure $LiMnPO_4$, and contain no impurity peaks. The expected nanosheet morphology is observed even at a DEG:H_2O ratio as high as 29:1. Formation of δ-$Mn_3(PO_4)_2$ when only water is present is not surprising, as it was recently found to form from the hydrothermal reaction of $Mn_3(PO_4)_2{\cdot}3H_2O$ nanosheets at 250 °C for 6 h.[25] Figure S3.6 shows the characterization of δ-$Mn_3(PO_4)_2$ formed from this hydrothermal reaction. The experimental XRD diffraction pattern in figure S3.6A matches to the calculated pattern of δ-$Mn_3(PO_4)_2$, ICDD #1554313. The TEM and SEM images in S3.6B and S3.6C respectively, confirm that the lateral dimensions of these nanoplates are on the order of tens of microns.

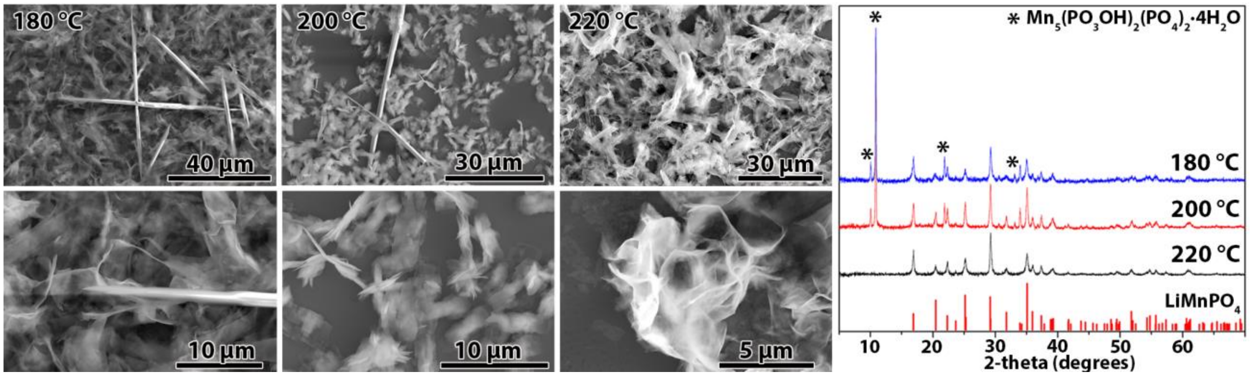

Figure 3.4: SEM images and XRD pattern of the solvothermal reaction of $Mn_3(PO_4)_2{\cdot}3H_2O$ nanosheets with LiH_2PO_4 at different temperatures. Each reaction was carried out with a 25:5 DEG:H_2O ratio.

Nanosheets of $LiMnPO_4$ in the form of crumpled sheets can be synthesized at temperatures <250°C, however, at these temperatures, the formation of $Mn_5(PO_4)_2(PO_3OH)_2{\cdot}4H_2O$ is favored. Figure 3.4 shows the SEM images and the XRD patterns for the products of the reaction of $Mn_3(PO_4)_2{\cdot}3H_2O$ nanosheets with LiH_2PO_4 at different temperatures, with a constant DEG:H_2O ratio of 25:5. At 220 °C, $LiMnPO_4$ is formed as crumpled nanosheets, as shown by SEM and the XRD pattern is indexed to $LiMnPO_4$. This morphology is also observed in 200 °C and 180 °C, but with an additional $Mn_5(PO_4)_2(PO_3OH)_2{\cdot}4H_2O$ impurity, as observed in the XRD patterns. This compound occurs naturally as the mineral hureaulite[26] and is known to form from $Mn_3(PO_4)_2{\cdot}3H_2O$ during reflux[19] and during hydrothermal reactions at 120 °C.[25] This $Mn_5(PO_4)_2(PO_3OH)_2{\cdot}4H_2O$ impurity occurs in the form of rods, >50 μm in length and <1 μm in width in dimensions, as observed in the SEM images.

This study illustrates that $Mn_5(PO_4)_2(PO_3OH)_2{\cdot}4H_2O$ readily forms at temperatures below 220 °C, even at a ratio of 25:5 DEG:H_2O. At greater temperatures, δ-$Mn_3(PO_4)_2$ impurities are not formed with this ratio, but they do form at lower ratios of DEG:H_2O. These findings suggest that one strategy for $LiMnPO_4$ nanosheet formation is to utilize the least amount of water as possible in this reaction, to quell the formation of stable manganese phosphate intermediates. In fact, this strategy has been utilized by Wang and coworkers to form $LiFePO_4$ nanosheets ~12 nm thick.[18]

Carrying out the same reaction but in a 25:5 ratio with ethylene glycol instead of DEG for 6 h also lead to $LiMnPO_4$—in the form of crumpled-up sheets. Figure S3.7 shows the XRD pattern and the corresponding SEM image for the product. The XRD pattern matches to $LiMnPO_4$, with several an impurity peaks belonging to δ-$Mn_3(PO_4)_2$. In comparison to the XRD pattern of the reaction with DEG, there is no indication of an orientation effect.

Interestingly, there is also a small difference of the final product on the initial conditions of the $Mn_3(PO_4)_2{\cdot}3H_2O$ nanosheets used. For all the experiments carried out, $Mn_3(PO_4)_2{\cdot}3H_2O$

nanosheets were taken from a colloidal suspension of washed nanosheets. However, if the $Mn_3(PO_4)_2·3H_2O$ nanosheets were dried at 120 °C and then redispersed in the appropriate amount of water, the final $LiMnPO_4$ product was significantly more flower-like. Figure S3.8 shows the comparison of the $LiMnPO_4$ product by using undried and dried at 120 °C. The difference is most noticeable in the XRD patterns—the $LiMnPO_4$ from $Mn_3(PO_4)_2·3H_2O$ dried at 120 °C exhibited a smaller orientation effect for the (200) at 16.98 2θ peak, whereas this peak was much larger for the $LiMnPO_4$ from undried $Mn_3(PO_4)_2·3H_2O$. The pH of each dispersed precursor is the same: $Mn_3(PO_4)_2·3H_2O$ after washing and $Mn_3(PO_4)_2·3H_2O$ nanosheets that were dried at 120 °C and then redispersed have a pH of 7.00-7.30. The surface area to volume ratio of different $Mn_3(PO_4)_2·3H_2O$ precursors may play a role, as those that were dried at 120 °C and redispersed (figure S3.9B) display thicker features (evidenced from the contrast in the TEM image) than those that were undried (figure 3.9A).

Nanosheets of $LiMnPO_4$ can also be obtained by using a different morphology of $Mn_3(PO_4)_2·3H_2O$ as well as different $Mn_3(PO_4)_2$ compounds. Nanoscrolls of $Mn_3(PO_4)_2·3H_2O$ can be synthesized by reacting a Mn(II) salt with $(NH_4)_2HPO_4$ in a solution of 25:5 EtOH:H_2O. The morphology of the nanoscrolls is shown in figure S3.10A. There is not 100% scrolling, as nanosheets of $Mn_3(PO_4)_2·3H_2O$ are still observed. Reacting this morphology with the same conditions used previously also resulted in nanosheets of $LiMnPO_4$, suggesting that nanosheet formation is independent of $Mn_3(PO_4)_2·3H_2O$ morphology.

Changing the $Mn_3(PO_4)_2·3H_2O$ precursor to δ-$Mn_3(PO_4)_2$ instead of $Mn_3(PO_4)_2·3H_2O$ and reacting for 4 h with the same conditions resulted in a slightly different morphology of $LiMnPO_4$. The XRD pattern in figure 3.5B shows that $LiMnPO_4$ is formed along with impurities unreacted δ-$Mn_3(PO_4)_2$. The SEM image shows that the obtained $LiMnPO_4$ morphology is formed as microplates. The TEM image shows that these structures undergo scrolling at the edges. The SAED pattern is clearly indexed to the d-spacings of $LiMnPO_4$. The β' polymorph was also reacted under the same conditions, for 4 h. The resulting XRD pattern in figure 3.5A matches to that of β'-$Mn_3(PO_4)_2$. The morphology of β'-$Mn_3(PO_4)_2$ is vastly different than that of δ-$Mn_3(PO_4)_2$ and is made of micron-sized three-dimensional aggregates. However, a sheet-like morphology is observed on the surface of these aggregates as shown in figure 3.5B. This morphology is evident in the TEM image. The SAED pattern confirms the structure of this compound, as they are indexed to the (200) plane of $LiMnPO_4$. The formation of $LiMnPO_4$ from both the β and δ phase of $Mn_3(PO_4)_2$ suggest that manganese phosphates in general are capable of reacting with LiH_2PO_4 under solvothermal conditions. The different $LiMnPO_4$ morphology may arise from the difference in structure and/or morphology, and may affect the nucleation rate of $LiMnPO_4$ on the surface.

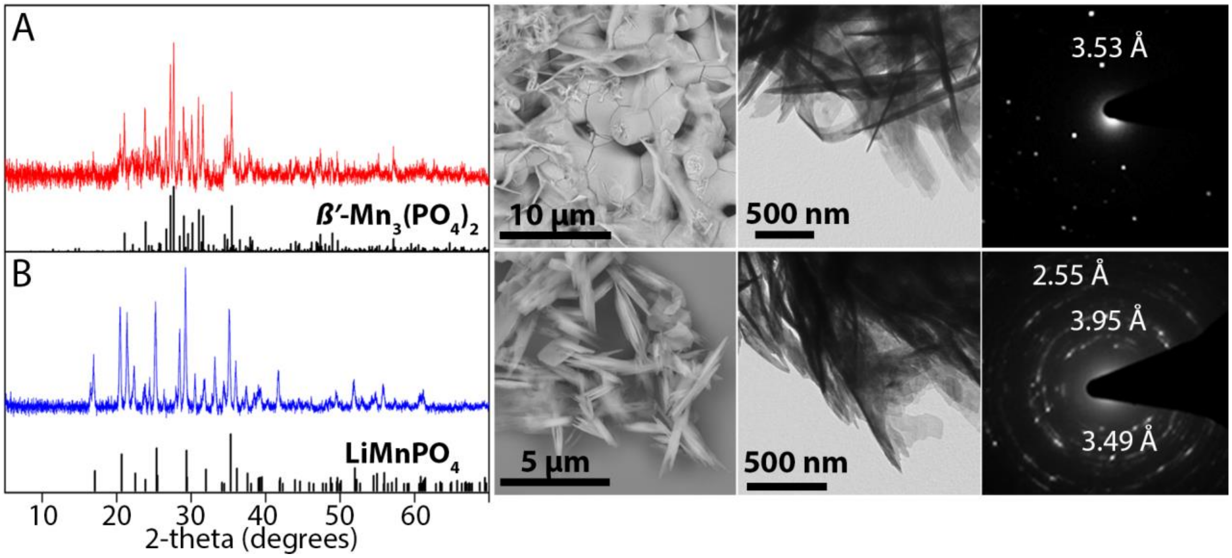

Figure 3.5: Row A: XRD pattern, SEM, TEM and SAED pattern respectively of the reaction of LiH_2PO_4 and β'-$Mn_3(PO_4)_2$ in DEG for 4h. Row B: XRD pattern, SEM, TEM, and SAED respectively of the reaction of LiH_2PO_4 and δ-$Mn_3(PO_4)_2$ in DEG for 4h.

A drastic change in $LiMnPO_4$ morphology was observed when the lithium phosphate salt was changed from LiH_2PO_4 to Li_3PO_4. Figure 3.6 shows the XRD pattern and SEM of the reaction of Li_3PO_4 with $Mn_3(PO_4)_2{\cdot}3H_2O$ nanosheets in a 25:5 DEG:H_2O ratio for 8 h. The XRD pattern matches to $LiMnPO_4$, without any observed impurity peaks. The SEM shows that the morphology is a mixture of three-dimensional prisms and aggregates that range from hundreds of nanometers to 3 µm in lateral dimensions. Similar morphologies were observed when this same reaction was carried out in H_2O. Figure S3.11A-C show the TEM, SEM, and XRD characterization data for this reaction. This resulting $LiMnPO_4$ product also forms as three-dimensional prisms. Finally, reaction of δ-$Mn_3(PO_4)_2$ with Li_3PO_4 yields similar morphologies, as shown in Figure S3.12B and S3.12C. There is also evidence of the formation of a Mn_2O_3 impurity, as shown in the XRD pattern in S3.12A. This may result from oxidation of the $LiMnPO_4$ nanosheets at these conditions, or it may form from the initial conditions of the hydrothermal formation of Mn_2O_3. The striking difference in morphology of the reactions using Li_3PO_4 and LiH_2PO_4 provides evidence that both the $H_2PO_4^-$ and PO_4^{3-} anions greatly impact the final morphology of the $LiMnPO_4$ product. Also, the absence of δ-$Mn_3(PO_4)_2$ and $Mn_5(PO_4)_2(PO_3OH)_2{\cdot}4H_2O$ impurities from the reactions with Li_3PO_4 suggest that the initial pH conditions of ~9.30 are unfavorable for their formation.

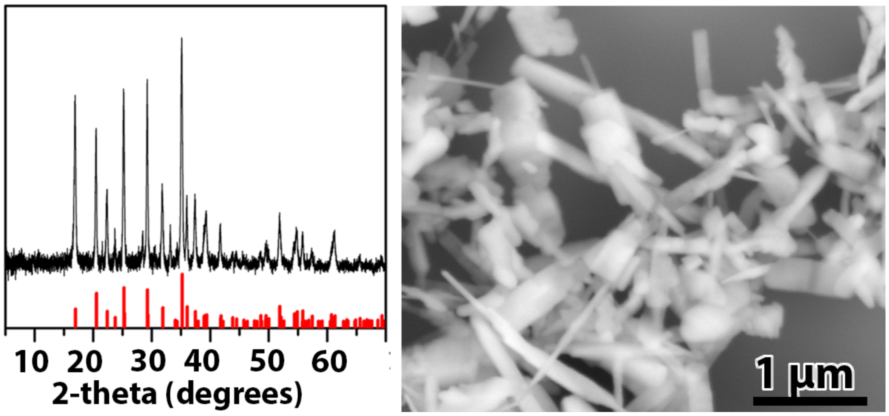

Figure 3.6: XRD pattern (left) and SEM image of the reaction of $Mn_3(PO_4)_2\cdot3H_2O$ nanosheets with Li_3PO_4 and a 25:5 ratio of DEG:H_2O.

Interestingly, using LiCl as the precursor did not result in $LiMnPO_4$; in fact, only $Mn_3(PO_4)_2\cdot3H_2O$ nanosheets were formed as shown in the XRD pattern in figure S3.13A. The TEM image in figure S3.13C reveals that the $Mn_3(PO_4)_2\cdot3H_2O$ product is scrolled. The other TEM image in figure S3.13D shows that in some instances the surface morphology of $Mn_3(PO_4)_2\cdot3H_2O$ nanosheets is porous. These results are remarkably similar to those obtained by same reaction conditions, without using a LiCl salt. Figures S3.14A-B show that reacting $Mn_3(PO_4)_2\cdot3H_2O$ in a 25:5 DEG:H_2O solvent ratio at 250 °C forms elongated belts of $Mn_3(PO_4)_2\cdot3H_2O$ nanosheets. Furthermore, the SEM image shows evidence of scrolled $Mn_3(PO_4)_2\cdot3H_2O$ nanosheets. In both instances, the $Mn_3(PO_4)_2\cdot3H_2O$ product is remarkably different than that of the precursor $Mn_3(PO_4)_2\cdot3H_2O$ nanosheets. These results suggest that $Mn_3(PO_4)_2\cdot3H_2O$ undergoes dissolution during the solvothermal reaction, and renucleates as $Mn_3(PO_4)_2\cdot3H_2O$ upon cooling. The fact that LiCl is not reactive with $Mn_3(PO_4)_2\cdot3H_2O$ demonstrates the importance of the lithium phosphate salt for $LiMnPO_4$ formation.

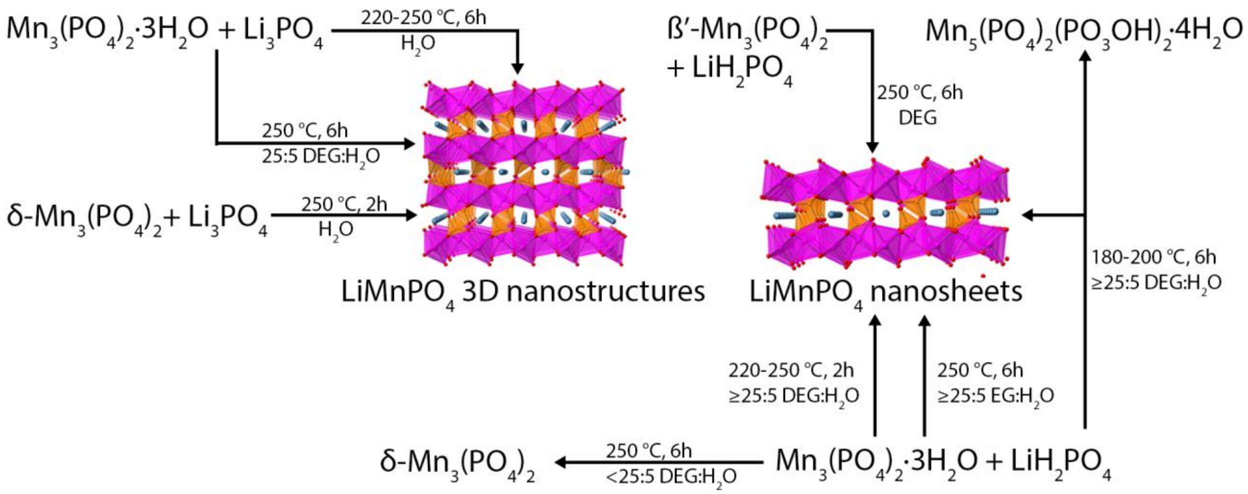

Figure 3.7: Schematic of the reactions that form $LiMnPO_4$ nanosheets and 3D nanostructures

Figure 3.7 summarizes the synthetic pathways that lead to different $LiMnPO_4$ nanomorphologies. The formation of $LiMnPO_4$ 3D nanostructures from Li_3PO_4 and $Mn_3(PO_4)_2 \cdot 3H_2O$ precursors follows a similar dissolution-renucleation pathway reported by Chung and coworkers. Here, $Mn_3(PO_4)_2 \cdot 3H_2O$ nanosheets were formed *in-situ* through the reaction of Li_3PO_4 with Mn(II) ions in solution. Excess Li_3PO_4 dissolved and reacted with the $Mn_3(PO_4)_2 \cdot 3H_2O$ nanosheets to form $LiMnPO_4$ nuclei, which then underwent self-assembly and Otswald ripening to form nanomorphologies of $LiMnPO_4$.[20]

Observations of the three-dimensional nanomorphologies are also in line with the thermodynamic conditions that lead to the precipitation of $LiMnPO_4$ reported by Delacourt et al. This report shows that $LiMnPO_4$ precipitates out of solution at a pH of ~10.5. This was backed up by experimental evidence—taking an aqueous solution of Mn^{2+}, PO_4^{3-} and Li^+ ions, and adjusting the pH to 10.7 with LiOH lead to $LiMnPO_4$ under reflux conditions. The formation of $Mn_3(PO_4)_2 \cdot 3H_2O$ nanosheets and $Mn_5(PO_4)_2(PO_3OH)_2 \cdot 4H_2O$ intermediates were observed at reaction times <2 h.[19] These observations are similar to our results when Li_3PO_4 was used as the lithium phosphate precursor in both DEG and H_2O conditions. Furthermore, the pH of the precursor reaction mixture was ~9.30—well in the pH range for $LiMnPO_4$ formation.

Notably, the precursor reaction conditions that lead to $LiMnPO_4$ nanosheets occur at a pH of ~6.30, well below the optimal 10.7 pH for $LiMnPO_4$ precipitation. The lower pH is due to the dissolution of LiH_2PO_4, which forms the $H_2PO_4^-$ anion in solution. Our results show that $LiMnPO_4$ can form at this pH, but under more strict conditions than that of the higher pH system. For example, at this pH range δ-$Mn_3(PO_4)_2$ and $Mn_5(PO_4)_2(PO_3OH)_2{\cdot}4H_2O$ are favored, as observed from the solvent and temperature studies. At higher pH values, such as in the Delacourt paper, $Mn_5(PO_4)_2(PO_3OH)_2{\cdot}4H_2O$ was formed as an intermediate at times <2 h, but it eventually dissolved and precipitated out as $LiMnPO_4$. At temperatures of 180-200 °C, such as in our study, $Mn_5(PO_4)_2(PO_3OH)_2{\cdot}4H_2O$ was formed (even with a 25:5 DEG:H_2O) ratio, but did not further react, even at 6 h. Furthermore, adding more H_2O in the initial precursor suspension, and reacting at 250 °C for 6 h resulted in δ-Mn_3PO_4. This compound was not an intermediate on the way to $LiMnPO_4$ formation; instead, it was the final product. These findings suggest that manganese phosphates are much more stable at neutral pH than $LiMnPO_4$.

Limiting the water in the system mitigated the formation of δ-$Mn_3(PO_4)_2$ and $Mn_5(PO_4)_2(PO_3OH)_2{\cdot}4H_2O$ impurities suggesting that $LiMnPO_4$ formed directly by reaction with the $Mn_3(PO_4)_2{\cdot}3H_2O$ precursors. Similar experiments were tested by Wang and coworkers on $LiFePO_4$. In this system, $LiFePO_4$ followed different reaction pathways based on whether H_2O or EG was used as the solvent. When only H_2O was the solvent, the Li_3PO_4, and $FeSO_4{\cdot}7H_2O$ reactants formed an $Fe_3(PO_4)_2{\cdot}8H_2O$ intermediate, on the way to forming $LiFePO_4$ under hydrothermal conditions at 180 °C. Replacing the H_2O with EG under the same conditions, amorphous intermediates were observed instead, but the end product was still $LiFePO_4$. The authors speculated that adding water favored the formation of the $Fe_3(PO_4)_2{\cdot}8H_2O$ intermediate, and facilitated the dissolution of Li_3PO_4.[27] Additionally, this waterless strategy was applied in another report to successfully synthesize 12 nm thick nanosheets of $LiFePO_4$.[18]

Additionally, DEG may have the added benefit of binding to certain facets of metal phosphate and nanomaterials during the nucleation process. DEG is known to exhibit strong bonding with (020) plane of $LiFePO_4$[23] and may act as a structure-directing agent to form $LiMnPO_4$ nanosheets. Furthermore, DEG and other polyols are known to prevent agglomeration of the final products.[28] However, DEG was also used in the solvothermal reaction that produced $LiMnPO_4$ 3D nanomorphologies and two-dimensional growth was not observed. Therefore, the phosphate anion may have a larger impact on the growth of $LiMnPO_4$ than DEG.

Phosphate anions are known to selectively adsorb to certain faces of hematite during nucleation.[29],[30] ZnO nanosheets were synthesized by the reaction of the Zn salt and Na_3PO_4. The phosphate anions adsorbed to the (001) face and restricted growth in the [001] direction.[31] The 3D nanomorphologies produced by the solvothermal reaction with Li_3PO_4 versus the two-dimensional morphologies formed by reaction with LiH_2PO_4 provide evidence for the structure-directing growth of the $H_2PO_4^-$ anion. This anion may adsorb to the (200) plane of $LiMnPO_4$ as it grows outwards, mitigating growth in the [020] directions. Two-dimensional morphologies of $LiMnPO_4$ are also observed in other reports that use LiH_2PO_4 as the precursor in a solvothermal reaction. These morphologies range from 15-35 nm thick platelets[15],[32],[16],[33],[34],[35] to flower-like clusters with nanoplates ~30 nm[13],[36]. It is important to point out however, that in all of these reports, EG or DEG were used as the solvent. There are far fewer reports of two-dimensional growth using Li_3PO_4 in the literature (or using reaction parameters that form Li_3PO_4 *in-situ*, such as by combining solutions of LiOH and H_3PO_4).

However, it is interesting that using LiCl as the precursor did not result in $LiMnPO_4$. Dissolution of $Mn_3(PO_4)_2 \cdot 3H_2O$ would yield PO_4^{3-} and Mn^{2+} ions, which along with Li^+ ions should provide a conducive environment for $LiMnPO_4$ formation. Instead, $Mn_3(PO_4)_2 \cdot 3H_2O$ is the final product under these conditions. Therefore, it is vital to have phosphate anions in solution, either to tune the pH or to react with the $Mn_3(PO_4)_2 \cdot 3H_2O$ precursors in the presence of Li ions.

Finally, the formation of $LiMnPO_4$ nanosheets may also occur by way of a dissolution-renucleation mechanism. Evidence for this mechanism is taken from the time study of $LiMnPO_4$ nanosheet formation study. No intermediates are observed at any time in this reaction. Furthermore, formation of $LiMnPO_4$ nanosheets from $Mn_3(PO_4)_2 \cdot 3H_2O$ nanoscrolls indicates that the initial sheet-like morphology is not necessary for the final $LiMnPO_4$ nanosheet morphology.

Based on these results, we propose the following reaction pathway for $LiMnPO_4$ nanosheets formation. 1.) $Mn_3(PO_4)_2 \cdot 3H_2O$ nanosheets provide nucleation sites for the formation of $LiMnPO_4$. At less than 1 h, $Mn_3(PO_4)_2 \cdot 3H_2O$ nanosheets react with Li^+ and $H_2PO_4^-$ to form $LiMnPO_4$ nuclei. 2.) The large amount of DEG in the reaction both binds to the surface of the newly formed $LiMnPO_4$ and prevents the more favorable δ-$Mn_3(PO_4)_2$ from forming. 3.) The crystal growth of nucleating $LiMnPO_4$ nanosheets proceeds in the [020] and [002] directions as a result of $H_2PO_4^-$ anion and H^+ that selectively bond to the (200) planes of $LiMnPO_4$.

Because of the low electronic conductivity of $LiFePO_4$ (10^{-9}-10^{-10} cm^{-1}) and $LiMnPO_4$ ($<10^{-10}$) S cm^{-1} [3] it is imperative to coat these materials with a conductive layer of carbon—even mixing with a carbon source during the slurry-making process is insufficient enough to produce any achievable electrochemical activity. A few reports in the literature have tested “bare”

$LiMnPO_4$ or $LiMnPO_4$ without a conductive layer of surface carbon, however, no appreciable electrochemical activity was obtained,[37],[33], highlighting the importance of a conductive layer of carbon.

One of the most common approaches to carbon-coating nanostructured materials is to mix $LiMnPO_4$ with a carbon containing precursor, such as glucose or sucrose, followed by annealing at temperatures >600 °C in flowing Ar. The goal is to create a few nm thick amorphous carbon coating layer, that provides high conductivity in the material without compromising Li^+ ion diffusion.[38] The main concern at temperatures >600 °C is the morphology breakdown, however, Qian and coworkers showed that nanorods of $LiMnPO_4$ approximately 100-600 nm in dimensions were able to preserve their morphology when annealed at 700 °C with carbon-containing precursors.[4] Furthermore, the optimal carbon coating for a materials is vital—Chen and coworkers found that optimal amount of glucose to yield a < 3nm thick carbon layer on $LiMnPO_4$ was 20 wt%. At higher carbon loadings, the material suffered a decrease in electrochemical performance, as result of higher impedance values. [39]

Using the standard annealing method, we first ball-milled $LiMnPO_4$ nanosheets (from the reaction of $Mn_3(PO_4)_2{\cdot}3H_2O$ with LiH_2PO_4 in 25:5 DEG:H_2O) with 30 wt% glucose in 5 ml ethanol. SEM and TEM of the dried, ball-milled product is shown in figure S3.15. The nanosheets maintain their two-dimensional morphology, with slightly decreased lateral dimensions. Next, the $LiMnPO_4$ glucose mixture was annealed in a quartz tube sealed under vacuum for 6 h at 600 °C. TEM image of the product after annealing can also be observed in figure S3.15 SEM and EDS mapping shows that the C, Mn, O, and P overlap well with each other, arising from the uniformity of the carbon coating.

Figure 3.8 presents the electrochemical data of the $LiMnPO_4/C$ nanosheets. The cyclic voltammagram (CV) curve of the first charge-discharge cycle displays a reduction peak at 3.93 V, corresponding to Mn^{3+} reduction to Mn^{2+}. The discharge and charge profiles show that the discharge capacity of $LiMnPO_4$ reaches about 30 mAh/g at a current rate of C/80. The discharge curve displays a voltage plateau at about 4.0 V, indicative of the two phase insertion of Li^+ into $LiMnPO_4$.[1] At higher currents, the discharge capacity decreases, and virtually no plateau is observed for cells cycled at 0.5 C, 0.1 C, and 0.05 C. Despite the relatively low discharge capacities, $LiMnPO_4/C$ nanosheets do show promise cycling ability. At C/20, this material shows little capacity fading over 27 cycles. In fact, a slight increase in discharge capacity was observed.

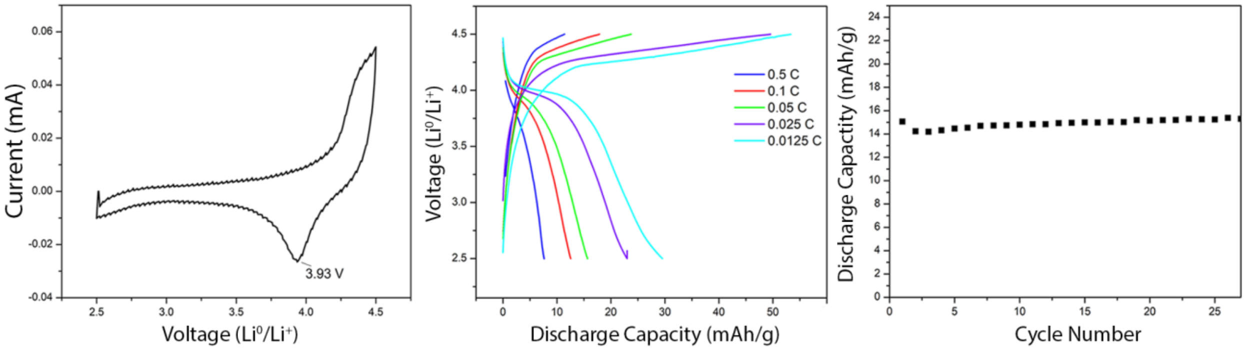

Figure 3.8: Electrochemical data for $LiMnPO_4/C$ nanosheets. Left: CV of the first charge/discharge cycle. Middle: Discharge capacities and charge capacities of the first cycle at different C rates. Right: Discharge capacity loss with $LiMnPO_4$ when cycled at C/20.

Future work aims to optimize the carbon-coating to achieve discharge capacities closer to the theoretical discharge capacity of 171 mAh/g.

Conclusion

Here we detailed a method to synthesize anistropic nanosheets of $LiMnPO_4$ using $Mn_3(PO_4)_2{\cdot}3H_2O$ nanosheets as precursors. $Mn_3(PO_4)_2{\cdot}3H_2O$ nanosheets were synthesized by a simple precipitation reaction of manganese (II) solution and a phosphate solution. Solvothermal treatment of the $Mn_3(PO_4)_2{\cdot}3H_2O$ nanosheets at 250 °C with a 25:5 DEG:H_2O lead to <6 nm thick nanosheets of $LiMnPO_4$. Temperature, DEG:H_2O, and lithium phosphate precursor all play a significant role in the structure and the morphology of the final product. Our findings suggest that the high-surface area $Mn_3(PO_4)_2{\cdot}3H_2O$ nanosheets provide many nucleation sites for the formation of $LiMnPO_4$. This chemistry shows potential for extension to other metal phosphate systems, such as $LiNiPO_4$ and $LiCoPO_4$, which both contain analogous $M_3PO_4{\cdot}8H_2O$ hydrated intermediates. Additionally, this system is interesting to study from a lithium-diffusion standpoint. The $LiMnPO_4$ nanosheets display the (200) plane, and the most favorable lithium diffusion pathway occurs parallel to this plane. However, even though the $LiMnPO_4$ nanosheets do not exhibit the ideal (020) plane, there may be several advantages, such as increased coherency strain between $LiMnPO_4$ and $MnPO_4$ which was responsible for the superior electrochemical performance of the (200)-oriented $LiFePO_4$ nanosheets.[18] Future work aims to optimize the carbon coating to achieve higher discharge capacities.

References

[1] A. K. Padhi, K. S. Nanjundaswamy and J. B. Goodenough, *Journal of The Electrochemical Society* **1997**, *144*, 1188-1194.

[2] K. Zaghib, J. Dubé, A. Dallaire, K. Galoustov, A. Guerfi, M. Ramanathan, A. Benmayza, J. Prakash, A. Mauger and C. M. Julien, *Journal of Power Sources* **2012**, *219*, 36-44.

[3] D. Choi, D. Wang, I.-T. Bae, J. Xiao, Z. Nie, W. Wang, V. V. Viswanathan, Y. J. Lee, J.-G. Zhang, G. L. Graff, Z. Yang and J. Liu, *Nano Letters* **2010**, *10*, 2799-2805.

[4] L.-e. Li, J. Liu, L. Chen, H. Xu, J. Yang and Y. Qian, *RSC Advances* **2013**, *3*, 6847.

[5] T. N. L. Doan and I. Taniguchi, *Journal of Power Sources* **2011**, *196*, 1399-1408.

[6] X. Zhou, F. Wang, Y. Zhu and Z. Liu, *Journal of Materials Chemistry* **2011**, *21*, 3353.

[7] D. Morgan, A. Van der Ven and G. Ceder, *Electrochemical and Solid-State Letters* **2004**, *7*, A30-A32.

[8] M. S. Islam, D. J. Driscoll, C. A. J. Fisher and P. R. Slater, *Chemistry of Materials* **2005**, *17*, 5085-5092.

[9] S. Y. Chung, S. Y. Choi, S. Lee and Y. Ikuhara, *Phys Rev Lett* **2012**, *108*, 195501.

[10] S.-Y. Chung, S.-Y. Choi, T.-H. Kim and S. Lee, *ACS Nano* **2015**, *9*, 850-859.

[11] R. Amisse, M. T. Sougrati, L. Stievano, C. Davoisne, G. Dražič, B. Budič, R. Dominko and C. Masquelier, *Chemistry of Materials* **2015**, *27*, 4261-4273.

[12] T. R. Kim, D. H. Kim, H. W. Ryu, J. H. Moon, J. H. Lee, S. Boo and J. Kim, *Journal of Physics and Chemistry of Solids* **2007**, *68*, 1203-1206.

[13] P. Nie, L. Shen, F. Zhang, L. Chen, H. Deng and X. Zhang, *CrystEngComm* **2012**, *14*, 4284.

[14] R. K. Petla, M. Venkateswarlu and N. Satyanarayana, *Three-dimensional lithium manganese phosphate microflowers for lithium-ion battery applications*, **2012**, p.

[15] D. Wang, H. Buqa, M. Crouzet, G. Deghenghi, T. Drezen, I. Exnar, N.-H. Kwon, J. H. Miners, L. Poletto and M. Grätzel, *Journal of Power Sources* **2009**, *189*, 624-628.

[16] N. P. W. Pieczonka, Z. Liu, A. Huq and J.-H. Kim, *Journal of Power Sources* **2013**, *230*, 122-129.

[17] X. Rui, X. Zhao, Z. Lu, H. Tan, D. Sim, H. H. Hng, R. Yazami, T. M. Lim and Q. Yan, *ACS Nano* **2013**, *7*, 5637-5646.

[18] Z. Li, Z. Peng, H. Zhang, T. Hu, M. Hu, K. Zhu and X. Wang, *Nano Lett* **2016**, *16*, 795-799.

[19] C. Delacourt, P. Poizot, M. Morcrette, J. M. Tarascon and C. Masquelier, *Chemistry of Materials* **2004**, *16*, 93-99.

[20] S.-L. Yang, R.-G. Ma, M.-J. Hu, L.-J. Xi, Z.-G. Lu and C. Y. Chung, *Journal of Materials Chemistry* **2012**, *22*, 25402.

[21] a) H.-J. Zhu, W. Zhai, M. Yang, X.-m. Liu, Y.-C. Chen, H. Yang and X.-d. Shen, *RSC Advances* **2014**, *4*, 25625; b) Q. Xia, T. Liu, J. Xu, X. Cheng, W. Lu and X. Wu, *Journal of Materials Chemistry A* **2015**, *3*, 6301-6305.

[22] Y.-J. L. S.L. Wilcke, E.J. Cairns. J.A. Reimer, *Appl. Magn. Reson.* **2007**, 547-563.

[23] Y. Zhao, L. Peng, B. Liu and G. Yu, *Nano Lett* **2014**, *14*, 2849-2853.

[24] F. Zhou, P. Zhu, X. Fu, R. Chen, R. Sun and C.-p. Wong, *CrystEngComm* **2014**, *16*, 766-774.

[25] G. Neher and T. T. Salguero, *Crystal Growth & Design* **2017**.

[26] S. Menchetti and C. Sabelli, *Acta Crystallographica Section B* **1973**, *29*, 2541-2548.

[27] Z. Li, K. Zhu, J. Li and X. Wang, *CrystEngComm* **2014**, *16*, 10112-10122.

[28] F. Fievet, J. P. Lagier, B. Blin, B. Beaudoin and M. Figlarz, *Solid State Ionics* **1989**, *32-33*, 198-205.

[29] M. Ocaña, M. P. Morales and C. J. Serna, *Journal of Colloid and Interface Science* **1995**, *171*, 85-91.

[30] B. Lv, Y. Xu, D. Wu and Y. Sun, *CrystEngComm* **2011**, *13*, 7293-7298.

[31] I. Hiroaki, I. Satoko and Y. Satoshi, *Chemistry Letters* **2004**, *33*, 768-769.

[32] T. Kodera, F. Isobe and T. Ogihara, *Preparation and Electrochemical Properties of LiMnPO4 Nanoparticles by Polyol Method*, **2013**, p. 95-98.

[33] Y. Kadoma, K. Harata, H. Watanabe, N. Kumagai and K. Ui, *Electrochemistry* **2014**, *82*, 456-461.

[34] H.-J. Zhu, X.-M. Liu, H. Yang and X.-D. Shen, *Ceramics International* **2014**, *40*, 6699-6704.

[35] L. Peng, X. Zhang, Z. Fang, Y. Zhu, Y. Xie, J. J. Cha and G. Yu, *Chemistry of Materials* **2017**, *29*, 10526-10533.

[36] C. Wang, S. Li, Y. Han and Z. Lu, *ACS Applied Materials & Interfaces* **2017**, *9*, 27618-27624.

[37] H. Guo, C. Wu, L. Liao, J. Xie, S. Zhang, P. Zhu, G. Cao and X. Zhao, *Inorg Chem* **2015**, *54*, 667-674.

[38] H. Li and H. Zhou, *Chem Commun (Camb)* **2012**, *48*, 1201-1217.

[39] K. Su, F. Liu and J. Chen, *Journal of Power Sources* **2013**, *232*, 234-239.

Supporting Information

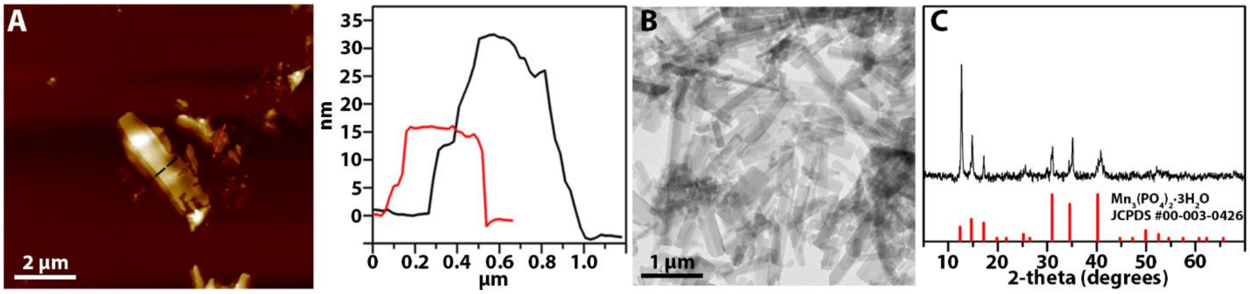

Figure S3.1: Characterization of $Mn_3(PO_4)_2{\cdot}3H_2O$ nanosheets: A) AFM image and height profile B) TEM image C) Experimental (black) and calculated (red) pattern for $Mn_3(PO_4)_2{\cdot}3H_2O$, JCPDS #00-003-0426.

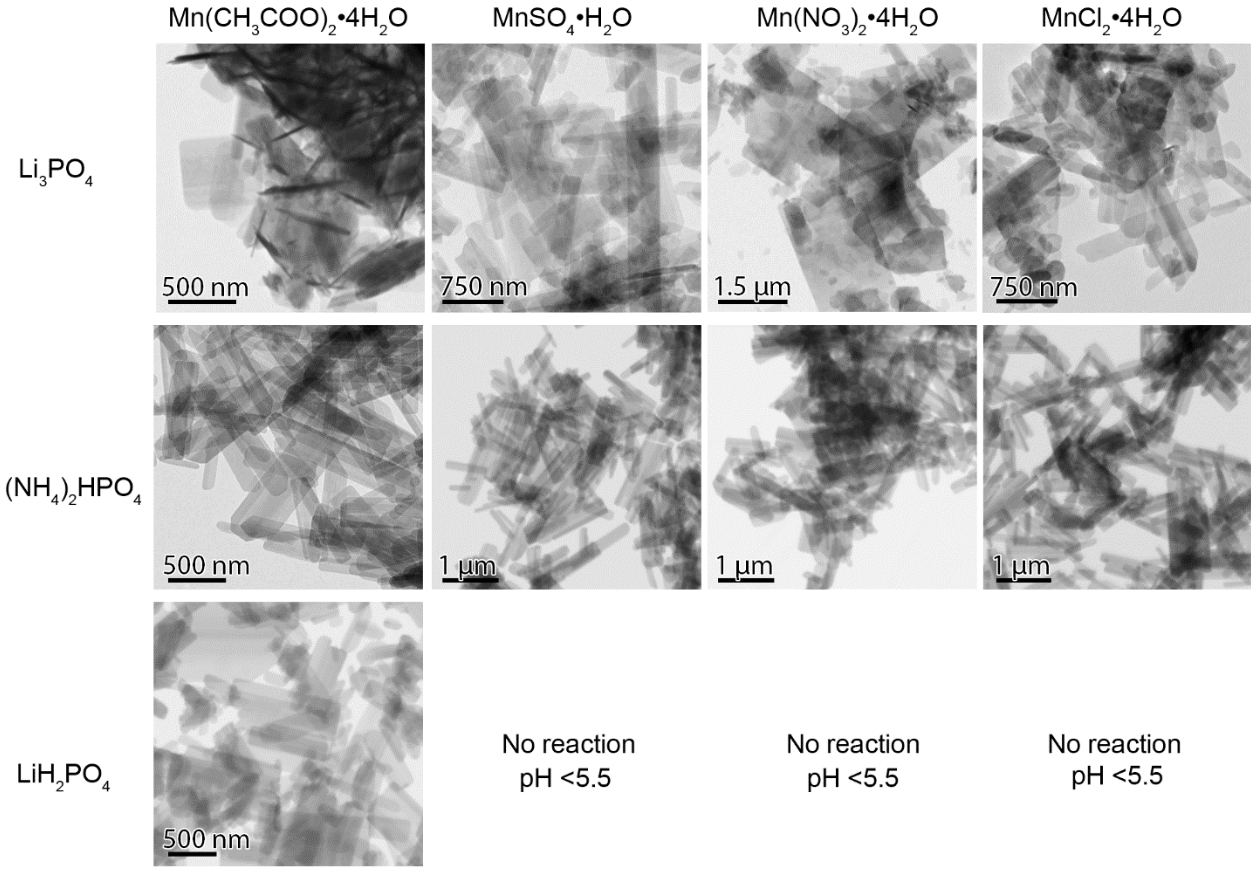

Figure S3.2: TEM images of $Mn_3(PO_4)_2 \cdot 3H_2O$ nanosheets formed from the reaction of different Mn(II) and phosphate salt precursors. The lateral dimensions of the $Mn_3(PO_4)_2 \cdot 3H_2O$ nanosheets vary slightly, but the overall morphology for each successful reaction is similar. $Mn_3(PO_4)_2 \cdot 3H_2O$ nanosheets did not form in instances where the total pH of the solution was less than 5.5.

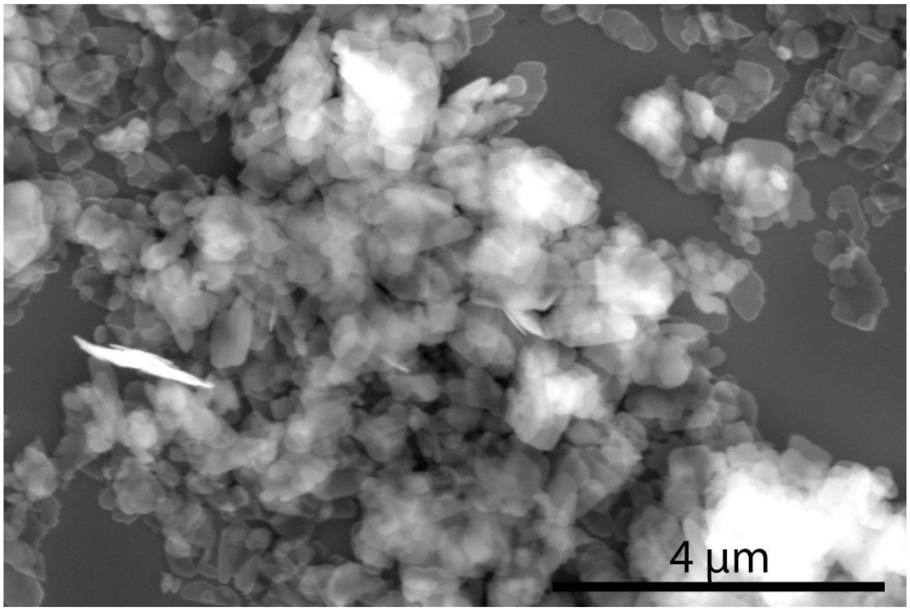

Figure S3.3: SEM image of $LiMnPO_4$ nanosheets

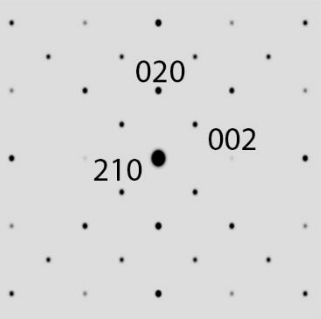

Figure S3.4: Calculated SAED pattern of the (200) plabe of $LiMnPO_4$

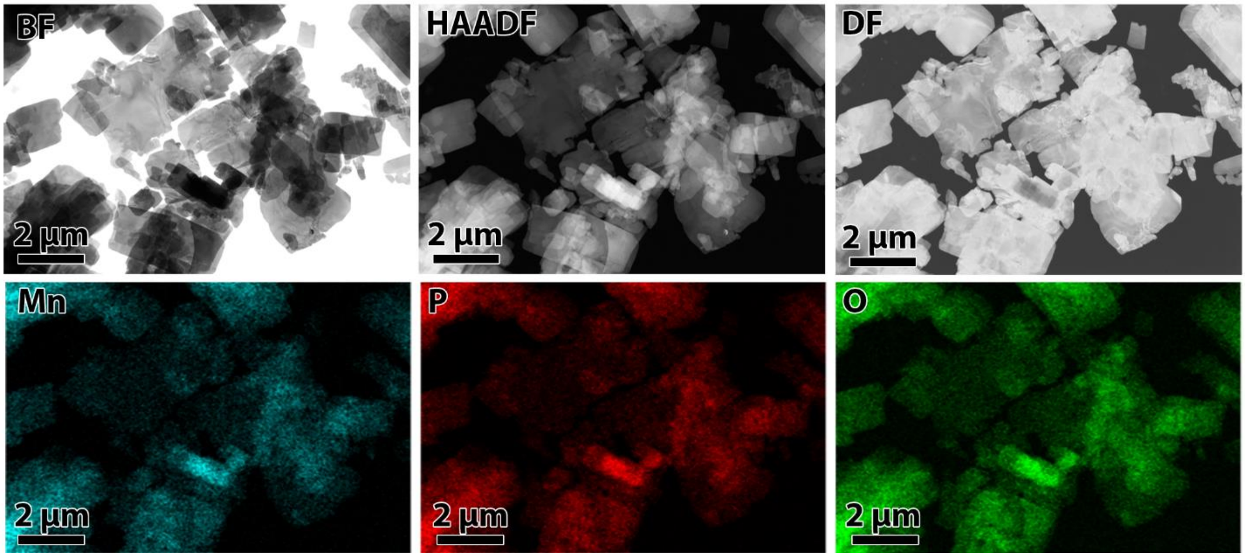

Figure S3.5: Low kV STEM images of $LiMnPO_4$ nanosheets in bright field (BF), high angle annular dark field (HAADF), and dark field (DF) modes. EDS mapping shows even distribution of Mn, P, and O.

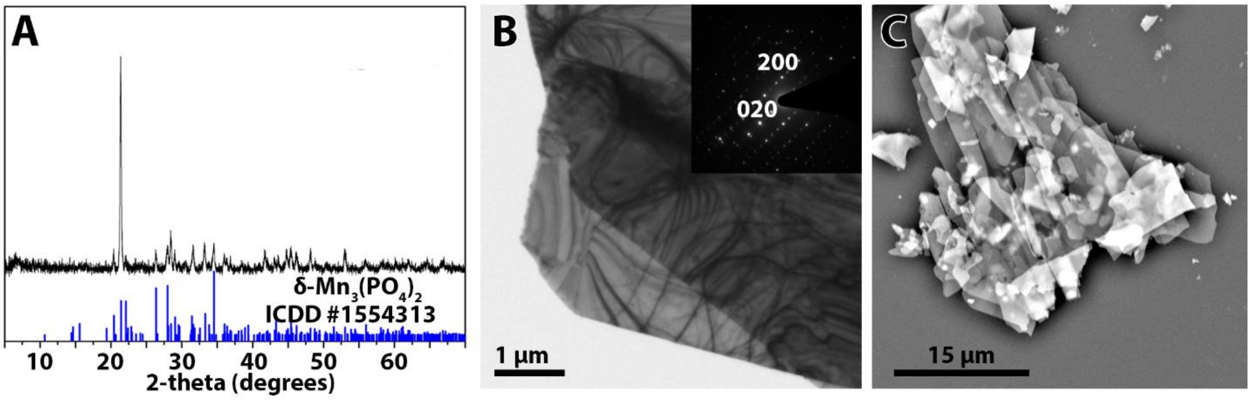

Figure S3.6: Characterization of δ-$Mn_3(PO_4)_2$ nanoplates from the hydrothermal reaction of $Mn_3(PO_4)_2 \cdot 3H_2O$ nanosheets at 250 °C: A) Experimental XRD pattern (black) and calculated diffraction pattern for δ-$Mn_3(PO_4)_2$ (blue lines) ICDD #1554313 B) TEM image of δ-$Mn_3(PO_4)_2$ nanoplates and SAED (inset) C) SEM image of δ-$Mn_3(PO_4)_2$ nanoplates.

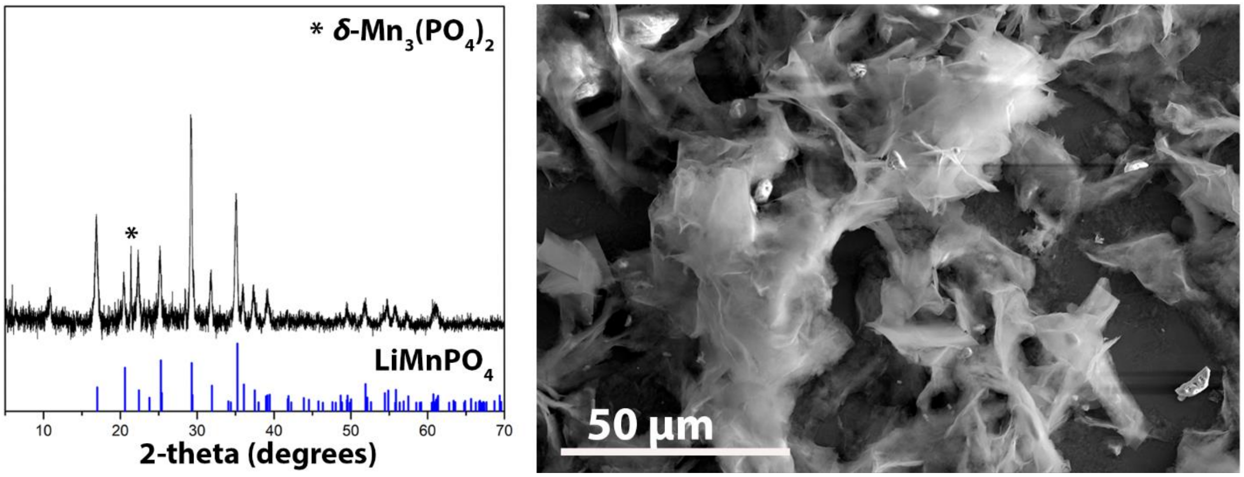

Figure S3.7: XRD pattern (left) and SEM images of the $LiMnPO_4$ highlighting the crumpled nature of the product from the solvothermal reaction with EG at 250 °C for 6 hours, instead of DEG. Impurity peak in the XRD pattern belongs to δ-$Mn_3(PO_4)_2$.

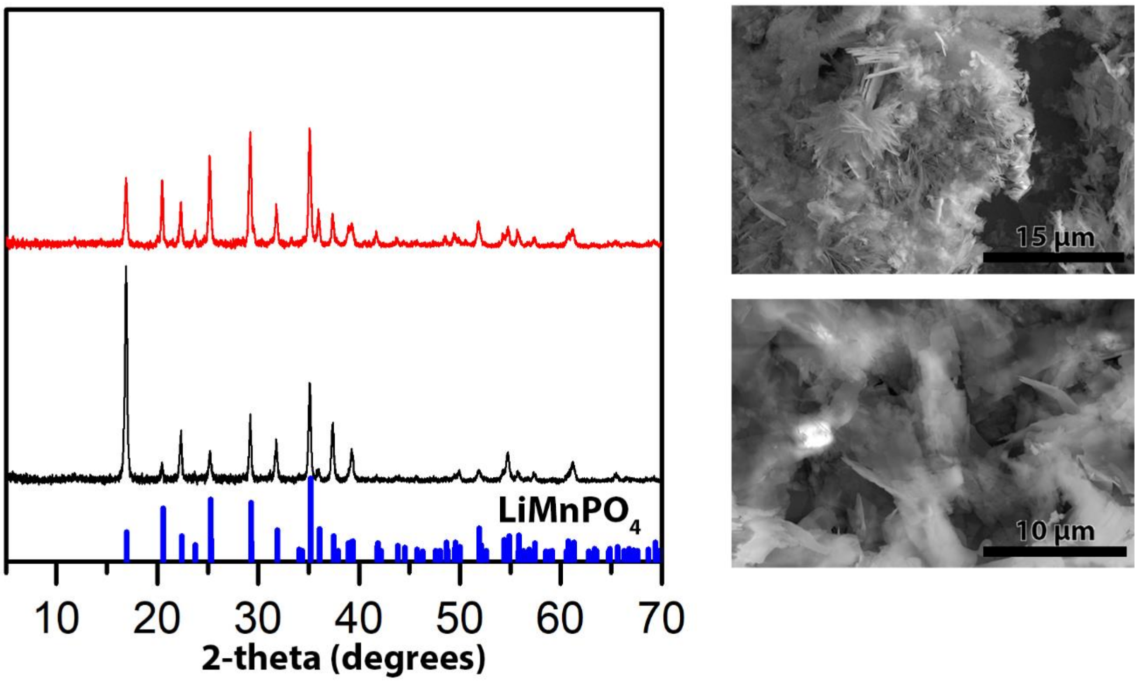

Figure S3.8: XRD patterns of the final $LiMnPO_4$ product using “dried” (red) or “undried” (blue) $Mn_3(PO_4)_2·3H_2O$ nanosheets as the precursor and reaction for 8 h hydrothermally to 250 °C Using dried $Mn_3(PO_4)_2·3H_2O$ results in flower-like structures, as shown in the SEM image on top right panel, while undried $Mn_3(PO_4)_2·3H_2O$ nanosheets results in two dimensional nanosheets, bottom right panel.

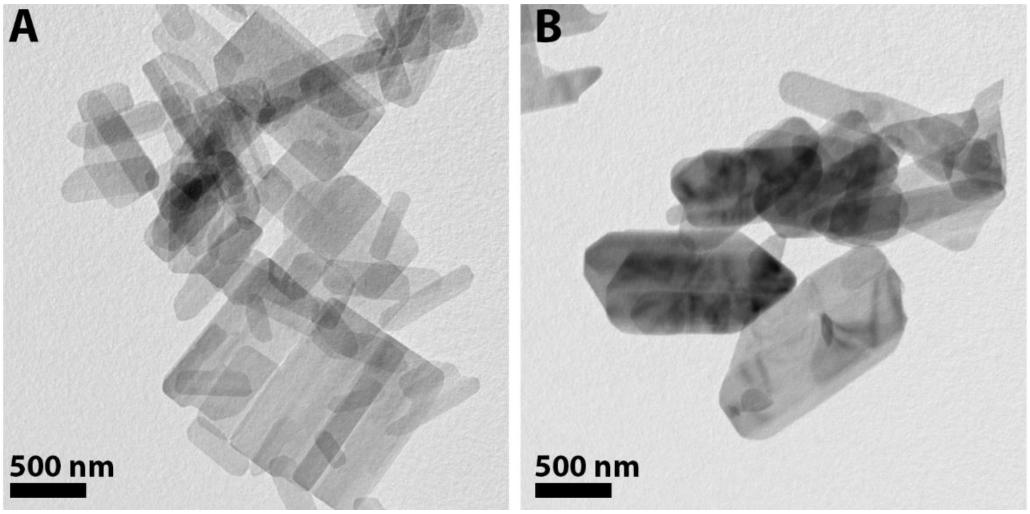

Figure S3.9: A) $Mn_3(PO_4)_2·3H_2O$ washed and redispersed B) $Mn_3(PO_4)_2·3H_2O$ washed and dried at 120 °C, and redispersed in H_2O

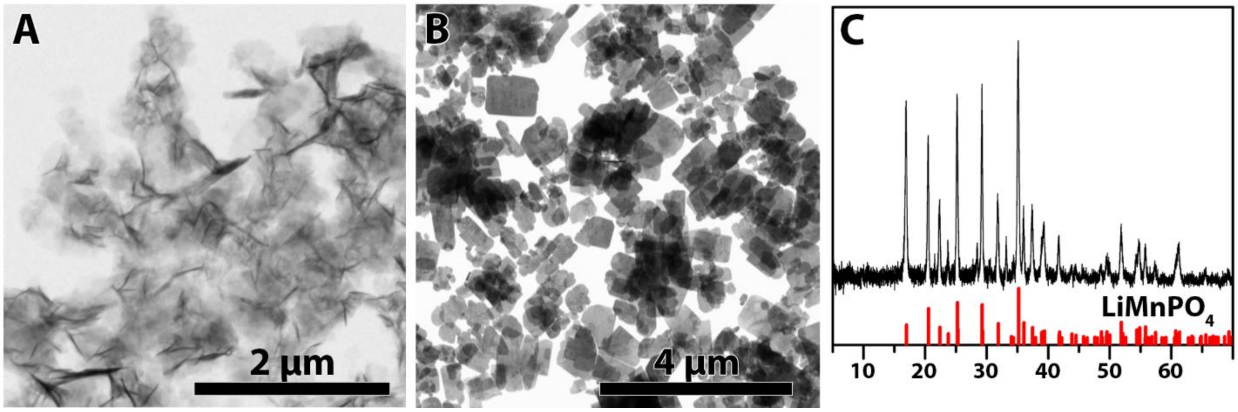

Figure S3.10: A) TEM image of $Mn_3(PO_4)_2 \cdot 3H_2O$ nanoscrolls B) STEM image and C) XRD patterns of $LiMnPO_4$ nanosheets from the reaction of $Mn_3(PO_4)_2 \cdot 3H_2O$ nanoscrolls at 250 °C, 6 h, in DEG:H_2O

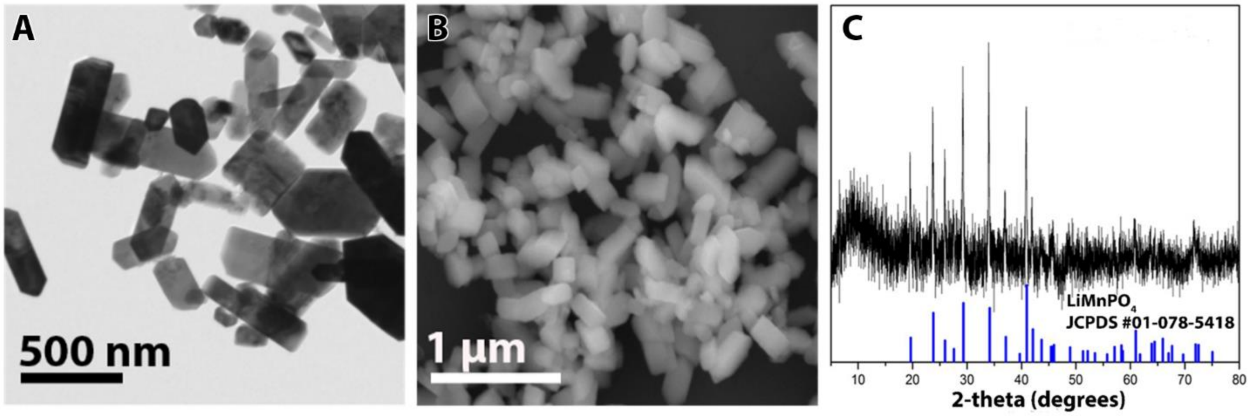

Figure S3.11: A) TEM and B) SEM images and C) XRD diffraction pattern of the hydrothermal reaction of Li_3PO_4 nanoparticles with $Mn_3(PO_4)_2 \cdot 3H_2O$ nanosheets at 250 °C for 4 h.

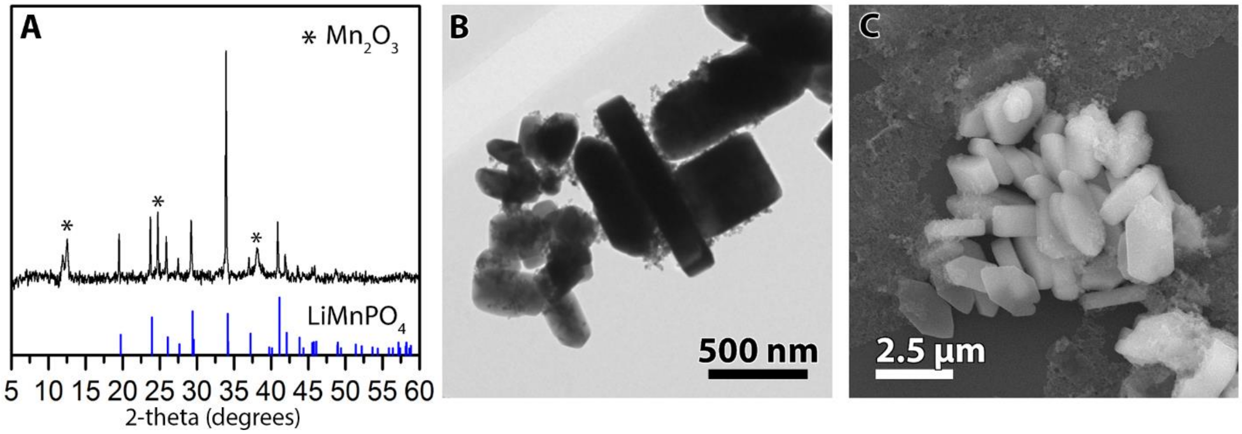

Figure S3.12: A) XRD pattern and B) TEM and C) SEM images of the hydrothermal reaction of Li_3PO_4 nanoparticles with δ-$Mn_3(PO_4)_2$ nanoplates at 250 °C for 4 h.

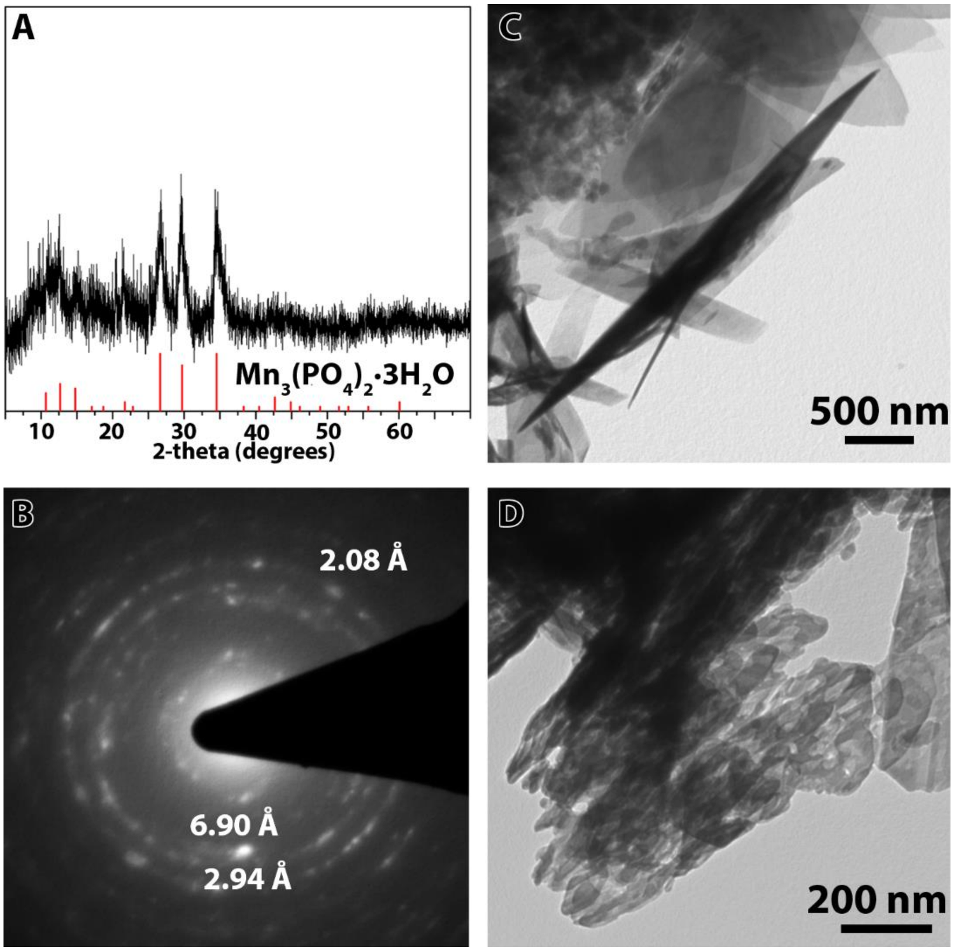

Figure S3.13: Characterization of the product formed by the reaction of $Mn_3(PO_4)_2{\cdot}3H_2O$ with LiCl at 250 °C, 6 h with a 25:5 ratio DEG:H_2O A) Experimental XRD pattern (black) and calculated diffraction pattern for $Mn_3(PO_4)_2{\cdot}3H_2O$. B) SAED pattern matching to the TEM image in D). C) TEM image highlighting the scrolled morphology of the $Mn_3(PO_4)_2{\cdot}3H_2O$ product.

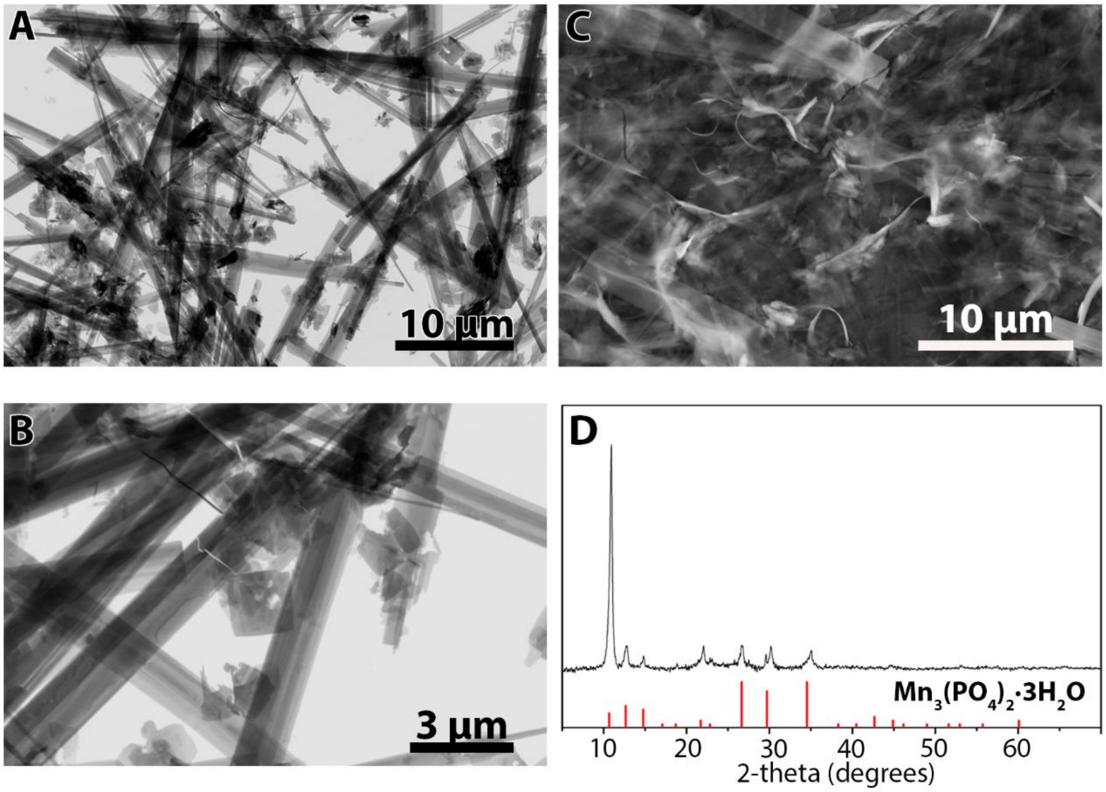

Figure S3.14: Characterization of the reaction of $Mn_3(PO_4)_2 \cdot 3H_2O$ nanosheets at 250 °C in 25:5 DEG:H_2O solvent without LiH_2PO_4. A) zoomed out and B) zoomed in image of belt-like structures. C) SEM image illustrating the bending and scrolling of the. D) XRD pattern of this reaction, corresponding to $Mn_3(PO_4)_2 \cdot 3H_2O$.

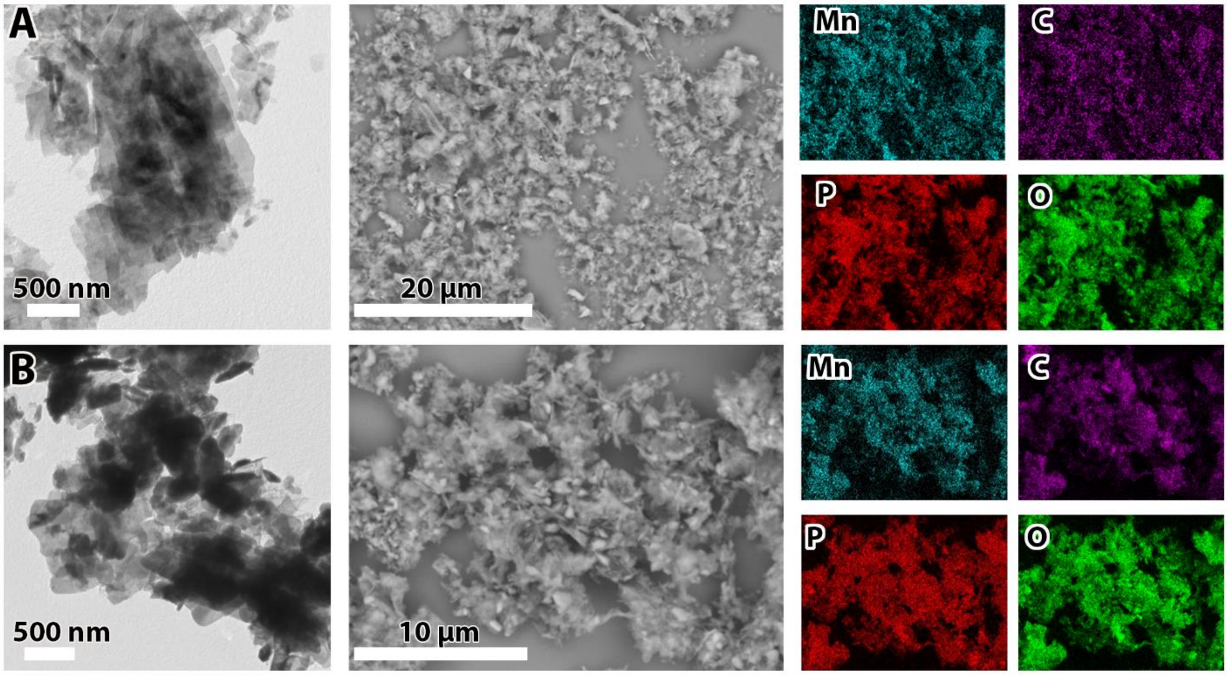

Figure S3.15: Row A) SEM and EDS maps of $LiMnPO_4$ nanosheets after ball-milling. B) $LiMnPO_4$ after ball milling and annealing at 600 °C in an Ar atmosphere for 6 h.

CHAPTER 4

SCROLLING BEHAVIOR OF $Mn_3(PO_4)_2 \cdot 3H_2O$ NANOSHEETS

Neher, G and Salguero, T.T. To be submitted to *Crystal Growth and Design*.

Abstract

$Mn_3(PO_4)_2 \cdot 3H_2O$ nanosheets are easily formed by the reaction of Mn(II) and phosphate precursors under aqueous conditions. Additionally, scrolled up $Mn_3(PO_4)_2 \cdot 3H_2O$ nanosheets were synthesized by carrying out this reaction in a 25:5 ethanol:H_2O solution. The relative amount of $Mn_3(PO_4)_2 \cdot 3H_2O$ nanoscrolls observed was altered by changing the amount of solvent used. Different solvents were also tested—$Mn_3(PO_4)_2 \cdot 3H_2O$ nanoscrolls were observed when polar solvents were used; however, no scrolling was noticed when non-polar solvents were used. Furthermore, raising the pH of the initial $(NH_4)_2HPO_4$ solution resulted in scrolling, suggesting that the HPO_4^{2-} ion also plays an important role in the scrolling mechanism. Finally, scrolling of $Mn_3(PO_4)_2 \cdot 3H_2O$ nanosheets was induced post-synthesis by solvothermally reacting $Mn_3(PO_4)_2 \cdot 3H_2O$ nanosheets at 250 °C in a 25:5 DEG:H_2O solution. The product morphology consisted of nanobelts and nanoscrolls of $Mn_3(PO_4)_2 \cdot 3H_2O$, indicating that the initial $Mn_3(PO_4)_2 \cdot 3H_2O$ nanosheets dissolve and renucleate out as these morphologies.

Introduction

Nanoscrolls represent a unique subclass of morphologies that contain elements of both one and two-dimensional materials. Nanoscrolls are nanosheets that are rolled up, but differ from other similar structures, such as nanotubes and nanowires, and in some instances show better performance as catalysts. Osterloh and coworkers showed that $H_2K_4Nb_6O_{17}$ nanoscrolls exhibit better photocatalytic activity than nanosheets of the same compound, due to a reduced bandgap and larger population of the trapped electrons from the folding of the niobate layers.[1] Two-dimensional compounds that are known to scroll in the literature include metal oxides,[2],[3],[4] layered-double hydroxides (LDHs),[5],[6],[7] and metal fluorides[8].

While there are a fair number of reports on nanoscrolls in the literature, an overall scrolling mechanism is still elusive. Sasaki and coworkers reported the scrolling behavior of 1D nanotubes from 2D nanosheets of TiO_2 and MnO_2 occurs by an ion intercalation-deintercalation mechanism, facilitated by the addition of NaOH.[4] Other reports have looked into the scrolling of LDHs. Du and coworkers reported the scrolling of a CoAl LDH that occurred as a result of the synergistic effect between the high pressure and urea precursor in their hydrothermal synthesis.[7] Additionally, Rui et al observed that the amount of LDH scrolling could be controlled by changing the ratio of ethanol:H_2O, during hydrothermal reactions. The vapor pressure of the different solvents ratios was determined to be the driving force for the scrolling behavior.[6]

Gusarov et al took a more quantitative approach to nanoscrolling and created an energy model for this phenomenon. Their energy model showed that for a 1 x 1 μm^2 thinplate of chrysotile, the change in total energy for the system changes is minimized at approximately 5-15 scrolling layers, and becomes unfavorable at more than 20 layers. Also, when the Young's Modulus (ratio of stress to strain in a material and a measure of elasticity) was increased, the result was a decrease in the interlayer radius of the scroll. With these observations, they concluded that nanoscrolls are formed based on three competing factors: 1) The elastic energy attempts to stabilize the nanoscroll with the lowest stress on the inner layer, 2) the reduction of the surface energy to minimize the surface area, and 3) the tendency for the adhesion energy to increase the interlayer surface area.[9]

$Mn_3(PO_4)_2 \cdot 3H_2O$ nanosheets present an interesting test candidate to study nanoscrolling, because of their ease of synthesis and two-dimensional layered structure. $Mn_3(PO_4)_2 \cdot 3H_2O$ has shown promise in supercapacitor applications,[10] as a water oxidation catalyst,[11] and as a precursor to cathode materials for Li-ion batteries[12]. In this chapter, we explore the parameters that lead to the scrolling of $Mn_3(PO_4)_2 \cdot 3H_2O$ nanosheets.

Experimental

Materials

The following reagents were used as received: $MnSO_4 \cdot H_2O$ (J.T. Baker 99%), $(NH_4)_2HPO_4$ (Sigma-Aldrich, ≥98%), Diethylene Glycol (Sigma Aldrich, 99%), Ethylene Glycol (Sigma Aldrich ≥ 99%), $MnCl_2 \cdot 6H_2O$ (Sigma Aldrich, 99-102%) $Mn(CH_3COO)_2 \cdot 4H_2O$ (Aldrich ≥ 99%)

Solvent Studies

0.5000 g (2.040 mmol) of $Mn(CH_3COO)_2 \cdot 4H_2O$ was completely dissolved in approximately 2.5 ml of H_2O and 22.5 ml of solvent. In a separate beaker, 0.1790 g (1.36 mmol) of $(NH_4)_2HPO_4$ was dissolved in 2.5 ml of water. The $(NH_4)_2HPO_4$ was solution was then added to the $Mn(CH_3COO)_2 \cdot 4H_2O$ solution and stirred for 30 minutes. The resulting suspension was then centrifuged 3x at 10,000 RPM and washed with 30 ml nanopure water 3x times, and finally redispersed in water for analysis.

pH Studies

For the pH studies, $Mn(CH_3COO)_2 \cdot 4H_2O$ was dissolved in 15 ml of H_2O. $(NH_4)_2HPO_4$ was dissolved in a separate 15 ml solution of water. The pH of the $(NH_4)_2HPO_4$ solution was adjusted to the desired level with the addition of 1M NaOH. Afterwards, the $(NH_4)_2HPO_4$ solution was added to the $Mn(CH_3COO)_2 \cdot 4H_2O$ solution, at which point a milky white precipitate immediately formed. The suspension was stirred for 30 min, centrifuged at 10,000 RPM, and washed with 30 ml nanopure water 3x. The resulting product could either be dried at 120 °C to form a powder or kept as a suspension in H_2O.

Characterization

Powder X-ray Diffraction (PXRD) data were collected on a PANalytical X'Pert utilizing a Cu Kα X-ray source ($\lambda = 1.78890$) operated at 40 kV and 40 mA. Diffraction data was collected from 5-70 2θ with a scan rate of 0.1 s/step. Samples were prepared as powder mounts or drop cast from solution.

Transmission Electron Microscopy (TEM) imaging and Selected Area Electron Diffraction (SAED) analyses were performed on a Tecnai 20 transmission electron microscope with an accelerating voltage of 200 kV. Samples were drop cast onto formvar grids and air dried.

Scanning Electron Microscopy (SEM) analysis was performed on a FEI Teneo FE-SEM at 10 kV with a spot size of 10. Samples were dropcast onto a silicon wafer.

For Atomic Force Microscopy (AFM), samples were dispersed in water, bath sonicated and drop cast onto a clean Si wafer. Data were collected with a Bruker Innova instrument in tapping mode. AFM data were analyzed with Nanoscope Analysis software.

IR spectra were collected on a Bruker Tensor 37 spectrometer in scanning mode from 500-4,000 cm^{-1}.

Results and Discussion:

$Mn_3(PO_4)_2 \cdot 3H_2O$ nanosheets are formed by a facile precipitation reaction by mixing a solution containing a Mn^{2+} cation and a solution containing HPO_4^{2-} or $H_2PO_4^{1-}$. Upon mixing these two solutions, a white $Mn_3(PO_4)_2 \cdot 3H_2O$ precipitate is formed. TEM and AFM analysis in chapters II and III reveal the two-dimensional morphology of this compound. This result is unique—nanosheets are typically synthesized through bottom-up hydrothermal methods involving a capping agent and high temperatures >180 °C. The capping agent is usually an organic compound that binds to the surface during nucleation, contributing to the directional growth of the compound.[13] Because no capping agent is used in this reaction, a closer look at the crystal structure of this compound is required in order to understand this distinctive two-dimensional growth.

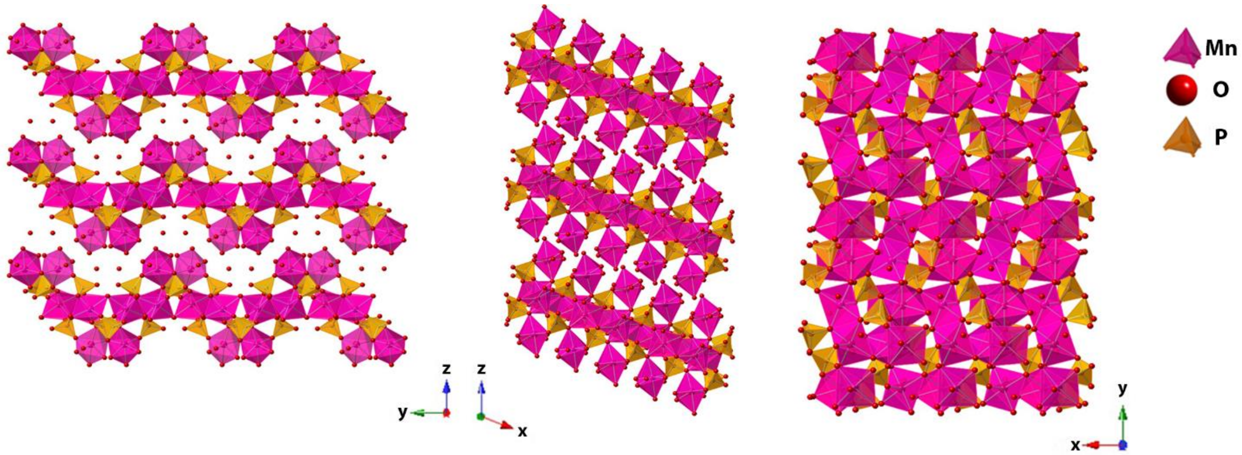

Figure 4.1: Crystal structure of $Mn_3(PO_4)_2 \cdot 7H_2O$ showing the (200), (020), and (002) planes.

Currently, the crystal structure of $Mn_3(PO_4)_2 \cdot 3H_2O$ has never been experimentally determined, however, the crystal structure of $Mn_3(PO_4)_2 \cdot 7H_2O$ is known and presented in figure 4.1. This structure is composed of planes of $[MnO_5]$ and $[MnO_6]$, edge and corner-shared to $[PO_4]$ tetrahedra. These planes extend along the x and y directions, and are separated by hydrogen-bound water molecules. The crystal structures of $Mn_3(PO_4)_2 \cdot 7H_2O$ and $Mn_3(PO_4)_2 \cdot 3H_2O$ differ slightly in unit cell parameters and hydrate environments. Nam et al used density functional theory (DFT) measurements to calculate the structure of $Mn_3(PO_4)_2 \cdot 3H_2O$, and discovered that the water molecules are found bridging two Mn atoms, coordinated to Mn, and found without any bonds between the layers.[11] The stronger and more stable in-plane covalent bonds compared to the weaker out-of-plane hydrogen bonds are the driving force for the two-dimensional growth of $Mn_3(PO_4)_2 \cdot 3H_2O$.

This growth, from the initial reaction to 7 d, was monitored by XRD and TEM. Aliquots were taken from this reaction at different time intervals and washed with H_2O. Figure 4.2 shows the XRD pattern and TEM images from each time point in this study. The XRD pattern of each matches to the experimental pattern for $Mn_3(PO_4)_2 \cdot 3H_2O$, and confirms that this compound precipitates after initial mixing of the precursor solutions. During the course of 7 d, the (002) peak in the XRD pattern becomes more prominent, indicating the increase in crystallinity of this plane. TEM images reveal that the nanosheet morphology does not change until 7 d. At this time, thicker nanosheets with rounded edges are observed. This small change in morphology is accounted for by the dissolution of the more reactive edges of the nanosheets over the course of 7 d.

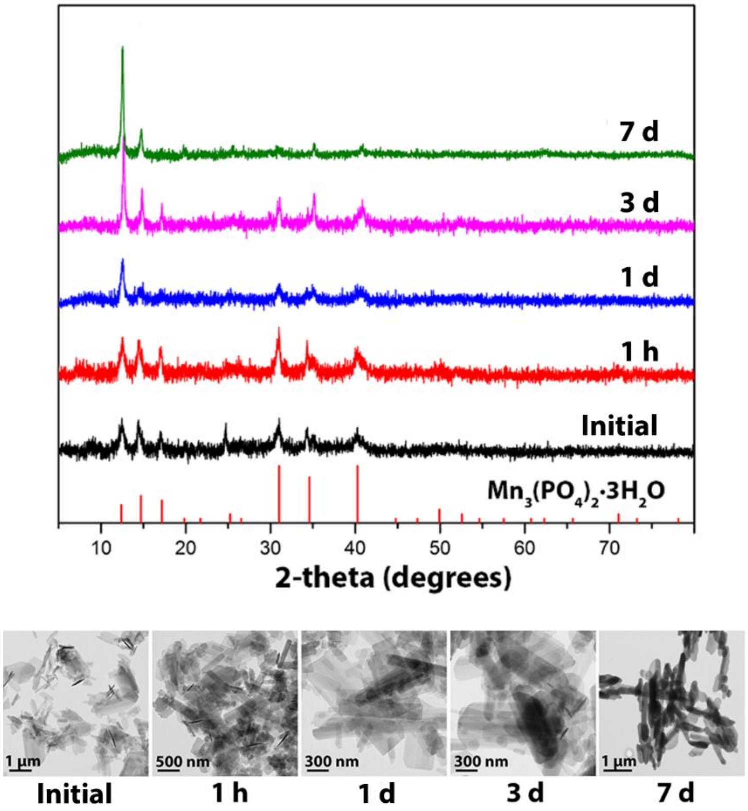

Figure 4.2: Time study of $Mn_3(PO_4)_2 \cdot 3H_2O$ formation monitored with XRD and TEM. Aliquots were taken up at each time point, centrifuged, and analyzed.

Both the ease of synthesis and sheet-like morphology of $Mn_3(PO_4)_2 \cdot 3H_2O$ make it an ideal test candidate for nanoscrolling experiments. We were successful in forming nanosheets by adding ethanol or other polar solvents to the precursor reaction mixture. During a typical experiment, $(NH_4)_2HPO_4$ and $Mn(CH_3COO)_2 \cdot 4H_2O$ were first dissolved in separate beakers with water. Next, ethanol was added to the $Mn(CH_3COO)_2 \cdot 4H_2O$ solution and adjusted to give a 25:5 EtOH:H_2O ratio for the total solution. Finally, the $(NH_4)_2HPO_4$ solution was added to the $Mn(CH_3COO)_2 \cdot 4H_2O$ EtOH:H_2O solution. Just as in the synthesis of $Mn_3(PO_4)_2 \cdot 3H_2O$ nanosheets, a solid white $Mn_3(PO_4)_2 \cdot 3H_2O$ product was formed immediately. However, observing the precipitate with TEM shows that many of the nanosheets were scrolled (Figure 4.3C). A comparison of $Mn_3(PO_4)_2 \cdot 3H_2O$ nanosheets and nanoscrolls is shown in Figure 4.3. For both morphologies, the XRD pattern in 4.3A shows a strong match to the calculated pattern of $Mn_3(PO_4)_2{\cdot}3H_2O$. However, the $Mn_3(PO_4)_2{\cdot}3H_2O$ nanosheets exhibit a more intense peak (002), than the nanoscrolls. This difference is explained by the different morphologies. The nanosheets (figure 4.3B), with length and width in hundreds of nanometers, and thickness in 10-25 nm, primarily exhibit the (002) face. The nanoscrolls (figure 4.3C) on the contrary, display multiple crystallographic planes, and thus do not display an orientation effect. This is further illustrated by the SAED patterns of each figure. For the nanosheets, single crystalline electron diffraction was obtained (figure 4.3D), while for the scrolls, only a polycrystalline ring pattern was observed (figure 4.3E). Attempts were carried out to obtain HRTEM on the scrolls. Unfortunately, the $Mn_3(PO_4)_2{\cdot}3H_2O$ nanosheets broke down under these beam conditions. Finally, IR spectroscopy was carried out on both nanoscrolls and nanosheets, however, no significant difference in the spectra was observed (figure S4.1).

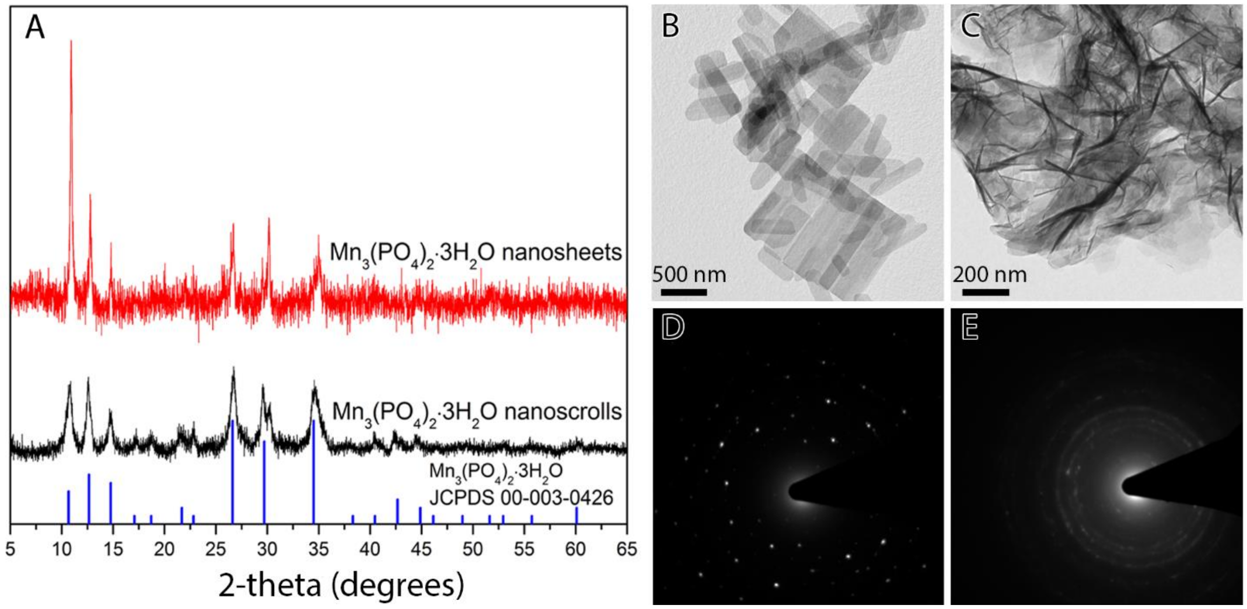

Figure 4.3: Comparison of $Mn_3(PO_4)_2{\cdot}3H_2O$ nanosheets and nanoscrolls. A) XRD patterns for both nanoscrolls and nanosheets. B) TEM image of $Mn_3(PO_4)_2{\cdot}3H_2O$ nanosheets C) nanoscrolls. Elecron diffraction pattern for D) $Mn_3(PO_4)_2{\cdot}3H_2O$ nanosheets and E) nanoscrolls.

Low kV STEM images of the $Mn_3(PO_4)_2\cdot 3H_2O$ nanoscrolls were taken with different detectors as shown in figure S4.2. The secondary electron detector and mix of stem detectors highlight the three-dimensionality of the scrolls. The EDS maps show an even distribution of O, P, and Mn present in the scrolls.

The nanoscrolls were also thermally stable when dried—drying $Mn_3(PO_4)_2\cdot 3H_2O$ at 120°C and redispersing in H_2O preserved the morphology of the $Mn_3(PO_4)_2\cdot 3H_2O$ nanosheets as shown in the TEM images in figure S4.3.

Additionally, the TEM images of the nanoscrolls show that the scrolling is not 100%—there are still clear instances of unscrolled $Mn_3(PO_4)_2\cdot 3H_2O$ nanosheets. However, we found that the ratio of solvent to water in the reaction impacted the amount of relative scrolling observed. For example, a higher percentage of scrolls was observed as the ratio of ethanol to water increased, as shown in the representative TEM images in Figure 4.4. Below a ratio of 15:15 EtOH:H_2O, scrolling was rare, while above this ratio, scrolling became more common. Due to the limited solubility of the $(NH_4)_2PO_4$ precursor in ethanol, a completely anyhdrous reaction could not be carried out.

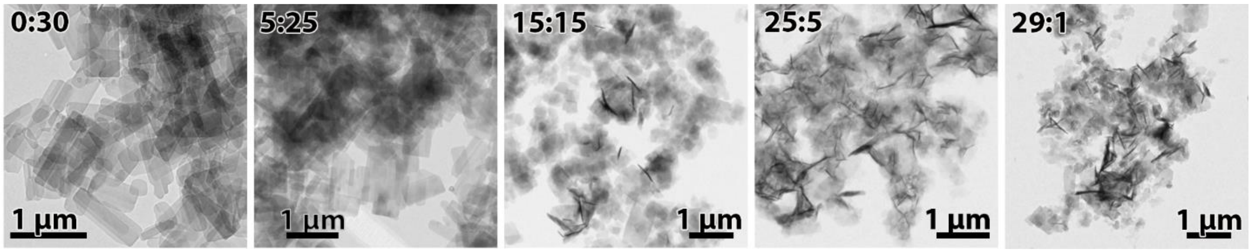

Figure 4.4: TEM images of the $Mn_3(PO_4)_2\cdot 3H_2O$ product when different ratios of H_2O:EtOH were used in the reaction.

Changing the Mn precursor and carrying out the reaction with a 25:5 ratio of EtOH:H_2O also resulted in scrolling, as shown in the TEM images in figure S4.4. Both $MnCl_2{\cdot}4H_2O$ and $Mn(NO_3)_2{\cdot}4H_2O$ salts lead to the same amount of scrolling. The scrolls synthesized with $Mn(NO_3)_2{\cdot}4H_2O$ are slightly larger in size than those produced by $MnCl_2{\cdot}4H_2O$, however $Mn(NO_3)_2{\cdot}4H_2O$ also produces noticeably larger nanosheets than nanosheets made from $MnCl_2{\cdot}4H_2O$ or Mn(acetate)$_2{\cdot}4H_2O$ in reactions in which H_2O is the sole solvent.

Scrolling experiments were also carried out with different solvents. Each reaction was carried out with a total of 5 ml of H_2O and 25 ml of solvent. The list of solvents tested is shown in table 4.1, along with each solvent's dielectric constant and the relative amount of scrolling observed. The TEM images of the resulting morphologies are shown in figure S4.5.

Table 4.1

Solvent	**Dielectric**	**Scrolls observed**
Methanol	32.6	Few
Ethanol	24.6	Many
Propanol	20.1	Few
Isopropanol	18.3	Few
Butanol	17.8	Few
Pentanol	13.9	Few
DMSO	47.0	Few
DEG	31.8	None
NVP	32.5	Many
Urea	2.9	none
EG	37.7	Many
pentane	1.8	None
hexane	1.9	None
Water	78.5	None

Notably, all alcohols tested lead to nanoscrolls. Furthermore, no scrolling was observed when pentane, hexane, diethylene glycol (DEG) and urea were used as the solvent. The most amount of scrolls were observed when ethanol, ethylene glycol (EG), N-vinyl pyrrolidone (NVP), and dimethyl sulfoxide (DMSO) were used as solvents. This study suggest that the polarity plays a role in the scrolling behavior. One measure of the polarity of a compound is its dielectric constant. Solvents with dielectric constants greater than 13 all formed $Mn_3(PO_4)_2{\cdot}3H_2O$ nanoscrolls, with the exception of DEG and H_2O. Consequently, solvents with low dielectric constants and therefore low polarity-hexane, pentane and urea-did not result in nanoscrolls. DEG is an interesting case, as it has a high dielectric constant and is similar in structure to EG, yet does not result in scrolling. However, DEG is known to be a strong chelator to metal phosphate compounds, and may stabilize the surface of $Mn_3(PO_4)_2{\cdot}3H_2O$.[14] Finally, even though H_2O has the highest dielectric constant tested, the hydrated $Mn_3(PO_4)_2{\cdot}3H_2O$ structure requires water to form, which is a possible reason why it may not form nanoscrolls.

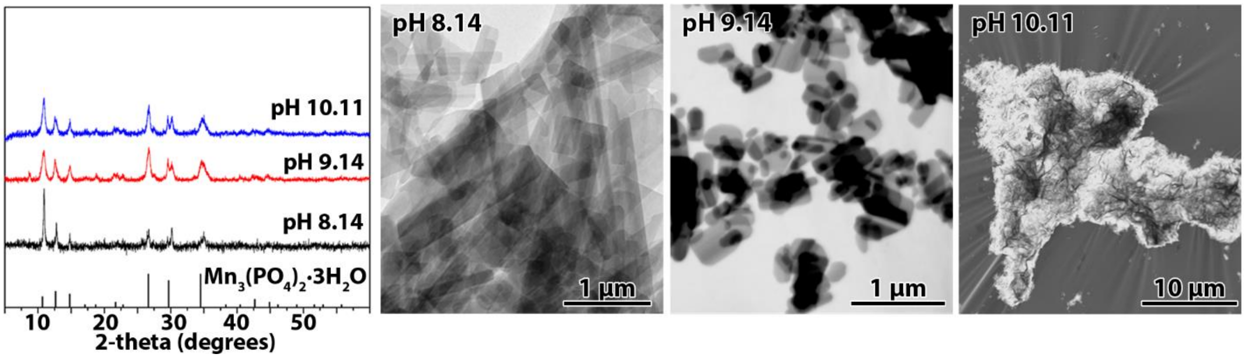

Figure 4.5: XRD pattern and TEM images of $Mn_3(PO_4)_2{\cdot}3H_2O$ formed by changing the pH of the $(NH_4)_2HPO_4$ with NaOH.

Raising the pH of the precursor $(NH_4)_2HPO_4$ solution also resulted in $Mn_3(PO_4)_2{\cdot}3H_2O$ nanoscrolls. In this study, the pH of the $(NH_4)_2HPO_4$ solution was adjusted with NaOH, and then reacted with an aqueous solution of $Mn(CH_3COO)_2{\cdot}3H_2O$. Figure 4.5 shows the XRD pattern and TEM images of the products of this reaction when different pH levels of the $(NH_4)_2HPO_4$ solution were used. The pH of the $(NH_4)_2HPO_4$ solution without adding NaOH is 8.14. No change in morphology was noticed at a pH of 9.14. However, when the reaction was changed to 10.11 pH, bundles of $Mn_3(PO_4)_2{\cdot}3H_2O$ nanoscrolls were observed, suggesting that the pH of the starting solutions also play a large role in the observed morphology.

We next investigated the effect of ionic strength on the formation of $Mn_3(PO_4)_2{\cdot}3H_2O$ nanosheets. We hypothesized that the ionic strength of the solutions would disrupt the electrostatic interactions of individual $Mn_3(PO_4)_2{\cdot}3H_2O$ nanosheets. To test this theory, 1.5 M LiCl solutions were prepared and added to the $Mn(CH_3COO)_2{\cdot}4H_2O$ precursor solution either before or after reaction with $(NH_4)_2HPO_4$. In these reactions, water was the only solvent. Figure S4.6 shows the TEM images of the resulting product. In each case, no scrolling was observed, eliminating electrostatic repulsions as a possible scrolling mechanism.

$Mn_3(PO_4)_2{\cdot}3H_2O$ nanoscrolls mentioned previously resulted from changing the pH or solvent of the precursor solution. We attempted to induce scrolling of $Mn_3(PO_4)_2{\cdot}3H_2O$ post synthesis with a few experiments. Figure S4.7 shows the TEM images of the $Mn_3(PO_4)_2{\cdot}3H_2O$ product of these attempts. Drying $Mn_3(PO_4)_2{\cdot}3H_2O$ nanosheets at 120 °C did not result in nanosheets, nor did heating the suspension at 80 °C. Also, treating a colloidal suspension of $Mn_3(PO_4)_2{\cdot}3H_2O$ nanosheets with EtOH did not result in nanoscrolling.

However, we were able to induce scrolling of $Mn_3(PO_4)_2{\cdot}3H_2O$ in one instance. In this experiment, $Mn_3(PO_4)_2{\cdot}3H_2O$ nanosheets were hydrothermally reacted at 250 °C for 6 h, in a solvent ratio 25:5 DEG:H_2O. The resulting $Mn_3(PO_4)_2{\cdot}3H_2O$ product is shown in the TEM and SEM image of 4.6A and 4.6B, respectively. The TEM image reveals nanobelts of

$Mn_3(PO_4)_2{\cdot}3H_2O$, tens of microns in length and <2 μm in width. In some instances, these belts are also twisted. Among these belts are smaller $Mn_3(PO_4)_2{\cdot}3H_2O$ structures. The SEM image in figure 4.6B shows large-scrolled structures, as well as the nanobelts. These findings are extremely interesting. The difference in morphology between the starting $Mn_3(PO_4)_2{\cdot}3H_2O$ nanosheets and the $Mn_3(PO_4)_2{\cdot}3H_2O$ nanobelt/scrolls product suggest that the initial $Mn_3(PO_4)_2{\cdot}3H_2O$ nanosheets dissolve, and then renucleate as twisted $Mn_3(PO_4)_2{\cdot}3H_2O$ nanobelts and nanoscrolls. Remarkably, this phenomenon occured in DEG, which did not result in scrolling when added to the precursor solutions in the solvent study. However, this reaction occurs above the boiling point of DEG (244 °C) which may provide a different nucleation environment than DEG at room temperature.

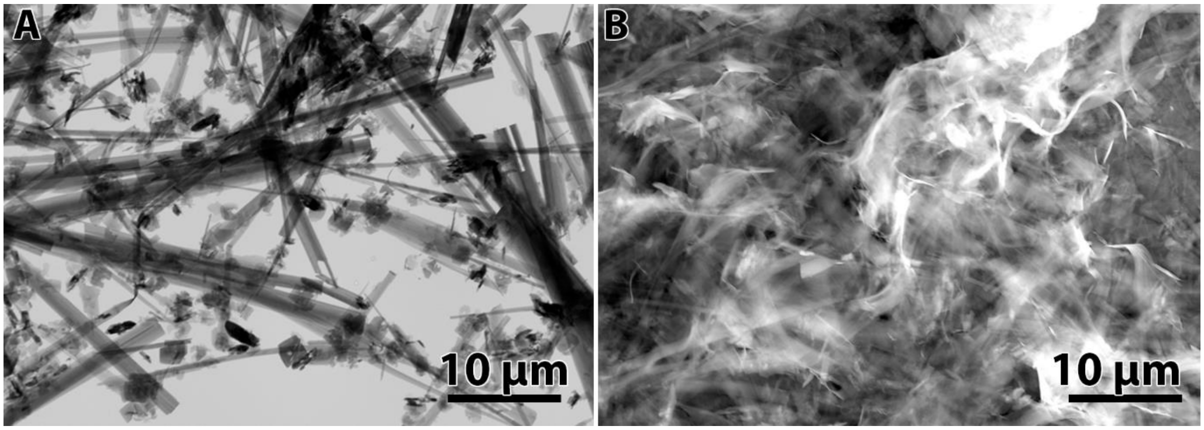

Figure 4.6: TEM (A) and SEM (B) images of the nanoscrolls of $Mn_3(PO_4)_2{\cdot}3H_2O$ formed by the hydrothermal reaction of $Mn_3(PO_4)_2{\cdot}3H_2O$ nanosheets at 250 °C for 6 h.

Based on this data, there are several different scrolling mechanisms that are possible in this system. Similar nanoscrolls were obtained in Ren et al with double layered-hydroxides.[6] In this report, increasing the ethanol to water ratio resulted in a higher degree of scrolling of the double-layered hydroxides. This observation was explained with Raoult's laws of partial pressures. The higher pressure experienced by the system as a result of adding a higher fraction of ethanol was thought to be responsible for the greater degree of scrolling. This was hypothesized to reduce the electrostatic interaction between the brucite sheet and interlayer CO_3^{2-}. In our experiments, $Mn_3(PO_4)_23H_2O$ scroll formation was observed in the presence of greater molar amounts of ethanol, but it does not explain why hexane, with a higher vapor pressure than ethanol, does not result in scrolling.

Also, Al and Co-doped NiOH in a ratio of 8:2:1 Ni:Al:Co resulted in 'dandelion' morphologies, or clusters of scrolls similar to what we observed.[15] This was attributed to the change in force of the cation and anions of the brucite-like NiOH. The structure of $Mn_3(PO_4)_2{\cdot}3H_2O$ is similar to the structure of LDHs, however, there is no charge separated positive and negative layer.

Hydrogen bonding of the polar solvents may have an impact on the scrolling of $Mn_3(PO_4)_2{\cdot}3H_2O$. It is possible that the polar solvents hydrogen bond with the O of the Mn and P polyhedra. This hydrogen bonding may result in distortion of the Mn and P polyhedra, causing it to adopt a morphology that is more thermodynamically favorable during nucleation and crystal growth. Schaak et al observed scrolling in TBA-exfoliated $H_2SrTa_2O_7$ and $H_2SrTa_2O_7$ compounds, and determined that the distortions of the MO_6 octahedra was a possible mechanism.[16]

The scrolling observed when the pH of the $(NH_4)_2HPO_4$ was raised to 10.11 may result from the different species of phosphate anion present. The starting pH of the $(NH_4)_2HPO_4$ solution is approximately 8.14, and according to the equilibrium values of phosphate species at different pH, this solution should contain 50% $H_2PO_4^-$ and 50% HPO_4^{2-} ions.[17] However, at a pH of 10, the $(NH_4)_2PO_4$ solution contains almost 100% HPO_4^{2-} ions. This chemical species may facilitate scrolling during the nucleation process by electrostatically interacting with the Mn and phosphate polyhedra.

Finally, the fact that we were not able to induce scrolling of $Mn_3(PO_4)_2{\cdot}3H_2O$ nanosheets by non-hydrothermal methods show the remarkable stability of the nanosheets. The hydrothermal reaction that did lead to scrolling suggests that the scrolling process occurs during the dissolution and renucleaction of the $Mn_3(PO_4)_2{\cdot}3H_2O$ nanosheets at high pressures and temperatures.

Conclusion

In this chapter, I demonstrated several viable ways to form $Mn_3(PO_4)_2{\cdot}3H_2O$ nanoscrolls. Nanoscrolling was achieved by using polar solvents with the reaction precursor and by changing the pH of the $(NH_4)_2HPO_4$ precursor solution. Furthermore, $Mn_3(PO_4)_2{\cdot}3H_2O$ was formed post-synthesis by solvothermally treating the precursor $Mn_3(PO_4)_2{\cdot}3H_2O$ nanosheets at 250 °C in H_2O. This same chemistry may be useful in forming scrolls of other two-dimensional layered metal phosphate compounds, such as NH_4MPO_4 (M = Mn, Fe, Ni, Co), and $M_3(PO_4)_2{\cdot}8H_2O$ (M = Ni, Co).

References:

[1] M. C. Sarahan, E. C. Carroll, M. Allen, D. S. Larsen, N. D. Browning and F. E. Osterloh, *Journal of Solid State Chemistry* **2008**, *181*, 1678-1683.

[2] Y. Zheng, N. Guo, Y. Jia, H. Qiao and H. You, *CrystEngComm* **2012**, *14*, 7195-7200.

[3] L. Shi, Y. Xu and Q. Li, *Crystal Growth & Design* **2008**, *8*, 3521-3525.

[4] R. Ma, Y. Bando and T. Sasaki, *The Journal of Physical Chemistry B* **2004**, *108*, 2115-2119.

[5] T. Posati, F. Costantino, L. Latterini, M. Nocchetti, M. Paolantoni and L. Tarpani, *Inorganic Chemistry* **2012**, *51*, 13229-13236.

[6] L. Ren, J.-S. Hu, L.-J. Wan and C.-L. Bai, *Materials Research Bulletin* **2007**, *42*, 571-575.

[7] W. Lv, M. Du, W. Ye and Q. Zheng, *Journal of Materials Chemistry A* **2015**, *3*, 23395-23402.

[8] R. Ramachandran, D. Johnson-McDaniel and T. T. Salguero, *Chemistry of Materials* **2016**, *28*, 7257-7267.

[9] A. A. Krasilin and V. V. Gusarov, *Russian Journal of General Chemistry* **2015**, *85*, 2238-2241.

[10] C. Yang, L. Dong, Z. Chen and H. Lu, *The Journal of Physical Chemistry C* **2014**, *118*, 18884-18891.

[11] K. Jin, J. Park, J. Lee, K. D. Yang, G. K. Pradhan, U. Sim, D. J. Jeong, H. L., S. Park, D. Kim, N. E. Sung, S. H. Kim, S. Han and K. T. Nam, *J Am Chem Soc* **2014**, *136*, 7435-7443.

[12] K. Wu, G. Hu, Z. Peng, Z. Zhang, Y. Cao and K. Du, *RSC Advances* **2015**, *5*, 95020-95027.

[13] C. Tan, X. Cao, X. J. Wu, Q. He, J. Yang, X. Zhang, J. Chen, W. Zhao, S. Han, G. H. Nam, M. Sindoro and H. Zhang, *Chem Rev* **2017**, *117*, 6225-6331.

[14] V. Aravindan, J. Gnanaraj, Y.-S. Lee and S. Madhavi, *Journal of Materials Chemistry A* **2013**, *1*, 3518.

[15] J. Xue, W. Ren, M. Wang and H. Cui, *Journal of Nanoparticle Research* **2014**, *16*, 2765.

[16] R. E. Schaak and T. E. Mallouk, *Chemistry of Materials* **2000**, *12*, 3427-3434.

[17] Y. Yang, Q. Wu, M. Wang, J. Long, Z. Mao and X. Chen, *Crystal Growth & Design* **2014**, *14*, 4864-4871.

Supporting information

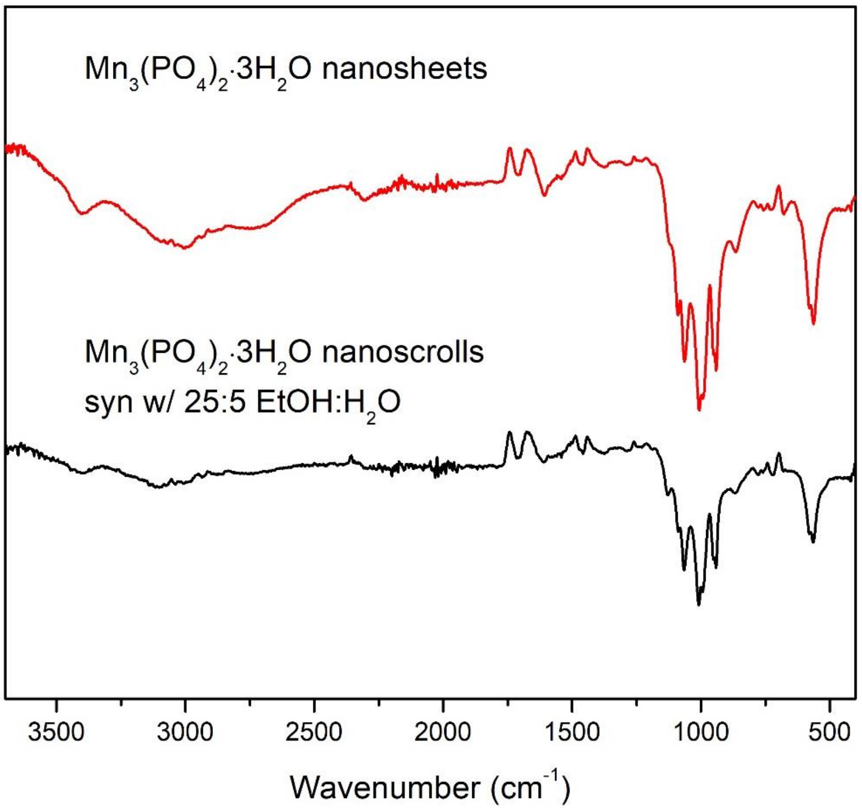

Figure S4.1: IR spectra of $Mn_3(PO_4)_2{\cdot}3H_2O$ nanosheets and $Mn_3(PO_4)_2{\cdot}3H_2O$ nanscrolls. Both spectra exhibit similar vibrational stretches.

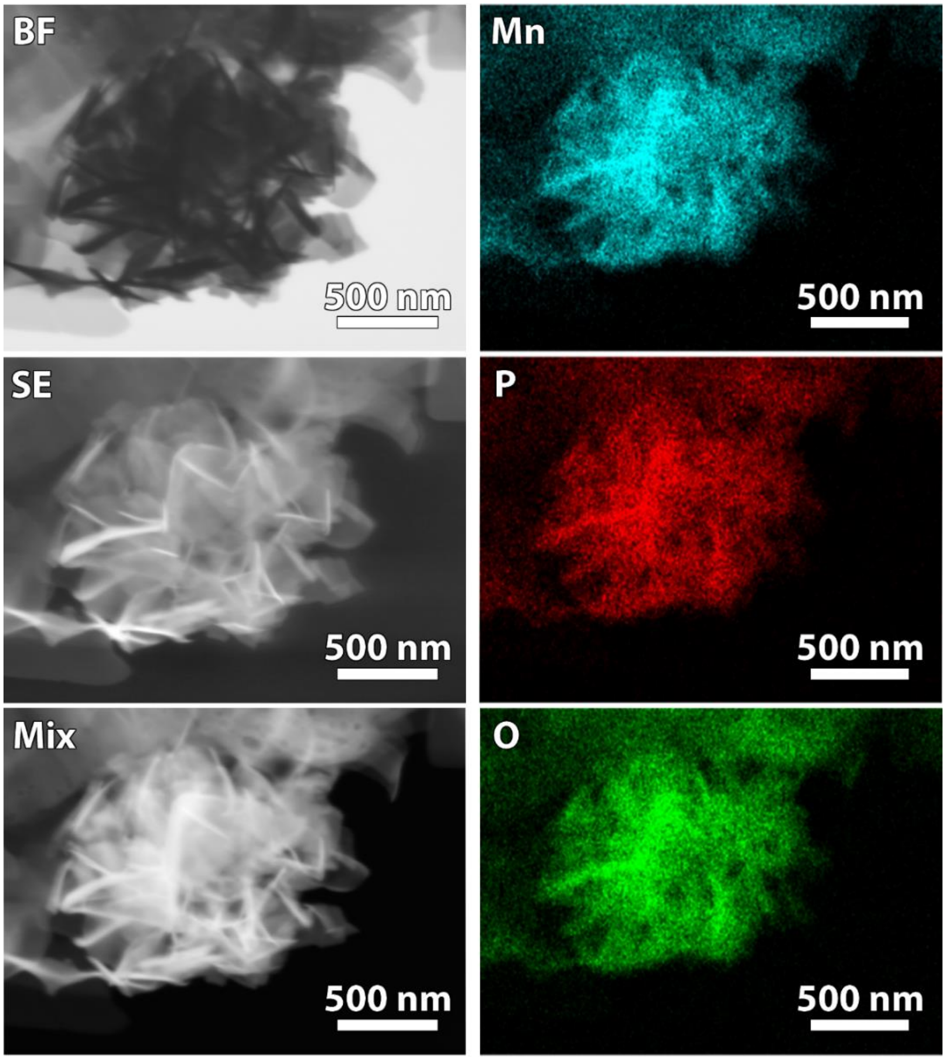

Figure S4.2: Low kV STEM images of $Mn_3(PO_4)_2 \cdot 3H_2O$ nanoscrolls taken with bright field (BF) detector, secondary electron (SE) detector, and mix of detectors. EDS mapping for Mn, P, and O.

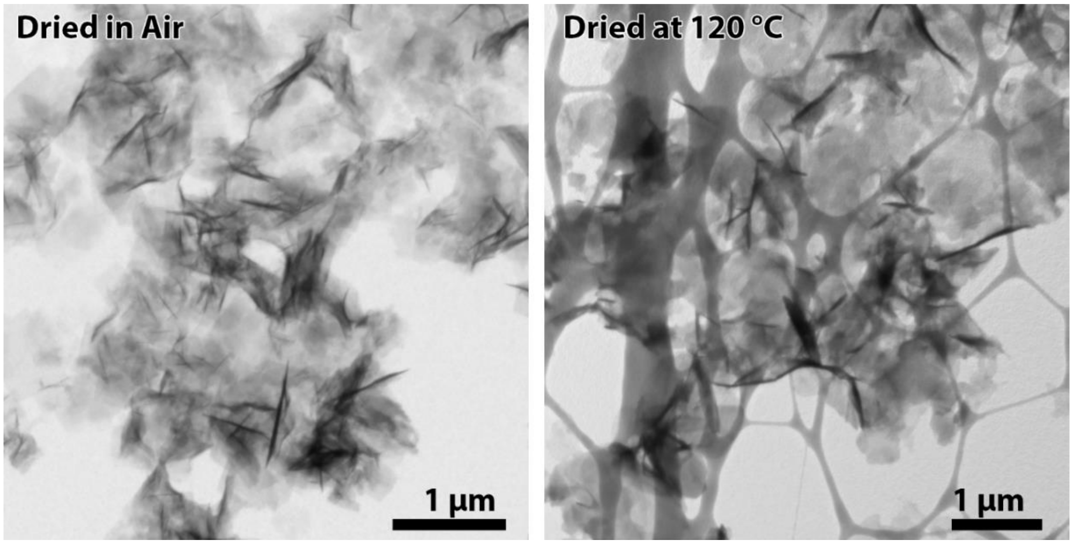

Figure S4.3: TEM images of $Mn_3(PO_4)_2 \cdot 3H_2O$ nanoscrolls after drying in air (left) and drying at 120 °C for 6 h and redispersing in H_2O (right).

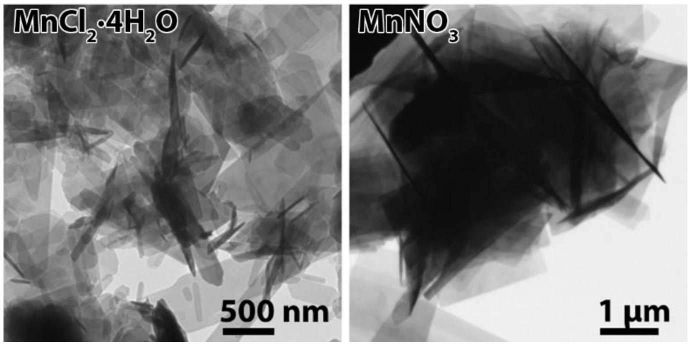

Figure S4.4: TEM images of different manganese salts reacted with a solution ratio of 25:5 ethanol to water. Both precursors resulted in scrolling.

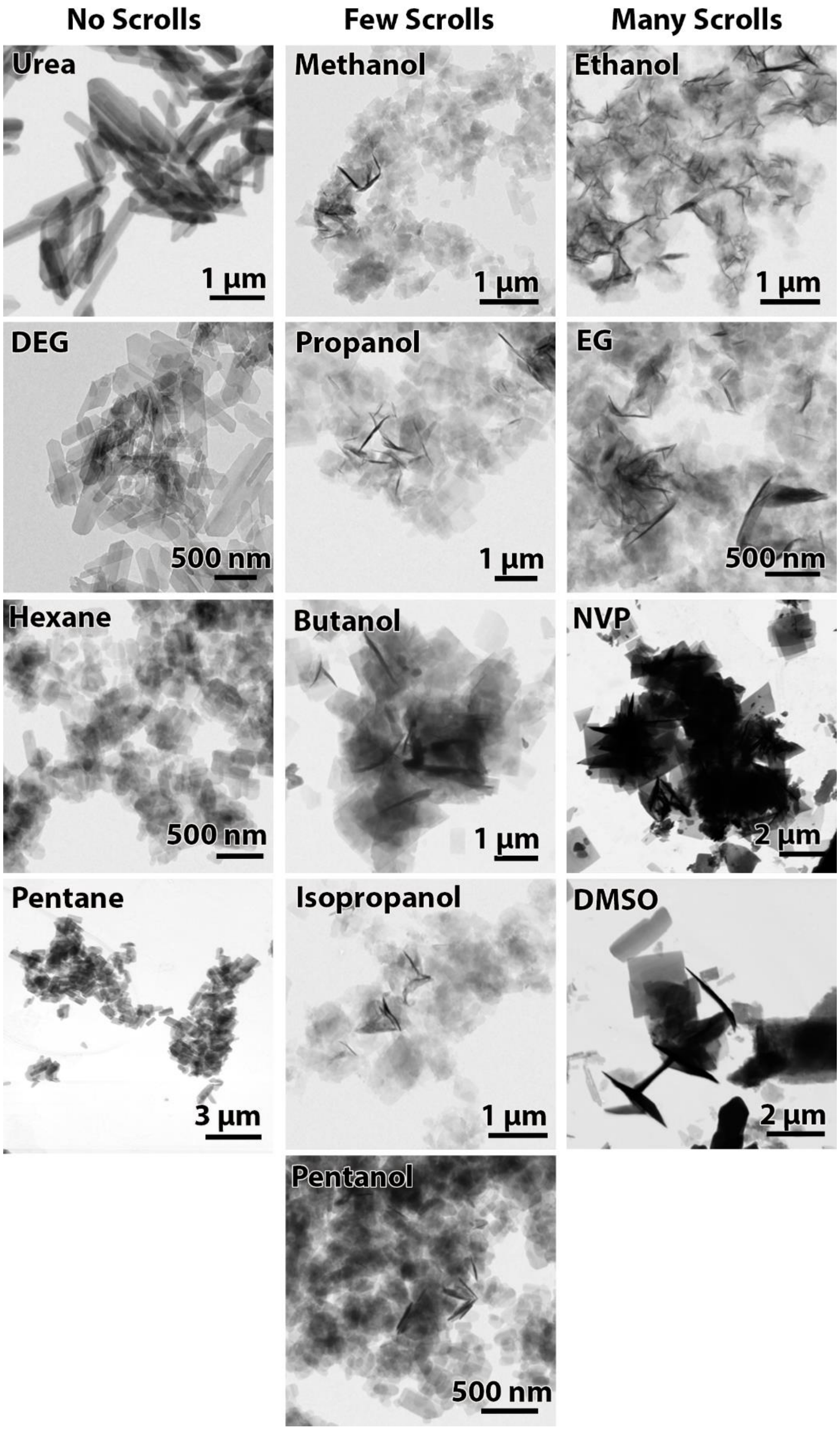

Figure S4.5: TEM images of the $Mn_3(PO_4)_2{\cdot}3H_2O$ morphology formed when using different solvents in a 25:5 solvent:H_2O ratio in the reaction.

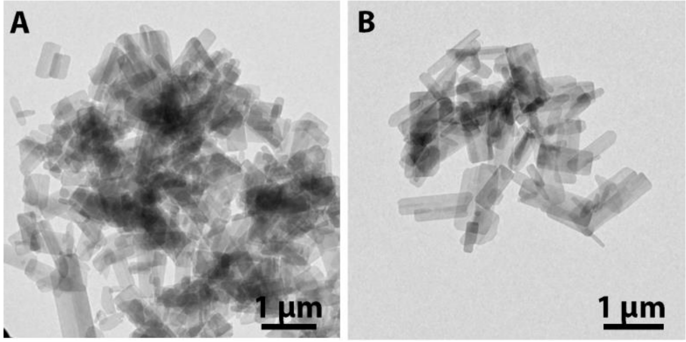

Figure S4.6: TEM images of the $Mn_3(PO_4)_2 \cdot 3H_2O$ product when adding LiCl to the precursor solution (A) and adding LiCl to $Mn_3(PO_4)_2 \cdot 3H_2O$ suspension post synthesis (B).

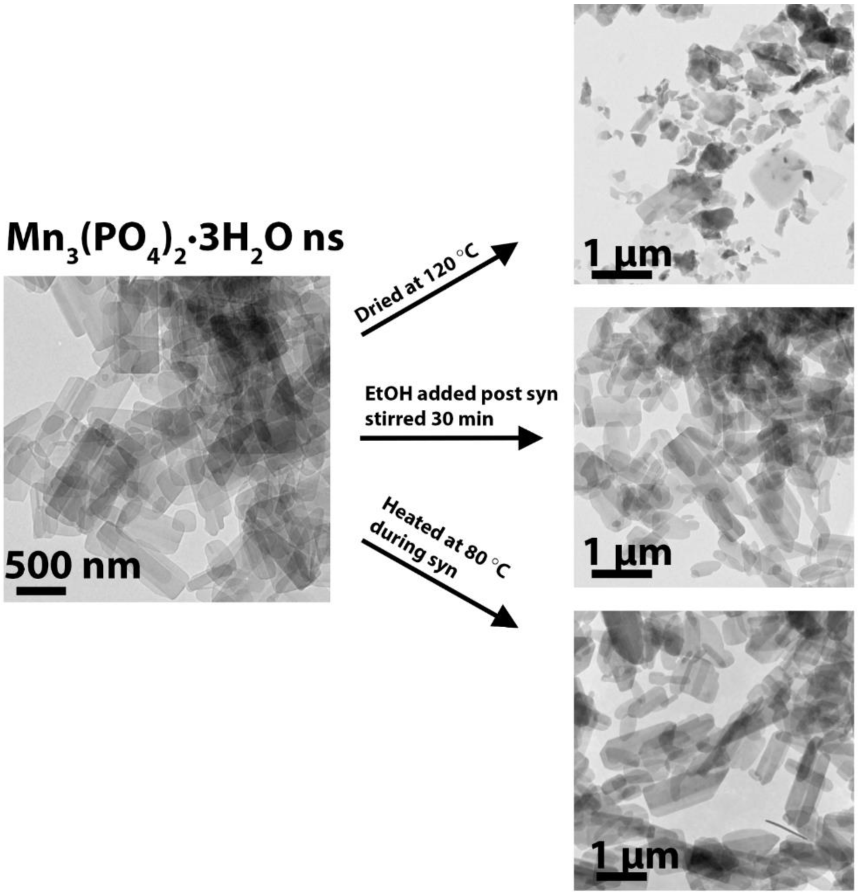

Figure S4.7: TEM images of noteable reactions that did not result in $Mn_3(PO_4)_2{\cdot}3H_2O$ scrolling.

CHAPTER 5

CONCLUSIONS AND FUTURE OUTLOOK

In chapter II, I demonstrated the successful synthesis and characterization of a novel polymorph of $Mn_3(PO_4)_2$—the δ-phase. This structure is composed of [MnO_5] pentahedra, edge- and corner-shared to [PO_4] tetrahedra, yielding a microporous open-framework structure. I identified two different hydrothermal pathways that lead to δ-$Mn_3(PO_4)_2$. In the first pathway, $Mn_3(PO_4)_2 \cdot 3H_2O$ nanosheets were reacted under hydrothermal conditions at 250 °C for 6 h. The resulting δ-$Mn_3(PO_4)_2$ product exhibited a nanoplate morphology approximately 5-40 µm in lateral dimensions with thicknesses <150 nm. The second pathway involved $Mn_5(PO_4)_2(PO_3OH)_2 \cdot 4H_2O$ as the precursor. Reacting this compound under the same hydrothermal conditions lead to microcrystals of δ-$Mn_3(PO_4)_2$. The microcrystals were approximately 100-200 µm in lateral dimensions—significantly larger than the nanoplates. The larger overall size of these microcrystals allowed analysis with single crystal X-ray diffraction, and lead to the atomic coordinates and lattice parameters of the δ-$Mn_3(PO_4)_2$ crystal structure.[1]

Furthermore, I was able to adapt a solid-state route to generate δ-$Mn_3(PO_4)_2$. Reacting $LiMnPO_4$ precursors with β-$Mn_3(PO_4)_2$ in a 1:2 ratio at 1,000 °C for 9 h also resulted in δ-$Mn_3(PO_4)_2$, along with a small amount of β-$Mn_3(PO_4)_2$.

δ-$Mn_3(PO_4)_2$ exhibits a unique open framework structure with pore sizes that range from 0.214-0.384 nm measured from Oxygen to Oxygen atom. This microporous structure shows promise in the area of small molecule separation. We attempted to carry out BET (Brunauer-Emmett-Teller) surface area and microporous analysis on δ-$Mn_3(PO_4)_2$ nanoplates, however, according to our data, the Ar gas molecules were not able to penetrate the micropores of the structure. This could be due to two reasons: 1) The pores are below the lower limit of Ar gas molecules for BET, or 2) only a small fraction of pores are accessible. The effective molecular radius for Ar is 3.54 Å, and the lower confidence limit for DFT calculations on the pore size distribution was 4.62 Å, so indeed, the pore size of δ-$Mn_3(PO_4)_2$ is near the lower limit of what can be determined by the BET method. The second reason is also a valid possibility. Because the δ-$Mn_3(PO_4)_2$ nanoplates exhibit the (002) plane, the pores are only accessible through the thinnest part of the plate. The nanoplates are 10-20 µm in lateral dimensions, but only 150 nm in thickness, making it difficult for the Ar molecules to intercalate into the pores. However, it may be possible to access the micropores of the larger δ-$Mn_3(PO_4)_2$ microcrystals.

Furthermore, δ-$Mn_3(PO_4)_2$ shows promise in the area of energy storage. The pore sizes of δ-$Mn_3(PO_4)_2$ are well in the range for Li^+ and Na^+ intercalation. Intercalation of Li^+ would result in the reduction of Mn^{2+} to Mn^0 and the formation of Li phosphates or oxides. Conversion reactions such as these are well known for transition metal oxides, and are represented by the following equation:

$$\mathrm{TMO} + 2\mathrm{Li}^+ \rightarrow \mathrm{TM} + \mathrm{Li_2O} \qquad (1)$$

Where TM is a transition metal and TMO is the transition metal oxide. In these reactions, Li reduces the metal oxide to its elemental state, forming Li_2O in the process.[2],[3] The Gibb’s free energy change (Δ_rG) in this process ranges from -230 kj.mol to -500 kj/mol depending on the transition metal oxide. Using the Nernst Equation and the value of Δ_rG, the voltage plateau can be calculated, and ranges from 0.605 V-2.200 V vs Li.[4] To date, transition metal phosphates have not been tested as conversion anodes. The reaction of $Mn_3(PO_4)_2$ with Li would likely form Li_3PO_4 and reduce Mn^{2+} to Mn^0. The electrochemical performance and activity of this compound as a conversion anode would also depend on the reversibility of this reaction. Furthermore, δ-$Mn_3(PO_4)_2$ would need a conductive coating of carbon on the surface to improve its conductivity. However, the chemical and thermal stability of the $[PO_4]$ tetrahedra in the structure makes δ-$Mn_3(PO_4)_2$ an intriguing candidate to test as a conversion anode.

Another fascinating aspect is that δ-$Mn_3(PO_4)_2$ may be stabilized by Li when synthesized by a solid-state method. Evidence for this proposal comes from the work done by myself and Oliver Clemens on δ-$Mn_3(PO_4)_2$. Clemens found that reacting β'-$Mn_3(PO_4)_2$ and $LiMnPO_4$ in stoichiometric amounts to yield a theoretical phase of $Li_{0.2}Mn_{1.40}PO_4$ lead to a new, unknown phase.[1, 5] This phase turned out to be δ-$Mn_3(PO_4)_2$, confirmed upon reproducing Clemen's synthesis and matching the XRD pattern of this compound to the simulated diffraction profile for δ-$Mn_3(PO_4)_2$. The solid-state reaction that forms δ-$Mn_3(PO_4)_2$ is carried out at 1000 °C in Ar. However, performing an *in situ* variable temperature XRD study shows that δ-$Mn_3(PO_4)_2$ is stable at temperatures <735.3 °C, above which the β' phase is formed. Therefore, the solid-state reaction would have to produce δ-$Mn_3(PO_4)_2$ on the cool down step, below 735.3 °C, otherwise any δ-$Mn_3(PO_4)_2$ formed above that temperature would be converted to the β'-phase.

The alternate possibility is that $LiMnPO_4$ stabilizes the structure of δ-$Mn_3(PO_4)_2$, allowing it to form at temperatures above the δ-β' transition. Lithium stabilization of δ-$Mn_3(PO_4)_2$ would be interesting to study both from a fundamental crystallographic point of view and a solid-state chemistry perspective and may provide insight into designing synthetic methods that lead to unique structures. First, two key questions need to be answered: 1) does $LiMnPO_4$ or Li stabilize the structure of δ-$Mn_3(PO_4)_2$ 2) what is the mechanism by which this stabilization occurs? Noteworthy is the fact that β'-$Mn_3(PO_4)_2$ was the only impurity observed in the XRD pattern of δ-$Mn_3(PO_4)_2$ synthesized by solid-state; unreacted $LiMnPO_4$ was not observed, even though it was also used as precursor. One definitive way to determine whether $LiMnPO_4$ or other Li compounds resides near the compound is by ^{7}Li solid-state NMR. The chemical shifts observed at values of 57-70.2 ppm can indexed to the Li environment in $LiMnPO_4$[6] while values for structural Li will be closer to 0 ppm.[7],[8] Answering the next question is perhaps tougher: how does $LiMnPO_4$ or Lithium incorporation stabilize the structure? One possible method is through defect sites in the lattice of δ-$Mn_3(PO_4)_2$. Defects have been observed before in several metal phosphate compounds, and are well studied in the ($LiMPO_4$ M = Mn, Fe, Co, Ni) system.[9],[10] Nevertheless, studying and exploring the Li stabilization of δ-$Mn_3(PO_4)_2$ may provide insight into synthesizing novel metal phosphate structures.

Another interesting question is whether or not it is possible to form other compounds with transition (II) metals that are isostructural with δ-$Mn_3(PO_4)_2$. Isostructural metal (II) phosphates are found in several cases, such as with the olivine $LiMPO_4$ (M = Mn, Fe, Co, Ni)[11] and $NH_4MPO_4{\cdot}H_2O$ (M = Mn, Fe, Co, Ni, and Cu).[12],[13] Various hydrated phosphates are isostructural with each other, such as $Co_3(PO_4)_2{\cdot}8H_2O$[14] and $Ni_3(PO_4)_2{\cdot}8H_2O$.[15] And, as a final thought, are there any other polymorphs of $Mn_3(PO_4)_2$ other than the four identified? This remains to be seen. Indeed, the stable [PO_4] building blocks of metal phosphates and the propensity for Mn^{2+} to form stable [MnO_5] and [MnO_6] polyhedra puts this in the realm of possibility. What is certain is that metal phosphates represent a large and diverse class of structures and there are undoubtedly more unique structures and compounds waiting to be discovered.

Chapter III details the successful synthesis of <10 nm thick $LiMnPO_4$. The synthesis route utilized $Mn_3(PO_4)_2{\cdot}3H_2O$ nanosheets as a precursor, reacting with LiH_2PO_4 under solvothermal conditions at 250 °C for 6 h. The resulting $LiMnPO_4$ nanosheets exhibit the (200) plane, and were approximately 2-10 µm in lateral dimensions, and <6 nm in thickness. Different reaction conditions lead to different products, for example, lowering the ratio of DEG:H_2O in this reaction formed Mn Phosphate compounds as products, and reacting with Li_3PO_4 lead to the formation of three-dimensional morphologies of $LiMnPO_4$.

A natural question is whether or not this chemistry can be expanded to other olivine phosphates. Recent work in our lab focused on synthesizing nanostructures of $LiCoPO_4$ from $NH_4CoPO_4 \cdot H_2O$ nanosheet precursors. This research was met with some success—$LiCoPO_4$ was synthesized in the form of nanoprisms. However, these nanoprisms formed under very stringent conditions, and were not able to be reproduced confidently.

$Mn_3(PO_4)_2 \cdot 3H_2O$ nanosheets are known to form *in-situ* during the synthesis of $LiMnPO_4$.[16],[17]. However, it is not clear whether analogous compounds, such as $M_3(PO_4)_2 \cdot 8H_2O$ (M = Co, Ni) are formed *in-situ* as intermediates in pathways that lead to $LiCoPO_4$ and $LiNiPO_4$. All the lithium metal phosphates form under slightly different hydrothermal and solvothermal conditions, and these all need to be fine-tuned in order to find a synthesis that produces nanosheets.

In chapter IV, I presented synthetic methods that lead to well-characterized $Mn_3(PO_4)_2 \cdot 3H_2O$ nanosheets and nanoscrolls. Scrolled $Mn_3(PO_4)_2 \cdot 3H_2O$ nanosheets were formed by reacting a solution of a Mn(II) salt and $(NH_4)_2HPO_4$ in a 25:5 ethanol:H_2O ratio. Other polar solvents lead to scrolling as well, including alcohols, ethylene glycol, and DMSO. Non polar solvents, such as hexane and pentane, did not result in scrolling.

Furthermore, scrolling was also observed when the pH of the $(NH_4)_2HPO_4$ precursor solution was raised above 10.00. The presence of a greater amount of HPO_4^{2-} anion at this pH may be responsible for the scrolling. Finally, we were able to directly scroll $Mn_3(PO_4)_2 \cdot 3H_2O$ by reacting these nanosheets under solvothermal conditions of 250 °C for 6 h in a 25:5 DEG:H_2O ratio. The resulting $Mn_3(PO_4)_2 \cdot 3H_2O$ product was composed of elongated belts and scrolls. This finding suggests that the original $Mn_3(PO_4)_2 \cdot 3H_2O$ nanosheets undergo dissolution and renucleate as $Mn_3(PO_4)_2 \cdot 3H_2O$ in different morphologies.

We attempted HRTEM on the $Mn_3(PO_4)_2 \cdot 3H_2O$ nanoscrolls to both confirm the scrolled morphology of $Mn_3(PO_4)_2 \cdot 3H_2O$ and to compare and contrast the lattice structure of the nanoscrolls versus nanosheets, to gain more insight into the scrolling mechanism. However, the nanoscroll morphology quickly degraded under the high beam current. This result was due to the instability of the hydrated water molecules in the crystal structure of $Mn_3(PO_4)_2 \cdot 3H_2O$ under these conditions, although the thin nature of the scroll may also play a role. Conventional microscopy techniques may not be suitable for accessing the lattice spacings of the $Mn_3(PO_4)_2 \cdot 3H_2O$ crystal structure. However, the relatively new cryo-em technique may be an alternate solution. In this technique, high resolution images (<5 Å) are obtained by taking 2D images of a sample that has previously been preserved with liquid nitrogen and then reconstructing these images into a 3D image. This technique has revolutionized structural biology by providing a method in which small and large protein complexes can be studied without damaging the sample, as in the case with conventional TEM. Furthermore, cryo-em offers researchers a way to study the structure of their compound without having to grow single crystals or obtain a significant amount of sample.[18]

This technique is not limited to just biology—a recent report in *Science* demonstrated the advantages of cryo-em for analyzing dendrites of Li metal in the SEI layer of a battery. High resolution images are difficult to obtain for Li, as it is very unstable under the electron beam. However, the researchers succeeded in obtaining atomic resolution of the lithium dendrites—a feat that was thus far impossible. The methodology was remarkably simple—lithium dendrites were electrochemically-deposited onto a copper grid, immersed in liquid nitrogen, and added to a modified TEM holder with an air-tight shutter.[19] In another report, lattice spacings of $WO_3 \cdot 2H_2O$

were successfully obtained at 200 kV using a Gatan model 914 cryo-transfer holder.[20] In general, cryo-em provides a viable option to gain high resolution images of not only $Mn_3(PO_4)_2·3H_2O$ nanosheets and nanoscrolls but of other hydrated materials.

Both $Mn_3(PO_4)_2·3H_2O$ nanosheets and nanoscrolls show promise as water oxidation catalysts. Previous work by Nam and coworkers found that $Mn_3(PO_4)_2·3H_2O$ exhibited superior water oxidation activity compared to manganese oxides. This unique property was owed to the relative ease of oxidation, arising from the Jahn-Teller effect that occurs with the oxidation of Mn^{2+} to Mn^{3+}, stabilized by the five and six-coordinated polyhedra and phosphate tetrahedral in the structure.[21] While this study was carried out with nanosheets of $Mn_3(PO_4)_2·3H_2O$, it would be interesting to perform a similar experiment with $Mn_3(PO_4)_2·3H_2O$ nanoscrolls. In fact, Osterloh and coworkers found improved photocatalytic activity of nanoscrolls versus nanosheets of hexaniobate.[22]

Another intriguing application for $Mn_3(PO_4)_2·3H_2O$ nanosheets and nanoscrolls is as supercapacitors. One report showed an activity of 2,086 F/g with a graphene and $Mn_3(PO_4)_2·3H_2O$ nanosheet hybrid catalyst.[23] This activity arose from the synergistic effect role graphene had in increasing the electrochemical surface area of the $Mn_3(PO_4)_2·3H_2O$ nanosheets. Because of the two-dimensional nature of $Mn_3(PO_4)_2·3H_2O$, there are many ways it can be incorporated with graphene. Once again, it would be interesting to compare the nanoscroll morphology to the nanosheet morphology.

Finally, comparing the electrochemical activity of $Mn_3(PO_4)_2·3H_2O$ to the anhydrous forms (α, β’, γ, and δ polymorphs of $Mn_3(PO_4)_2$) would be an interesting endeavor. Veronica Augustyn’s group at North Carolina State University found that $WO_3·2H_2O$ showed significantly higher capacity retention and reversibility for proton storage than the anhydrous WO_3 compound.

They proposed that the interlayer hydrates allowed for faster H$^+$ and more efficient intercalation into the hydrated lattice.[20]

In conclusion, manganese (II) phosphate compounds exhibits a wealth of chemistry. As shown in figure 5.1, the synthesis of each compound is impacted by different reaction conditions, including temperature, amount of H_2O, pH, and precursor used. Furthermore, morphology can also be fine-tuned by changing these parameters. Despite the differences in preparation, manganese (II) products and precursors are highlighted by a set of interconnected reactions. Finally, the manganese (II) phosphate system is just one of many different metal phosphate systems and provides a roadmap to form other novel metal phosphate materials.

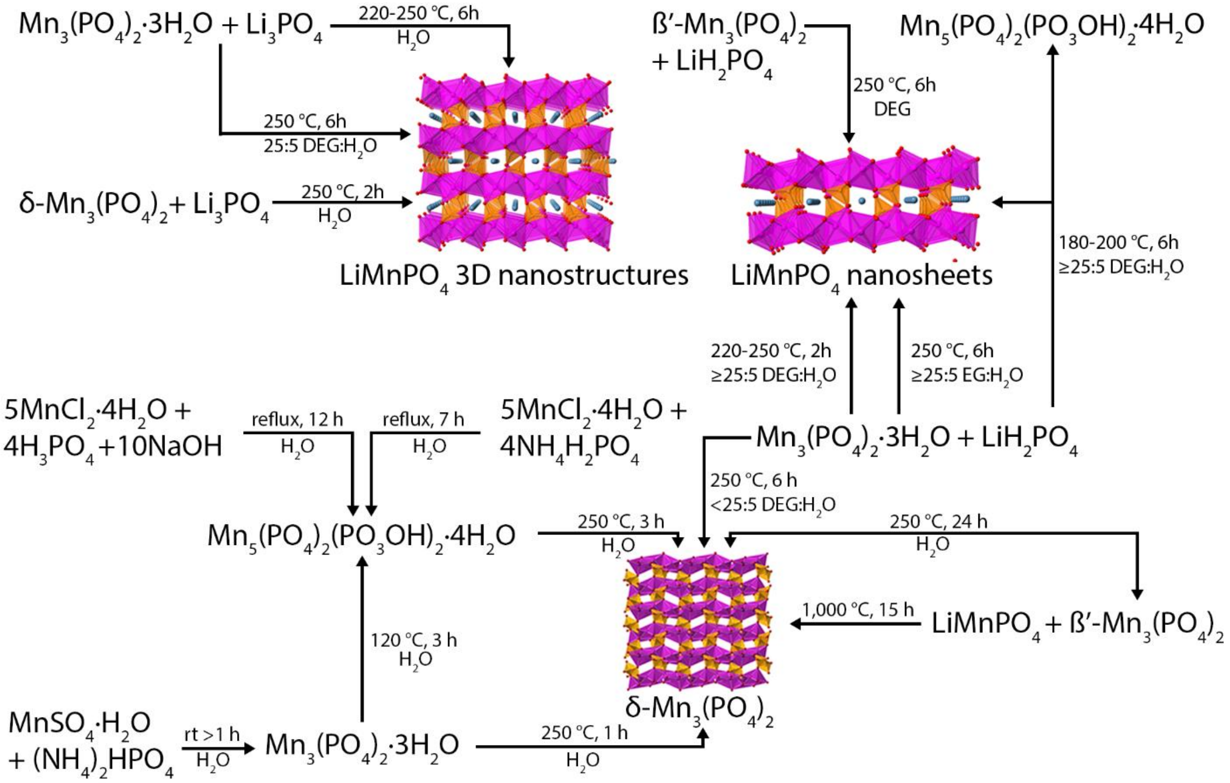

Figure 5.1: Schematic of the reaction pathways that lead to Manganese (II) phosphates

References

[1] G. Neher and T. T. Salguero, *Crystal Growth & Design* **2017**.

[2] J. Cabana, L. Monconduit, D. Larcher and M. R. Palacin, *Adv Mater* **2010**, *22*, E170-192.

[3] K. M. Abraham, D. M. Pasquariello and E. B. Willstaedt, *Journal of The Electrochemical Society* **1990**, *137*, 743-749.

[4] P. Poizot, S. Laruelle, S. Grugeon and J.-M. Tarascon, *Journal of The Electrochemical Society* **2002**, *149*, A1212-A1217.

[5] O. Clemens, *(Saarbrücken, http://scidok.sulb.uni-saarland.de/volltexte/2012/4718/)* **2011**.

[6] S. L. Wilcke, Y.-J. Lee, E. J. Cairns and J. A. Reimer, *Applied Magnetic Resonance* **2007**, *32*, 547-563.

[7] G. P. Holland, D. A. Buttry and J. L. Yarger, *Chemistry of Materials* **2002**, *14*, 3875-3881.

[8] M. Wagemaker, R. van de Krol, A. P. M. Kentgens, A. A. van Well and F. M. Mulder, *Journal of the American Chemical Society* **2001**, *123*, 11454-11461.

[9] S. Y. Chung, S. Y. Choi, S. Lee and Y. Ikuhara, *Phys Rev Lett* **2012**, *108*, 195501.

[10] M. S. Islam, D. J. Driscoll, C. A. J. Fisher and P. R. Slater, *Chemistry of Materials* **2005**, *17*, 5085-5092.

[11] A. K. Padhi, K. S. Nanjundaswamy and J. B. Goodenough, *Journal of The Electrochemical Society* **1997**, *144*, 1188-1194.

[12] A. Yuan, J. Wu, L. Bai, S. Ma, Z. Huang and Z. Tong, *Journal of Chemical & Engineering Data* **2008**, *53*, 1066-1070.

[13] S. G. Carling, P. Day and D. Vissen, *Inorganic Chemistry* **1995**, *34*, 3917-3927.

[14] H. Shao, N. Padmanathan, D. McNulty, C. O′Dwyer and K. M. Razeeb, *ACS Applied Materials & Interfaces* **2016**, *8*, 28592-28598.

[15] V. N. Viter and P. G. Nagornyi, *Russian Journal of Applied Chemistry* **2009**, *82,* 935-939.

[16] C. Delacourt, P. Poizot, M. Morcrette, J. M. Tarascon and C. Masquelier, *Chemistry of Materials* **2004**, *16*, 93-99.

[17] S.-L. Yang, R.-G. Ma, M.-J. Hu, L.-J. Xi, Z.-G. Lu and C. Y. Chung, *Journal of Materials Chemistry* **2012**, *22*, 25402.

[18] X. C. Bai, G. McMullan and S. H. Scheres, *Trends Biochem Sci* **2015**, *40*, 49-57.

[19] Y. Li, Y. Li, A. Pei, K. Yan, Y. Sun, C.-L. Wu, L.-M. Joubert, R. Chin, A. L. Koh, Y. Yu, J. Perrino, B. Butz, S. Chu and Y. Cui, *Science* **2017**, *358,* 506-510.

[20] J. B. Mitchell, W. C. Lo, A. Genc, J. LeBeau and V. Augustyn, *Chemistry of Materials* **2017**, *29,* 3928-3937.

[21] K. Jin, J. Park, J. Lee, K. D. Yang, G. K. Pradhan, U. Sim, D. J. Jeong, H. L., S. Park, D. Kim, N. E. Sung, S. H. Kim, S. Han and K. T. Nam, *J Am Chem Soc* **2014**, *136*, 7435-7443.

[22] M. C. Sarahan, E. C. Carroll, M. Allen, D. S. Larsen, N. D. Browning and F. E. Osterloh, *Journal of Solid State Chemistry* **2008**, *181,* 1678-1683.

[23] C. Yang, L. Dong, Z. Chen and H. Lu, *The Journal of Physical Chemistry C* **2014**, *118,* 18884-18891.